LBL-5784
c.1

ANALYSES OF GRAIN BOUNDARY REACTIONS IN ALUMINUM-ZINC ALLOYS UTILIZING LATTICE IMAGING ELECTRON MICROSCOPY

Ronald Gronsky
(Ph. D. thesis)

December 1976

Prepared for the U. S. Energy Research and Development Administration under Contract W-7405-ENG-48

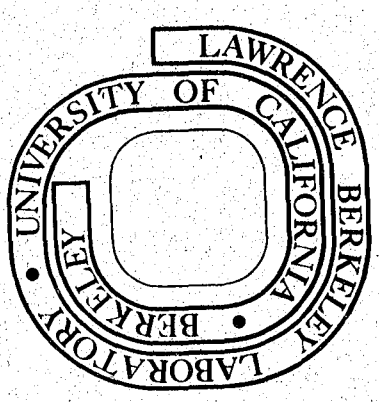

LBL-5784
c.1

LBL-5784

Analyses of Grain Boundary Reactions in Aluminum-Zinc Alloys Utilizing Lattice Imaging Electron Microscopy

Ronald Gronsky

Lawrence Berkeley Laboratory
University of California
Berkeley, California 94720

December 1976

Work performed under the auspices of the U. S. Energy Research and Development Administration

in memory of my mother

CONTENTS

ABSTRACT

Lattice imaging and conventional transmission electron microscopy have been applied in an investigation of the relationship between grain boundary structure and boundary-nucleated phase transformations. The study encompassed three reactions associated with grain boundaries in the Al-Zn system: heterogeneous nucleation at grain boundaries, discontinuous precipitation involving the R-phase and the low temperature discontinuous reaction. In conjunction with image computations, lattice images were interpreted using direct fringe spacing measurements, microdensitometer traces and optical diffraction, providing superior capabilities in structural and chemical analysis. Errors of $\leq 1\%$ were achieved by only 10-fringe samplings using an internal magnification standard.

Results indicate that solute enrichment and composition profiles within both matrix and precipitate phases can be detected in regions ≤ 10 Å from the boundary plane. Direct verification of the plane matching model is presented in lattice images at interphase interfaces of heterogeneously nucleated grain boundary precipitates. These images reveal the occurrence of structural relaxation at boundary positions of high atomic density and the presence of one to two atom layer microledges in facted growth fronts. The discontinuous R-phase reaction is shown to display misorientations of $\leq 3°$ between neighboring lamellae, detectable only in the lattice image mode, which also reveals absolute continuity in orientation and composition of the Al-rich phase across low temperature discontinuous reaction fronts.

It is concluded that structural effects at grain boundaries are secondary to the orientation of the boundary plane in promoting effective catalysis of grain boundary precipitation reactions. In the Al-Zn system,

boundary segments which parallel the trace of low index matrix planes are energetically favored reaction sites. Lattice imaging further reveals that those segments parallel to a {111} matrix trace impart the additional advantage of enhanced decomposition kinetics.

1. INTRODUCTION

Virtually all engineering materials are utilized in polycrystalline form and their properties are largely influenced by the presence of grain boundaries as microstructural constituents. Unfortunately except for their role in strengthening (i.e. as obstacles, or sources, for slip),[1,2] grain boundaries are detrimental defects. Intergranular failure seriously impairs materials performance in a wide variety of applications under conditions ranging from high temperature creep[3,4] to low temperature embrittlement.[5,6] The ultimate improvement in mechanical properties of these materials is therefore strongly dependent upon a detailed knowledge of the relationship between grain boundaries and microstructure.

One of the most convincing ways in which grain boundaries affect alloy properties is by catalysis of solid state phase transformations. Heterogeneous precipitation,[7] discontinuous precipitation[8-10] and discontinuous growth[11,12] are examples of reactions which can cause drastic changes in microstructure by employing grain boundaries as reaction fronts. The propagation of these reactions is controlled by the mobility[13] and/or diffusivity[14] characteristics of the involved grain boundary sites and can be easily monitored by light-[15] or electron-optical[16] techniques. Considerable difficulty arises however in detecting the initiation of grain boundary reactions, the structural characteristics of favored reaction fronts and the manner in which active grain boundaries facilitate transformation behavior. Such studies require a level of spatial resolution which has only recently[17,18] become available in current generation transmission electron microscopes.

In view of the above questions, the object of this research was to analyze, using transmission electron microscopy (TEM) at high resolution, the structural aspects of the relationship between grain boundaries and boundary-nucleated phase transformations. The Al-Zn binary system was chosen for this study primarily due to the ease with which reaction products can be obtained[19] and its excellent electron transparency. Specimen preparation procedures were tailored to represent bulk behavior as closely as possible. Because it is a pioneer application of the technique, an assessment was also made of the best conditions for lattice imaging of grain boundary reactions in alloys. A computer program was formulated for image calculation and an experimental determination of the accuracy of the lattice imaging technique for localized chemical analysis was performed, the latter appearing in the appendix. Complementary applications of conventional TEM and weak beam imaging were also made and the results are compared with current theories of grain boundary structure.

2. REVIEW OF THEORY

2.1 Grain Boundary Structure

Due primarily to some of the recent experimental findings on grain boundary properties,[20] theoretical models of grain boundary structure based upon disorder or amorphous layers have given way to those emphasizing order or periodicity within the boundary region. (For a review of earlier models see refs. 21-23; more recent models are reviewed in refs. 24-27.) In the most popular formulation of this concept, a transition lattice is described which is a superlattice of two misoriented crystal lattices and which is continuous in spite of the presence of the boundary. Based upon this model, it has been suggested[28,29] that when the boundary plane is also a plane of the transition lattice there will be good atomic fit and hence a low energy configuration at the grain boundary.

It has been shown[30] that two cubic space lattices will share a superlattice of coincidence sites when rotated by an angle θ about the direction [hkl] if

$$\theta = 2 \tan^{-1} \left(\frac{y}{x}\right)\sqrt{N}$$

where x and y are integer coordinates and N is given by

$$N = h^2 + k^2 + l^2 \quad .$$

After this operation, the fraction of total lattice sites which coincide will be $1/\Sigma$, where

$$\Sigma = x^2 + Ny^2 \quad .$$

The multiplicity, Σ, must have only odd values in the cubic system. Therefore, even Σ solutions are divided by the correct multiple of 2 to yield an odd value. Tables have been published[25,27,31] which contain axis/angle pairs (i.e. values of [hkl] and υ) that produce a

coincidence site lattice (CSL) for multiplicities ranging up to $\Sigma = 19$. It should be obvious that all rotational symmetry elements yield $\Sigma = 1$ (ref. 30). The next highest degree of coincidence in the cubic system, $\Sigma = 3$, occurs for the familiar twinning operation.[32]

When the CSL concept is used in the description of grain boundaries, it is necessary to also consider the orientation of the boundary plane. For grain boundaries inclined to CSL planes a ledge structure is anticipated[28,33] in order to provide a maximum areal fraction of good matching. Recent refinements of this structural unit model have accounted for localized atomic relaxation in the boundary region[34,35] and experimental evidence has been obtained for rigid body translations at coincidence boundaries.[36]

The above formulation reveals that lattice spacings in a CSL are a discontinuous function of rotation angle θ. Recognizing this as a shortcoming of the model, Bollman[26] generalized the concept of coincidence to include not only lattice points, but their interstices as well. Subdividing general lattice coordinates into external coordinates which locate a unit cell and internal coordinates, which position a point within the unit cell, he defined "0-points" as those having internal coordinates (000). Hence 0-points are coincidences of points which have equivalent positions within the two lattices.

The construction of an 0-lattice then follows mathematically. Defining $\underset{\sim}{x}_0$, the base vectors of the 0-lattice; $\underset{\sim}{x}_1$, the base vectors of lattice 1; $\underset{\sim}{A}$, the transformation matrix and $\underset{\sim}{I}$, the identity matrix, a lattice of 0-points is described by:[26]

$$\underset{\sim}{x}_0 = (\underset{\sim}{I} - \underset{\sim}{A})^{-1} \underset{\sim}{x}_1 \quad .$$

On this model, 0-lattice spacings are a continuous function of rotation

angle θ, and whether or not they are CSL points, O-points represent positions of good fit for the two interpenetrating lattices. For the special case of an exact CSL orientation, every other O-point is a CSL point, making the coincident site lattice a superlattice of the O-lattice.

In a less rigorous description of grain boundary structure, Pumphrey[37,38] suggests that the matching of a set of low index lattice planes across a grain boundary provides for a low energy configuration. Hence, on the plane matching (PM) model, a grain boundary will assume the structure necessary to preserve continuity of low index atom planes across its interface. The difference between the PM and CSL models is best emphasized by considering a boundary between crystals misoriented about a low index axis. On the PM model, all rotation angles for this boundary would be of relatively low energy; however on the CSL model, only specific misorientation angles yield a low energy boundary. In one description[39] a PM boundary is a limiting case of a CSL boundary with $\Sigma \to \infty$. The primary advantage of the PM model is its close association with TEM imaging[40,41] of grain boundaries.

Based upon these various models, there have been numerous descriptions of the defect structures expected at grain boundaries. Employing the CSL approach, Schober and Balluffi[42,43] rationalized that deviations in the boundary plane from a CSL plane would be accommodated by a network of dislocations having Burgers vectors equal to CSL translation vectors. These were designated "intrinsic" grain boundary dislocations to distinguish them from "extrinsic" grain boundary dislocations that may have originated from adsorbed lattice defects.[44]

On the O-lattice model, Bollman[26] classifies "primary" grain boundary dislocation networks (intersections of the boundary with O-lattice misfit cell walls) and "secondary" grain boundary networks (partial dislocations of the nearest CSL), noting that in the general case primary displacements are a subset of secondary displacements. In specifying the nature of defects in the O-lattice, an additional construction, the "complete pattern shift" lattice, termed the DSC lattice, is utilized.

Mismatch accommodation on the plane matching model has been given an optical analogue by Pumphrey,[37] in keeping with TEM observations. Representing the misoriented low index planes as overlapping optical gratings (see Fig. 1), Pumphrey compares the resulting Moiré pattern to the structural lines actually observed in the microscope.[40,41] Assuming that the dark lines of the grating represent atom planes, then the high opacity Moiré bands indicate regions of high atomic density. Pumphrey suggests that atomic relaxation in these high density regions gives rise to strain fields which are then imaged by TEM in either or both grains. The spacing (d) of these lines can be computed by the well-known Moiré formula:[45]

$$d = \frac{d_1 d_2}{(d_1^2 + d_2^2 - 2d_1 d_2 \cos\theta)^{\frac{1}{2}}}$$

where d_1 and d_2 are the spacings of the lattice planes misoriented by θ at the boundary. The angle (ρ) between the structural Moiré lines and the trace of lattice 1 is given by (see Fig. 1):

$$\sin\rho = \frac{d_1 \sin\theta}{(d_1^2 + d_2^2 - 2d_1 d_2 \cos\theta)^{\frac{1}{2}}} \quad .$$

Pumphrey further adds[27] that in terms of a CSL with $\Sigma \to \infty$, the periodic misfit lines are dislocations with Burgers vectors equal to the interplanar spacing.

2.2 High Resolution Electron-Optical Imaging

The theory of electron-optical imaging has reached an advanced state of development as evidenced by the extensive reviews[46-49] on the subject which are elaborate in detail. The purpose of this section is to briefly summarize the mechanisms involved in high resolution imaging with respect to the formation and interpretation of lattice fringe images.

Following a suggestion by Cowley,[50] the formation of an image in an electron microscope can basically be divided into two components:

(1) the modification of the incident electron wave by transmission through the specimen; and

(2) the modification of the resulting wave amplitude distribution by the image formation system.

Because the specimen in this case is a periodic object (with the periodicity of the lattice planes being imaged) then component (1) above can be described on the basis of Abbé's theory (see refs. 51 and 52 for review). Assuming plane parallel illumination, Abbé's principle states that during imaging by a lens, all incident radiation which is scattered by the object at a given angle will be brought to focus at a singular point. Hence the amplitude distribution at the back focal plane due to the presence of the specimen is that of a Fraunhofer diffraction pattern.

The formation of such a pattern is described mathematically[53,54] by the Fourier transform function, indicated here by F. Letting

$\psi'(\underset{\sim}{r}')$ represent the wavefunction transmitted by the specimen (i.e. at its exit surface), then in the idealized case, the wavefunction ($\eta'(\underset{\sim}{g})$) at the back focal plane of the objective lens is given by:

$$\eta'(\underset{\sim}{g}) = F[\psi'(\underset{\sim}{r}')] \quad .$$

This situation is never realized however, due to component (2) above of the image formation process. Upon transmission through a less than perfect lens, off-axis illumination is retarded in phase with respect to that component of the wavefront which travels down the optic axis ($\underset{\sim}{g} = 0$). The resultant phase shift can be described[47] by introducing a phase distortion function which depends on electron wavelenth (λ),

$$\chi(\underset{\sim}{g}) = \frac{2\pi}{\lambda}\{C_s \frac{\lambda^4 g^4}{4} - \Delta z \frac{\lambda^2 g^2}{2}\}$$

and which accounts for the effect of spherical aberration (C_s = spherical aberration coefficient) and focus condition (Δz = extent of defocus). Other aberrations which have been neglected are either less severe[17] (e.g. chromatic aberration) or can be corrected at the microscope (viz. astigmatism). The actual wavefunction is then given by:

$$\eta(\underset{\sim}{g}) = \eta'(\underset{\sim}{g})\ e^{i\chi(\underset{\sim}{g})} \quad .$$

To complete the image formation process on Abbé's theory each point of the diffracted amplitude distribution can by considered as a source for a Huygens wave propagating to the conjugate image plane. The amplitude distribution at the image is then determined by summing all the Huygens waves from the back focal plane with attention to phase. Since the image plane is effectivcly at infinity from the back focal plane, this interference effect can again be described[51] by a Fourier transform to yield the image wavefunction

$$\psi(\underset{\sim}{r}) = F^{-1}[n(\underset{\sim}{g})]$$

and the actual image intensity

$$I(\underset{\sim}{r}) = \psi^{*}(\underset{\sim}{r})\psi(\underset{\sim}{r}) \quad .$$

It should be noted that in the idealized case the image is identical, apart from a magnification factor, to the intensity distribution at the exit face of the crystal. "High resolution" therefore refers to an image of the diffracting species. Complications may arise from deviations in periodicity within the object[45] e.g. crystal imperfections, size limitations, strain and thermal diffuse scattering, which: (1) introduce an unwanted range of periodicities in the back focal plane, reducing contrast, and (2) contribute to increased amplitude of diffraction by the objective aperture, impairing resolution.[52] Hence, particularly when imaging crystal imperfections or small crystallites (e.g. precipitates), thick specimens should be avoided.

Overcoming the effects of the phase distortion function generally requires either improved (achromatic) lens design or the elimination of higher order diffracted amplitudes at the back focal plane by an objective aperture.[55] At the minimum condition, the transmitted beam on the optic axis is made to interfere with only one strongly diffracted off-axis beam. However these circumstances still cause the location of fringes within the image and their visibility to be subject to a strong phase error through defocus.[52]

An alternative method, developed by Dowell[56-58] incorporates two beams which, by changing the angle of illumination, are made to travel symmetrically with respect to the optic axis (see Fig. 2). By this procedure, the magnitude of the phase distortion function for

the transmitted (0) beam (located at -g/2 from the optic axis) is made equal to that for the diffracted (g) beam (located at +g/2 from the optic axis), with the result indicated below.

With reference to Fig. 2, the wavefunction at any arbitrary point $\underset{\sim}{x}$ in the image plane is computed using the familiar[45,52] form of the wave equation:

$$\psi(\underset{\sim}{x}) = \phi_o e^{i(\underset{\sim}{K}\cdot\underset{\sim}{r}_o)} e^{i\chi_o} + \phi_g e^{i(\underset{\sim}{K}\cdot\underset{\sim}{r}_g)} e^{i\chi_g} \quad .$$

Here ϕ_o and ϕ_g are the transmitted and diffracted wave amplitudes determined from the dynamical theory (see Sec. 4). They are a function of depth in the foil and hence contain the thickness dependence. In the phase factors, $\underset{\sim}{K}$ is the propagation wave vector ($= \frac{2\pi}{\lambda}$), and $\underset{\sim}{r}_o$ and $\underset{\sim}{r}_g$ are the ray paths followed by the transmitted and diffracted beams, respectively. In general a spectral path distance $|\underset{\sim}{r}|$ differs from the distance $|\underset{\sim}{r}_o'|$ along the optic axis by an amount δr given by:

$$\delta r = \frac{\lambda x}{2dM}$$

where d is the lattice spacing and M the magnification. Hence,

$$K\cdot r = K\cdot r_o' + \frac{\pi x}{dM} \quad .$$

Recognizing that x changes sign between beams 0 and g across the optic axis, the wavefunction can be rewritten in the form

$$\psi(\underset{\sim}{x}) = e^{i\underset{\sim}{K}\cdot\underset{\sim}{r}_o'} \left[\phi_o e^{-i\frac{\pi x}{dM}} e^{i\underset{\sim}{\chi}_o} + \phi_g e^{i\frac{\pi x}{dM}} e^{i\underset{\sim}{\chi}_g}\right]$$

from which the intensity distribution at the image plane is obtained:

$$I(\underset{\sim}{x}) = \psi^*(\underset{\sim}{x})\psi(\underset{\sim}{x})$$

$$= |\phi_o|^2 + |\phi_g|^2 + 2|\phi_o||\phi_g| \cos\left(\frac{2\pi x}{dM} + \chi_g - \chi_o\right) \quad .$$

Inspection of the cosine argument reveals immediately that under tilted illumination conditions (i.e. $\chi_o = \chi_g$) the image faithfully displays the period of the lattice planes, and will not exhibit variations in phase contrast with defocus. In fact the position of the fringes is true at exact focus. It should also be noted that any chromatic errors (e.g. lens current or high voltage fluctuations) will affect both beams identically, and will therefore cancel out.

Maximum success with obtaining interpretable lattice fringe images can therefore be anticipated using the two-beam tilted illumination technique. It is capable of achieving a theoretical resolution limit[45] given by

$$d_{min} = (\pi C_s \Delta\alpha \frac{\lambda}{2})^{1/3}$$

which for actual values of the beam divergence angle ($\Delta\alpha$) and current instrument parameters is $\simeq 2\text{Å}$. Due to its strongest dependence on electron wavelenth (λ), ultimate significant improvement in resolution will require the use of higher accelerating voltages (see e.g. ref. 59).

3. HISTORICAL

3.1 Experimental Studies of Grain Boundaries

The concept of a grain boundary was originally formulated by Sorby[60] following his observations of metallic specimens using light optical microscopy. This technique produces a linear image of a grain boundary at its intersection with a polished specimen surface. It can be used to determine grain size, grain boundary curvature, and with suitable specimen sectioning,[61] the topographical features of polycrystalline aggregates. However, with the exception of etch pit decoration,[62] light optical microscopy cannot resolve details of grain boundary structure.

Of the electron optical techniques applied to the study of grain boundaries, many have shown similar limitations. Thermionic emission microscopy[63] is a well proven method for the dynamic observation of grain growth in metals and alloys.[64,65] However the emission image of a crystalline boundary is merely a projection of its surface intersection line, and as such it offers no improvement in resolution over light optical microscopy. Even scanning electron microscopy (SEM), which allows fracture surfaces to be imaged at superior resolution,[66] lacks the capacity for providing direct images of grain boundary structural detail.

Because a grain boundary separates crystalline regions which differ in orientation, structure and/or composition, it is necessary to simultaneously extract information from each of these regions, preferably at atomic resolution, if the structure of the grain boundary is to be accurately represented. Field ion microscopy (FIM) is a technique capable of resolving the atomic configuration of a pointed filament

tip and has been applied to fundamental studies of grain boundary structure.[28,67-69] However results have been limited due to the difficulties of specimen preparation and the small areas of grain boundaries actually imaged. In order to enhance the statistical study accompanying FIM applications to grain boundaries, digitization and computer graphics procedures have recently been employed.[70] Nevertheless these refinements still produced only qualitative results due to poor grain boundary contrast.[71]

An indirect analysis of grain boundary structure has also been attempted using electron[72] and x-ray[73,74] diffraction techniques. The method involves the detection of extra reflections originating from the transition lattice of crystals which are misoriented across a grain boundary. In both cases limitations were imposed by double diffraction, although this effect was judged less severe in the x-ray study. For this reason it was suggested[75] that intensity measurements of the extra x-ray reflections could provide more detailed data on grain boundary structure. However it was also pointed out[76] that there are major difficulties in such a study stemming from the preparation of suitable specimens and the detection of very weak scattered intensities.

By far the most successful method for studying grain boundaries has been conventional transmission electron microscopy (TEM) due to its ability to provide both diffraction and imaging information. Techniques have been devised to determine the misorientation across grain boundaries with high precision using selected area diffraction (SAD).[77-82] In the imaging mode, contrast effects from grain boundaries and their substructural features (viz. ledges,[33,83] dislocations[84]) are well documented both experimentally[44,85-87] and in

simulations[88-93] computed on the basis of the dynamical theory of electron diffraction. Similar studies have also been performed with greater ease using oriented bicrystals[41,94] and non-conventional techniques, viz. weak beam microscopy.[95] The latter method showed particular advantage in producing images of defect structures at grain boundaries with enhanced clarity and resolution.

As a result of these investigations there is firm evidence that grain boundary defects are important structural features. Grain boundary dislocations have been found to possess Burgers vectors which are not necessarily lattice translation vectors,[42] and may be instrumental in the migration of grain boundaries.[96] Ledges are also shown to vary in density along grain boundaries as a well behaved function of misorientation between grains.[86] Together these findings indicate that periodicity is a significant parameter in grain boundary structure, also making possible the correlation of theoretical transition lattice models (see Sec. 2.1) of particular misorientation grain boundaries with experimentally observed structural configurations in the interfacial area.[36,82,97]

3.2 Effects of Boundary Structure on Precipitation Behavior

The first attempt at a systematic study of grain boundary precipitation was performed by Toney and Aaronson[98] using oriented bicrystals of silicon-iron. They observed that precipitation of austenite from the ferritic matrix occurred preferentially at grain boundaries only when the misorientation angle (θ) exceeded ~11°. The rate of growth at the boundary region was also found to increase rapidly as θ increased, and this was attributed to increased boundary diffusivity.[99] It was further observed that boundary nucleation was

favored at small angle boundaries having a higher density of misfit dislocations in screw orientation.

A subsequent study of an Al-Ag alloy was carried out by Clark[100] and yielded similar results. At boundaries for which $\theta \lesssim 16^{\circ}$, γ precipitation occurred as plates growing along {111} planes of the Al-rich matrix. For $\theta \gtrsim 16^{\circ}$ however, the precipitates established a planar interface with the grain in which they were nucleated and grew into the neighboring grain by migration of their curved interface. The density of precipitates was also found to increase with increasing θ.

Vaughan[101] extended this type of research to the Al-Cu system and found that low angle boundaries ($\lesssim 9^{\circ}$) were more effective in nucleating the intermediate θ' phase, while the equilibrium θ phase was found at higher misorientation boundaries. He reasoned that because the intermediate phase is partially coherent with the matrix, it tends to seek a dislocated (low angle) boundary where it might nucleate with lower elastic strain energy. Conversely the equilibrium phase is incoherent with the matrix and prefers a more disordered (high angle) boundary for reduction of surface energy.[101]

Unwin and Nicholson[102] later employed the coincidence site lattice (CSL) model[29] to correlate grain boundary structure and precipitation behavior. In their analysis of Al-Mg and Al-Zn-Mg alloys, they observed that high angle boundaries within ~4° of a coincidence relationship had a very low density of precipitates, while those boundaries at further deviations from a CSL orientation showed a much greater density of precipitates. This distinction was found to disappear however at higher levels of supersaturation when precipitation on all high angle boundaries was similar. It was also observed[102] that

the position of the boundary plane did not affect precipitate density. On the CSL theory, this result indicated that there is no apparent correlation with the misfit structure of high angle boundaries.[28] In contrast to these conclusions, Le Coze et al.[103-105] found that the density of precipitates in Al-Cu bicrystals was highest at grain boundaries having low energy symmetrical CSL orientations, and that the observed variation in precipitate density with boundary misorientation was not a trivial one.

An attempt at explaining these observations was made by Aaron and Bolling[106] on the concept that free volume at a grain boundary determines grain boundary phenomena. They suggested that for semicoherent precipitates, the ability to maintain matrix coherency should decrease, and hence the rate of nucleation should decrease, as boundary free volume increases. Incoherent precipitates on this argument would therefore increase in density as boundary free volume increases. Although satisfactory in its general description, this model still does not explain the observation[103,104] of a wide variation in precipitate density at boundaries having the same effective free volume.

More recently, Pumphrey[107] has referred to published experimental evidence as indicating that boundary structure is only of secondary importance in precipitate nucleation. Instead he contends that nucleation will be favored whenever a precipitate can easily establish a low energy semicoherent interface with at least one of the grains bordering the boundary region. A similar explanation had been invoked by Vaughan[108] in his follow-up study on Al-Cu during which he reported the observation of θ' precipitation on high angle rather than the expected low angle boundaries seen earlier.[101] He concluded that the

semicoherent precipitates were able to reside at the boundaries in a low energy configuration with both bordering grains. In a related claim, Russell and Aaronson[109] give evidence that solution annealing temperature may affect grain boundary precipitation due to a temperature dependent solute adsorption rather than any grain boundary structure effects as previously suggested.[110]

In summary, although there has been considerable progress in relating grain boundary structural models to observed boundary defect configurations (Sec. 3.1), the work on grain boundary precipitation is less conclusive. A recent review of in-situ studies by Butler and Swann[111] reflects on the necessity of establishing better boundary structure to growth parameter relationships in grain boundary precipitation research. All of the above studies furthermore illustrate the need for high resolution information on the boundary/precipitate interfacial regions.

3.3 Lattice Imaging of Alloys

Lattice imaging is a high resolution technique in transmission electron microscopy whereby structural information about suitable specimens can be obtained at the atomic level (for a recent general review, see Allpress and Sanders, ref. 17). The method is extremely attractive for the study of materials because it provides a direct image of the object rather than an assemblage of scattered intensities which must then be reconstructed to provide an (indirect) image. There is danger in empirical interpretation of lattice images however, especially with regard to crystal defects,[50,112] owing to the mechanisms of image formation in the electron microscope. Recognition of this problem has prompted calculations of image contrast in n-beam

lattice images, particularly for complex materials with large unit cells where n is of the order of 100 (refs. 113-118). For these materials it is possible to obtain lattice images containing two dimensional detail. Under appropriate imaging conditions (viz. number of beams, microscope aberrations, extent of defocus, specimen thickness and orientation),[116-118] a representation of structure is obtained in the form of a projection of charge density within the material,[119] e.g. a row of metal atoms parallel to the incident beam will give a dark spot in the image.

Point-to-point resolution of this kind is currently limited in conventional transmission electron microscopes[118] to about 3.5 Å. It is clear therefore that interpretable structural resolution of metallic systems having much smaller unit cells is not routinely possible. For these materials, which include nearly all commercially important alloys, lattice imaging is presently restricted to one dimensional detail in the 2 Å range. A summary of the theory of one dimensional lattice image formation is presented in section 3.2. The following is a brief account of the applications of the technique in materials science.[120]

Many of the early studies utilizing lattice imaging for quantitative analysis involved crystal lattice dislocations.[121-123] In these investigations, measurements were made of spacing perturbations surrounding terminating fringes and were related through isotropic elasticity theory to the core width, core strain and long range matrix strains associated with dislocations. Such studies were also applied to crossed lattice images[124] to examine the effects of lattice strain on atomic positions. However it was later demonstrated[125] both experimentally and through contrast calculations that an inclined

lattice dislocation may produce either one or three terminating fringes in a two beam image, depending upon the direction ($+\underset{\sim}{g}$ or $-\underset{\sim}{g}$) of the operating reflection. Only when the dislocation line was oriented end-on with respect to the electron beam was a single fringe termination produced.[125] These results not only invalidated all earlier findings[121-124] but also demonstrated that extreme care must be taken to assure a one-to-one correspondence between terminating fringe profiles and matrix dislocations.

Subsequent research on dislocation strain fields was carried out using specimens prepared under rigid geometrical constraints[126] in order to assure the required end-on dislocation configuration. In other defect studies, lattice imaging was successful in revealing microtwins of 3 atom plane thicknesses in silicon, as well as the occurrence of highly regular periodic structures in incoherent twin boundaries.[127] It was also observed that in ion-bombarded Ge, damaged regions exhibited no fringe contrast suggesting a lack of crystallinity,[128] while similar defects in Cu were found to have a complex strain field detected only in the lattice image mode.[129]

By providing detail which supersedes the resolution capabilities of other experimental techniques, lattice imaging has considerably enhanced our understanding of phase transformation behavior. Following the direct observation[128] of G.P. zones in Al-Cu by this method, a quantitative assessment of zone size, density and displacement field was subsequently performed at the atomic level[130] and more recently extended through the precipitation sequence.[131] This latter study revealed a continuous structure progression from G.P. zones through θ' precipitation, allowing identification of each phase by its

characteristic fringe spacing even when such evidence in the electron diffraction patterns was questionable. Similar applications to a Cu-Be alloy permitted analysis of monolayer G.P. zones by {200} lattice images in spite of a very strong {110} tweed constrast.[132] When utilized in an examination of the omega transformation in Zr-Nb, lattice imaging furthermore confirmed the existence of three subvariants within a previously identified single omega variant.[133]

In research on ordering in Cu_3Au (refs. 134-136), Au_4Cr and Au_3Cr (ref. 137) and Mg_3Cd (ref. 138), lattice imaging has confirmed the microdomain model of short range order, permitted measurements of domain wall thicknesses at APB's, provided direct evidence for the origin of superlattice spot splitting, revealed atomic arrangements in the area of translational and rotational APB's, identified phases and indicated a ledge mechanism for ordering and domain growth. Because each of these studies involved multi-beam imaging, corresponding image computations were also performed.

The only published report of lattice imaging at grain boundaries[139] actually involves the superlattice image produced by combining 0-lattice reflections[72] within the objective aperture. By this method a representation of the 0-lattice was obtained at misorientation angles up to ~25°. Secondary grain boundary dislocations were also imaged even though no diffraction evidence for their existence was found.[72]

Applications of lattice imaging in alloy systems has therefore demonstrated success in two primary analytical fields. The first of these is structural research, which relies on the detection of geometrical arrangements in fringe images to reveal information about the atomic

arrangements within crystalline specimens. The second is chemical analysis, made possible by comparing relative fringe spacings to known variations (as determined for instance by x-ray analysis) in lattice parameter with changes in composition. Agreement between the results of these studies and those of image computations or conventional analytical methods has not only promoted confidence in, but also revealed the superiority of, the lattice imaging technique.

3.4 Decomposition in Al-Zn

The Al-Zn phase diagram[140] shows a prominent miscibility gap at temperatures below about 350°C (Fig. 3). Precipitation for dilute alloys in this system has been reported[141-145] to follow the general sequence:

G.P. zones → rhombohedral R-phase → cubic α' → hexagonal Zn. However, at higher Zn concentrations ($\gtrsim$30 at %), there is evidence that α' formation is suppressed, and instead the R-phase transforms directly to Zn (refs. 146,147). In addition, the existence of a spinodal mode of phase separation has been reported[147-152] to occur for alloys aged well within the miscibility gap.

Several investigations[15,153-156] have also concentrated on the discontinuous mode of decomposition which is dominant in this system. In one case, cellular precipitation kinetics in an Al-28 at % Zn alloy have been accurately determined by means of in-situ hot stage transmission electron microscopy,[19,157] and revealed that boundary diffusion is rate controlling. Somewhat more peculiar reactions involving the discontinuous precipitation of R-phase lamellae[149,158,159] have also been analyzed with respect to morphology and diffraction effects.

At lower temperatures (below ~150° C) the morphology of the discontinuous reaction changes, resulting in a granular two phase distribution.[159,160] It was suggested that this reaction proceeds by autocatalytic nucleation on dislocations punched out by the Zn-rich phase.[160] No orientation change at the reaction front was detected and resolution was limited primarily due to a high density of R-phase precipitates and their associated strain fields.[159]

4. IMAGE COMPUTATION

Based upon the optics outlined in the previous section, computations have been performed to establish best conditions for lattice imaging of face centered cubic alloys. The program incorporates n beams along a systematic row to account for the effects of higher order dynamical interactions on the wave amplitudes ϕ_o and ϕ_g of the two image-forming beams. Input parameters include alloy composition and lattice constant, Miller indices of the operating reflection, number of beams, electron scattering factors and the accelerating voltage.

For this study, atomic scattering factors were computed using the electron scattering factors of Doyle and Turner.[161] Alloy structure factors (F_g) were then calculated using the approximation

$$F_g^{\text{Alloy}} = f^{(1)}F_g^{(1)} + f^{(2)}F_g^{(2)}$$

outlined by Head et al. where $f^{(1)}$ and $f^{(2)}$ are the atom fractions and $F_g^{(1)}$, $F_g^{(2)}$ the structure factors for pure components (1) and (2) respectively.

Wave amplitudes were determined using a matrix formulation of the many beam dynamical theory described by Hirsch et al.[45] which is based upon the eigenvalue equation:

$$A^{ij}C_g^{jk} = \gamma^k C_g^{jk} \quad .$$

The matrix $\underset{\sim}{A}$ has diagonal elements

$$A_{gg} = s_g$$

and off-diagonal elements

$$A_{gh} = \frac{1}{2\xi_{g-h}}$$

where s_g is the deviation parameter and ξ_g the extinction distance of the reflection g. Solving the equation yields a set of eigenvalues γ^k and column vectors $\underset{\sim}{C}_g^k$ whose elements are the Block wave amplitudes used in computing the total wave amplitude of a beam g (g = 0 or g) as a function of specimen thickness (z):

$$\phi_g = \sum_k C_o^k C_g^k \exp(2\pi i \gamma^k z) \quad .$$

Absorption effects were not taken into account. A total of 8 beams (systematic) were employed in each calculation.

An important practical consideration in lattice imaging is the variation in fringe visibility with crystal thickness, computed here by adopting a visibility (V) criterion[54] based upon wave amplitude:

$$V = \frac{2\phi_o\phi_g}{\phi_o^2 + \phi_g^2} \quad .$$

It is noted that maximum visibility (V = 1) occurs for $\phi_o = \phi_g$.

The typical calcomp output shown in Fig. 4 is a plot of fringe visibility for the {200} planes in an Al-10 at % Zn alloy. It is clear that with precise control over thickness during specimen preparation (e.g. by vacuum evaporation) success in obtaining high resolution images could be greatly enhanced. In this case, producing an exact foil thickness of 180 Å, 312 Å, etc. seems most favorable. However the breadth of the peaks and sharpness of the troughs also indicates that reasonable success can be expected with a bulk thinning technique. Similar behavior was found for all low index planes in three different alloys as well as pure Al.

In additional image computation, the intensity profile along a direction $\underset{\sim}{x}$ normal to the fringes given by[163]

$$I(\underset{\sim}{x}) = |\phi_o|^2 + |\phi_g|^2 + 2|\phi_o|\ |\phi_g| \cos 2\pi \underset{\sim}{g}\cdot\underset{\sim}{x}$$

was determined for the tilted illumination case. It is apparent from this equation that whereas visibility is maximum at $\phi_o = \phi_g$ for all values of the wave amplitudes, fringe intensity is maximum only for maximum ϕ_o and ϕ_g.

Figure 5 is a composite plot showing the intensity profile produced by the {111} planes in a crystal 300 Å thick. Plotted in arbitrary units, the intensity is given to the same scale for pure Al (solid line) as well as an alloy (dotted line) of 50 at % Zn (labelled). The values indicate that the addition of up to 50 at % Zn decreases the signal-to-background ratio for {111} lattice images by ~15%. Not all images are affected in the same way, however, since the signal-to-background ratio for {220} fringes increases by ~6% with the same degree of alloying. Data of this kind are most useful in studies of phase separation, where fringe visibility might be used to monitor solute content at high resolution within a multicomponent alloy. However it also stresses the necessity of detailed supplemental calculations in the quantitative interpretation of lattice images.

5. EXPERIMENTAL PROCEDURE

5.1 Materials Fabrication and Treatment

Alloys were fabricated from 99.999% purity Al and 99.993% purity Zn under Ar atmosphere and chill cast in 1 inch diameter crucibles. The ingots were then homogenized at 420°C for 72 hrs. and hot rolled to approx. 40 mils thickness. Sections were further cold rolled to approx. 5 mils. Following a solution anneal (15 mins. at 400°C), the sheet material was immersed in a silicon oil bath for aging at temperatures ranging from 185°C to room temperature. All aging treatments were terminated by an iced brine quench.

Two compositions were chosen for this study: a dilute (~10 at % Zn) alloy to concentrate on heterogeneous nucleation at grain boundaries in the absence of discontinuous effects and a higher Zn (~30 at %) alloy for analysis of discontinuous reaction products including those involving the R phase. Chemical analysis following all thermal-mechanical treatments revealed the actual compositions to be (in atomic %):

Alloy 1: 90.5 Al - 9.5 Zn

Alloy 2: 69.7 Al - 30.3 Zn .

Because of the known tendency for these materials to decompose at room temperature[156] all sheet specimens were kept refrigerated until thinned for foils, usually within the next 24 hours.

5.2 Specimen and Microscope Preparation

Foil preparation was carried out in a double jet polisher using a nitric acid-methanol electrolyte at -25° to -30°C. The polished foils were immediately placed in ethanol and again refrigerated until viewed within the next few hours in the microscope. The rigid

specimen requirements necessary for this study, viz. unetched grain boundaries and intact precipitates in the thinnest areas of the sample, were met by preparing a large number of foils just prior to each microscope session and choosing the best for imaging.

A Siemens Elmiskop 102 was used exclusively during this research, having been maintained throughout for high resolution performance. Microscope parameters (C_s = 1.9mm, C_c = 1.6mm) provided for guaranteed 2 Å resolution (line-to-line) over $\pm 45^\circ$ double-axis tilting, however additional modifications were made in order to facilitate lattice imaging. These included the use of pointed filaments for higher brightness and beam coherence, as well as a modified[164] conical bias shield, also supplied by Siemens. The filament tip was recessed 600µm below the bias shield aperture plane in order to optimize source intensity.[165] During lattice imaging the filament was consistently operated in a slightly undersaturated condition at a beam current of 8 to 10 µA, resulting in a mean filament lifetime of ~20 hours. Fringe visibility was enhanced by installation of a higher efficiency screen and a minor modification in lens circuitry which permitted direct image magnifications in excess of 800,000 times. In order to attain the necessary beam intensity at reasonable coherence, the first condenser was set at midpoint between being fully focused and fully defocused while a 200µm C2 aperture provided collimation. The second condenser was nearly always set at a fully focused condition.

Constant attention was given to microscope alignment and cleanliness, particularly in the area of the gun and specimen cartridge. Thin film apertures were used throughout the column, including the second condenser. In order to further prolong pointed filament life and

minimize specimen contamination, beam excitation was delayed until the column pressure fell below ~5 x 10^{-6} torr. Accelerating voltages were 125 kV and 100 kV.

5.3 High Resolution Transmission Electron Microscopy

Most of the foils examined in the course of this study showed a strong <001> texture, however other zone axes were brought into beam incidence, notably <110>, requiring the use of a high angle ($\pm 45^{\circ}$, biaxial) specimen tilt cartridge. Once suitable areas were found lattice imaging began immediately, followed by conventional and/or weak beam imaging with crystallographic data provided by selected area diffraction.

Success in obtaining lattice images was found to be greatest under the following experimental conditions:

5.3.1 Orientation

The foil was always tilted into a strong diffraction condition for the image forming beams. Proper orientation was easily assured by observing the image in dark field (displaced aperture was sufficient) and tilting until the area of interest became illuminated. A more rapid method, also used to correct for foil bending during lattice imaging, involved the location of the dark/light extinction contour pair originating from the transmitted and diffracted beams, respectively, within the objective aperture. In each instance the foil was tilted until the pair of contours (seen in a defocused image) intersected the grain boundary region being photographed.

5.3.2 Focussing

The exact focus condition was always determined by superposition of bright field (BF) and dark field (DF) images. It was found that this

procedure was most easily accomplished when viewing the edge of a perforation in the foil. However other internal boundaries including those of precipitates and grains were most frequently used. The procedure is roughly demonstrated in the next figure.

Figure 6(a) is a defocused two beam image of precipitates at relatively low magnification showing both the dark (BF) and light (DF) images which are made to coincide through manipulation of the objective lens current as shown in (b). Note also that the background contrast in (b) has become considerably more sharp. From this point of coarse superposition, fine focusing is accomplished by simultaneous correction of objective lens current and stigmators while viewing at high magnification (>400,000 X). At exact focus background phase contrast is at a minimum and a fringe image is formed.

For this research, minimum working magnifications of 500,000 times were employed while focusing through 10 X binoculars. Photographs were rarely attempted unless lattice fringes were visible on the screen. Otherwise a through-focus series in ~80 Å increments of defocus from +400 Å to -400 Å was found to be most useful.

5.3.3 Foil Thickness

Generally it was found that the thinner the foil, the greater the success in lattice imaging. Unfortunately most of the thinnest foil areas were lacking either grain boundaries or precipitates due to their having been etched away during specimen preparation. Choice of a suitable working thickness was then based upon the ability to achieve exposure times no longer than 8 to 10 seconds on Kodak E.M. film at the filament and condenser settings given above.

5.4 Lattice Image Analysis

Even at magnifications of 500,000 times, 2 Å lattice fringes are spaced only 0.1mm apart on a photographic negative and therefore demand more than routine visual analysis. During this study three methods were employed and often combined to increase accuracy. These are described below.

5.4.1 Photographic Enlargement

Direct enlargement of the negative up to ~18 times was used for visual inspection of fringe geometry as well as measurements of fringe spacings and angular misorientations. During enlargement a point source on the enlarger head and minimum grade 4 printing paper were used to enhance fringe contrast. Additional contrast and/or magnification was obtained when necessary by re-photographing high quality prints. Obviously at these magnifications dust and scratches were a constant nemesis sometimes avoided by sandwiching the cleaned negative between glass lantern slides and tape-sealing the edges.

5.4.2 Microdensitometer Scanning

A Joyce-Loebl MK III microdensitometer was also used in the analysis of fringe spacings. All scans were made directly on the appropriate negatives at a 50 : 1 magnification ratio. Measurements were then made of the peak-to-peak distances representing the lattice spacings imaged on the negative.

5.4.3 Optical Diffraction

Another method of evaluating fringe spacings on the lattice image negatives evolved from their similarity to standard optical gratings. When mounted in the ray path of a He-Ne laser at normal incidence, the negatives produced a Fraunhofer diffraction pattern

which was then related to the fringe spacings averaged over the illuminated area.[166] A standard optical diffractometer (e.g. see ref. 167) was used to obtain the optical diffraction patterns.

A method was then developed[168,169] for obtaining diffraction information from the specimen down to ~20 Å diameter equivalent areas. The technique basically utilized an aperture in the path of the laser such that selected area optical diffraction patterns were obtained. Optical microdiffraction was also employed in the present study for distinguishing individual diffraction effects in complex electron diffraction patterns and to ascertain the presence of lattice fringes which were imaged at low visibility.

A rigorous assessment of the accuracy involved in each of these techniques was performed using lattice images of evaporated Au films and a spinodally decomposed Au-Ni alloy, the former having a single well defined spacing and the latter a sinusoidal spacing variation. Details of this study are provided in the appendix.

6. EXPERIMENTAL RESULTS

6.1 Grain Boundary Precipitation

Lattice imaging was successfully applied to heterogeneously nucleated precipitates much less than 1000 Å in size (i.e. longest dimension). Although most of these particles were seen in a well-defined morphological state, some evidence was obtained for the early stages of formation of grain boundary precipitates. An example of the latter case is shown in Fig. 7.

The grain boundary region running diagonally in Fig. 7(a) was imaged under the diffraction conditions shown in 7(b). The foil was prepared from alloy 1 aged for 30 mins. at 180°C and exhibits some thickening at the grain boundary which reaches a maximum width of ~55 Å.

At higher magnification (Fig. 8(a)) the fringes produced by the $(1\bar{1}\bar{1})$ planes of the upper grain are clearly visible. In addition there are lower visibility fringes within the thickened grain boundary region which are rotated clockwise at a small angle from the matrix fringes. Using the 2.33 Å spacing of the $(1\bar{1}\bar{1})$ matrix planes[145] as an internal magnification standard, it was found that the matrix lattice fringe spacing is constant to $\pm$0.02 Å measurement error. On this basis, the fringes within the boundary region have a spacing of 2.36 $\pm$ 0.02 Å. The rotation angle is 2.8 $\pm$ 0.1°. Both spacing and angle agree qualitatively with the diffuse splitting seen in the electron diffraction pattern of Fig. 7(b); however no quantitative evaluation can be made from the pattern alone.

These results indicate that the larger spacing fringes actually represent a solute-enriched region independent of either bordering

grain. The presence of very weak rotational Moiré fringes found only within this region (outlined by white slash marks in Fig. 8(a)) further supports this description. The spacing and rotation angle of the Moiré pattern agree to within diffraction spot measurement error (~30% for this pattern) with the calculated values expected from the interference of the imaged second phase fringes and those lattice planes giving rise to the arrowed diffraction spike in Fig. 7(b) originating from the lower grain.

On the basis of its difference in interplanar spacings and rotation angle, the Zn-rich region was found to preserve its identity down to a thickness of ~6 to 8 Å (e.f. Fig. 8(b)), below which quantitative measurements were considered dubious. The total length of grain boundary exhibiting second phase fringes was found to be ~1500 Å. This was also the approximate length over which the boundary coincided with the trace of the (200) planes of the upper grain.

An example of a well-developed precipitate resulting from the same aging condition is shown in Fig. 9. By contrast analysis the dislocations seen at the boundary (arrowed in 9(a), invisible in 9(d)) are shown to have Burgers vectors $\underset{\sim}{b} = a/2[101]$ or $a/2[0\bar{1}1]$ associated with matrix slip dislocations, and from the weak beam image in 9(b), do not appear to be dissociated within the boundary region. Due to its greater resolution ($\underset{\sim}{s} \approx 0.01$ Å^{-1}) the weak beam image also reveals the presence of facets within the grain boundary precipitate which are not obvious in the other (BF) images of Fig. 9.

Similar facets were found in grain boundary precipitates of alloy 2 as the micrographs in Fig. 10 show. Here both DF (Fig. 10(a)) and lattice image (Fig. 10(b)) modes were applied to a specimen aged

1 min. at 135°C. Both images show Moiré fringes at the boundary/precipitate interface, and the presence of a "wedge" between the precipitate and boundary, shown boxed in 10(b). However an enlargement of the boxed region (Fig. 11) indicates the superior resolution of the lattice image.

As emphasized by the curved arrow in Fig. 11, the fringes within the lower wedge region remain continuous into the upper precipitate area. The poor visibility of the $(1\bar{1}1)$ matrix fringes in the lower grain prohibited their use as a standard for absolute d-spacing determination. Nevertheless it is apparent from micrograph measurements that the fringes within the wedge area have a 1.6% larger spacing than those within the precipitate area, indicating again a higher Zn concentration in the lower wedge than in the precipitate. The sharpness of the image allowed measurement errors to be maintained under 1%. By locating a few well-defined $(1\bar{1}1)$ fringes in the lower grain, their misorientation with respect to the precipitate fringes was measured at $3.5 \pm 0.5°$, thereby confirming the origin of the interfacial Moiré pattern.

Sharp facets were also observed at the growth edge of grain boundary precipitates (i.e. opposite the face where nucleation at the boundary occurred), but again only under conditions of enhanced resolution. The example in Fig. 12 (alloy 1, 30 mins. at 180°C) demonstrates the effect of increasing the deviation parameter in DF imaging. At $s = 0$ (Fig. 12(a)) a precipitate is seen residing at a grain boundary parallel to an (002) matrix trace and containing perturbations in contrast (arrowed). However as s is increased to $s \approx 0.004$ Å^{-1} (12(b)) and finally $s \approx 0.01$ Å^{-1} (12(c)), the upper surface facet (arrowed in (c)) and boundary dislocation net become clearly delineated.

Another specimen of the same batch is shown at higher resolution in Fig. 13 to have a nearly identical grain boundary precipitate morphology. The planar facet in 13(a) extends into a grain (2) whose (200) trace parallels the grain boundary. It is also seen by comparison with the oriented diffraction pattern in 13(b) that the facet parallels the (200) trace of the neighboring grain (1). However additional detailed analysis of this lattice image, which shows fringes in the grain boundary precipitate (trace "P") as well as both bordering grains (traces "1" and "2"), provides considerably more crystallographic and chemical data.

Using the high visibility (200) fringes in grain (2) as a magnification standard, their spacing (2.02 Å) was measured to $\pm$0.01 Å. By comparison, the precipitate fringes were found to be spaced 2.09 $\pm$ .01 Å, indicative again of higher solute content. The rotation angle (θ) between matrix (2) and precipitate fringes was determined from both lattice image and SAD measurements to be 9.2 $\pm$ 0.1°. Application of the formula presented in Sec. 2.1 allowed the measured spacing (d) and rotation angle (ρ) of the boundary structural lines to then be compared with calculated values (see also Fig. 1). The results

$$d_{meas.} = 12.2 \pm 0.5 \text{ Å} \qquad d_{calc.} = 12.4 \pm 0.2 \text{ Å}$$

$$\rho_{meas.} = 106.5 \pm .5^\circ \qquad \rho_{calc.} = 107 \pm 1^\circ$$

indicate that the plane matching (PM) model[37] of grain boundary structure can be given direct quantitative verification by lattice image analysis.

Additional direct evidence of plane matching is obvious from Fig. 14 which is a high magnification image of the boundary region arrowed in Fig. 13(a). Here it is seen that continuity of lattice planes across the boundary is for the most part preserved. All mismatch

accommodation is seen to occur within the high density Moiré bands as evidenced by the presence of terminating fringes (arrowed). These terminations furthermore suggest that misorientation dislocations with a Burgers vector equal to the interplanar spacing[27] may be associated with the misfit lines.

Lower magnification images of misfit lines at grain boundary precipitate interfaces were found to exhibit the general appearance shown in Fig. 15. It is noted that in this foil (alloy 2 aged 1 wk. at room temperature) the grain boundary again follows the trace of the (002) matrix planes from the lower grain. The misfit lines barely visible in 15(a) are given enhanced visibility by weak beam imaging ($s \approx 0.006$ $\mathring{A}^{-1}$) in 15(b) where they are also seen on the neighboring precipitate (arrowed in 15(b)). Figure 15(a) also reveals a ledged structure (arrowed) along one of its facets, where the faces of the ledges appear to coincide with the traces of the $(1\bar{1}1)$ and $(\bar{1}\bar{1}\bar{1})$ planes of the lower matrix grain. It was shown above (Figs. 13,14) that lattice imaging provides a unique advantage in the analysis of structural Moiré lines; the example below is an application to the analysis of microledges in grain boundary/precipitate interfaces.

Figure 16 is a low magnification lattice image of a grain boundary precipitate in alloy 1 aged 30 mins at 180°C. There appear to be two primary facets along the right hand boundary, indicated by the boxed regions (1) and (2). At higher magnification (Fig. 17(a)), it is seen that facet (1) is composed of a number of microledges (arrowed) of 1 or 2 atom layer thickness which maintain the interface exactly parallel to the $(\bar{1}\bar{1}1)$ planes of the neighboring grain. In this case the fringes in the bordering grain are imaged at low

visibility; however their trace has been indicated by the long double arrow. In Fig. 17(b), facet (2) is seen to be exactly parallel to the precipitate fringes and atomically flat except for the presence of microledges (arrowed) which protrude by 1 or 2 atom layers into the neighboring grain.

An extended analysis of the precipitate/matrix interfaces shown at high magnification in Fig. 18 was also performed by optical microdiffraction. The results are given in Fig. 19. It is seen that at region (1) in Fig. 18(a), the laser detected two primary periodicities of nearly equal intensity shown by the split spots in Fig. 19(a). At the opposite boundary, i.e. region (2) in Fig. 18(a), the optical diffraction pattern (Fig. 19(b)) showed the arrowed higher angle spot to be weaker and rotated clockwise with respect to the more intense low angle spots. Reference to the lattice image (viz. Fig. 17) reveals immediately that the low intensity spot corresponds to the low visibility matrix fringes. Hence from the relative spacings of the optical diffraction spots, the Zn-rich precipitate is again shown to have the larger interplanar spacing in spite of the inability to measure the spacing of the matrix fringes. Identical results are obtained in Figs. 19(c) and (d) corresponding respectively to regions (1) and (2) of the lower half of the precipitate shown in Fig. 18(b). From quantitative measurements of these patterns, the interplanar spacings in the vicinity of precipitate interface are found to be:

$$d_{matrix} = 2.33 \pm 0.02 \text{ Å}$$

$$d_{precipitate} = 2.47 \pm 0.03 \text{ Å} \quad .$$

It is also apparent that the laser detected a much larger periodicity corresponding to the lower angle spots arrowed in Fig. 19(c) but present as well in the other optical diffraction patterns. Measurements show that the inner spots correspond to exactly twice the spacing of the precipitate fringes. Their origin will be treated later in the presentation of Fig. 27.

The cumulative results above show definitively that during precipitation the Zn-rich regions of the lattice are expanded along <111> directions with respect to the Al-rich matrix. The effect of this lattice expansion along a single [111] direction in reciprocal space is shown schematically in Fig. 20. The dotted lines represent a $[1\bar{1}0]$ reciprocal lattice section which upon addition of Zn is compressed along [111], producing the rhombohedrally distorted lattice of solid lines. Experimentally, this effect has been observed in split diffraction spots (cf. Figs. 7(b), 13(b), 19).

An attempted direct measurement of this effect on the actual lattice at a grain boundary region is presented in the next figure. Based upon its parallel arrangement of matrix $(1\bar{1}1)$ fringes and rhombohedrally distorted precipitate fringes, measurements were made across the grain boundary at region (1) in Fig. 18(b). Each measurement included 5 fringes, advancing by 1 fringe each time. The plot shown in Fig. 21 reveals that to within measurement error (an error bar representative of each point is shown on the 1st data point), the spacing is constant within both matrix and precipitate regions, and changes abruptly across the grain boundary (dotted line).

Somewhat different behavior is observed however when the measured {111} fringes are not parallel to the grain boundary. For

this latter study, the grain boundary precipitate shown in Fig. 22 was chosen. Alloy and aging conditions for this specimen are identical to those immediately above. Measurements were performed in the area of the boxed region in 22(a) shown enlarged in 22(b), by 10 fringe groups, advancing by ~1 fringe width normal to the boundary at each measurement. The results are plotted in Fig. 23 and indicate a decreased fringe spacing suggestive of solute depletion as the boundary (dotted line) is approached from either matrix or precipitate side. An error bar representative of each measurement is again shown on only the first point.

Concomitant with the observed change in fringe spacing is an accommodation of matrix strain which is also revealed in the lattice images. Figure 24 is an enlargement of the grain boundary in Fig. 22 (precipitate at bottom), showing the boundary in an edge-on configuration. The solid arrowed lines trace continuous fringes across the boundary between which there are 48 fringes in the matrix and 45 fringes in the precipitate. However the fringes still appear to exhibit a high degree of continuity across the boundary except for an occasional terminating fringe. One example on the matrix side is indicated by the open arrow.

In other regions of the boundary still in an edge-on orientation strain accommodation appears to be less localized. The region between the open arrows in Fig. 25 shows an apparent disruption in continuity distributed over ~7 or 8 lattice planes. It is emphasized that this is not due to a change in foil thickness, the effects of which are demonstrated in an adjacent area of the same image. The black and white arrow passing through the darkened region of a thickness extinction contour connects a dark fringe from the precipitate with a light fringe from the matrix.

A final example from the same boundary in an inclined orientation is presented in Fig. 26. The curved arrow on the left points out the exaggerated fringe bending which occurs during preservation of fringe continuity across the boundary. In the region between the solid arrows the observed drastic bending can most likely be attributed to a change in thickness[78] as the boundary becomes more sharply inclined. Nevertheless the lattice images shown here directly reveal the structural continuity resulting from plane matching at an interphase boundary.

The last example of heterogeneous precipitation at grain boundaries, shown in Fig. 27, is taken from alloy 2 aged 1 wk. at room temperature. Using the diffraction conditions in 27(b), a lattice image of the boxed region in 27(a) was obtained and is shown at high magnification in the next figure. The resulting micrograph (Fig. 28) clearly reveals the presence of $(1\bar{1}1)$ matrix fringes having a spacing of 2.33 Å and able to be measured at $\pm$0.01 Å accuracy. Based upon this standard, the spacing of the fringes within the precipitate was found to be 4.90 $\pm$ 0.02 Å. Both of these values showed excellent agreement with the spacings of the $(1\bar{1}1)$ and weak (arrowed) precipitate reflections within the objective aperture (Fig. 27(b)).

The value of the precipitate fringe spacing measured here agrees with that (4.947 Å) given for the c-axis dimension[143,146] of the rhombohedrally distorted Zn-rich phase found in the Al-Zn system. However, based upon structure factor considerations, the (0001) reflection is not allowed for rhombohedral symmetry, nor can it be obtained by double diffraction.[170]

In more recent x-ray experiments,[145] it has been suggested that the Zn-rich phase exhibits hexagonal symmetry, and the c-axis dimension in this study (4.936 Å) is even more closely related to the value measured above. Furthermore it is shown schematically in Fig. 29 that the (0001) Zn reflection can occur by double diffraction. In this figure the [110] fcc pattern is superimposed on a $[11\bar{2}0]$ hcp pattern where the position of the (0001) reflection made possible by double diffraction is enclosed by parentheses. It is concluded that the indicated 4.9 Å fringes and the double periodicity spots seen in Fig. 19 are due to hexagonal Zn.

The presence of these fringes in the lattice image of Fig. 27 is further verified by the microdensitometer traces shown in Fig. 30. At the top is a segment of a trace from the matrix region alone, while the bottom segment, shown to the same scale, is from the precipitate region alone. It was additionally found that in regions near the interphase interface both periodicities were detected by microdensitometer analysis (Fig. 31(a)) as well as optical microdiffraction (Fig. 31(b)).

It is also noted that the precipitate in Fig. 28 is revealed to be completely enveloped by the matrix phase, not only from the upper grain in which nucleation occurred, but also at the growth front, as evidenced by the thin 20 - 50 Å region of $(1\bar{1}1)$ fringes at the perimeter of the precipitate. The presence of these (and all other) fringes in the micrograph was found to be unaffected by changes in focus during an entire -320 Å to +320 Å through-focus series.

6.2 Role of Grain Boundary Defects

The severe restrictions on specimen thickness necessary for lattice imaging often prevented its application to analysis of defect

structures within grain boundaries and studies of their role in heterogeneous precipitation. Relatively thick foils were required to obtain sufficiently wide images of grain boundaries in order to identify defect substructures. Presented below is a summary of some conventional T.E.M. observations on this topic.

The micrograph in Fig. 32 shows two images of the same low angle grain boundary in alloy 1, aged 30 mins. at 180°C. Analysis of the corresponding electron diffraction patterns shows that the boundary is primarily twist ($5.9 \pm 0.5^{\circ}$ about $[\bar{2}00]$) with a small tilt component ($2.5 \pm 0.3^{\circ}$ about $[001]$). The boundary plane is also found to be near the (220) trace of the right hand grain.

By diffraction analysis the dislocation net visible in 32(a) is found to be composed of lattice dislocations having a Burgers vector $b = a/2[1\bar{1}0]$. Under the diffraction conditions in 32(b), the dislocations are no longer visible but an array of closely space lenticular precipitates are seen to reside at the boundary with their long dimension parallel to the dislocation lines. These results strongly suggest that it is the defect substructure of the low angle boundary, rather than merely the boundary itself, which catalyzes precipitate nucleation.

In another example the same specimen shows aligned arrays of equiaxed particles, rather than single long precipitates as noted above, within the boundary plane (Fig. 33(a)). Although the boundary in this case is pure tilt ($10.1 \pm 0.2^{\circ}$ about $[1\bar{1}0]$), it is also found to parallel a $(2\bar{2}0)$ trace of the matrix, as in Fig. 32.

A different behavior is noted however when the boundary plane is parallel to the lower index {200} family of matrix planes. The example in Fig. 33(b) shows that for this low angle tilt boundary

($7.5 \pm 0.2^{\circ}$ about [001]), the precipitates reside upon the boundary as hemispherical caps with their long dimension running along the grain boundary, transverse to the line direction of the dislocation net. Hence under these conditions the defect structure comprising the grain boundary appears to have no particular effect on heterogeneous precipitation.

At high angle boundaries, defect structures were also observed to bear a close relationship with grain boundary precipitates. An example of extrinsic grain boundary dislocation behavior is shown in Fig. 34. The arrowed dislocations in 34(a) and 34(c) derive their extrinsic character from being partially contained within the matrix. It is observed however that each of these dislocations makes contact with a precipitate at the boundary. Under weak beam conditions (Fig. 34 (b), $s \approx 0.01\text{Å}^{-1}$) the dislocation arrowed in 34(a) is seen to pass around the large precipitate at the center of the micrograph and continue through the boundary to the precipitate at the upper left. The larger size of the interconnected precipitates compared to those not included in the extrinsic dislocation net (e.g. at lower right) may indicate the effectiveness of these defects in enhancing growth kinetics.

The micrograph in Fig. 35 shows another high angle boundary which is characterized by nearly continuous matching of the (002) planes from both bordering grains. An extrinsic dislocation from the lower grain is shown by the long arrow in 35(a) occupying a position at the precipitate/matrix interface. However an intrinsic dislocation network is also indicated by small arrows and shows increased density at regions of increased boundary curvature (35(a)) and near the precipitate (35(b)). These observations suggest that the intrinsic dislocations may facilitate boundary motion during the growth of grain boundary precipitates.

6.3 R-Phase Discontinuous Precipitation

Observations on the R-phase discontinuous reaction were made using samples of alloy 2 aged for 15 mins. at 185° C. As shown in Fig. 36, the reaction proceeds by the growth of alternating lamellae of the Al-rich matrix phase and (in thin bands) the R-phase. The lamellae cluster in colonies and grow until impingement, leaving a denuded region near the boundary in some cases (36(a)), but not all (36(b)). Electron diffraction evidence from the impingement boundaries suggest that the colonies are only slightly misoriented in agreement with earlier reports.[158] It is also seen in Fig. 36 that subsequent precipitation occurs within the Al-rich lamellae under the influence of residual supersaturation.

In foils where impingement was not complete, the reaction front was seen (Fig. 37) to be severely affected by the presence of the discontinuous product. The arrowed cusps in Fig. 37(b) indicate a strong surface tension at the interlamellar boundaries. In this micrograph the R-phase lamellae in the right hand grain are shown to be etched away during foil preparation. Nevertheless their edge-on orientation reveals a smooth curvature at the point of termination (arrowed in 37(a)).

A more detailed view of an intact lamellar termination is shown in Fig. 38 where it is revealed that mismatch is accommodated by a single lattice dislocation, arrowed in 38(a). Contrast analysis indicates a Burgers vector equal to a/2[110]. The weak beam image in 38(b) also suggests that the tip of the terminated lamella (arrowed) is continuously curved.

At higher magnification, an interlamellar boundary appears as shown in the dark field image of Fig. 39(a). The stark Moiré contrast obviously obscures all boundary structural detail in this image, which is to be compared with a lattice image formed under the diffraction conditions shown in 39(b).

The fringes in Fig. 40 are clearly visible through the high density Moiré bands and show terminations (arrowed) which suggest that accommodation of misorientation strain occurs within these regions. The origin of this misorientation is revealed in the following lattice image (Fig. 41) taken near the lamellar termination. Direct measurement is possible from the micrograph and indicates that the {111} planes within neighboring lamellae are misoriented by $2.0 \pm 0.5^{\circ}$. Hence this application of lattice imaging reveals directly that a large contribution to diffraction spot splitting in SAD patterns (cf. Fig. 39(b)) of the R-phase discontinuous product is made by the misorientation of individual lamellae and not just the misorientation between colonies of lamellae as previously reported.[158]

6.4 The Low Temperature Discontinuous Reaction

After aging alloy 2 at room temperature for 2 wks. the low temperature discontinuous reaction was found to be sufficiently advanced for study. Its general morphology is revealed in Fig. 42(a), indicating that random colony growth is not confined to grain boundary regions, but may also pervade the matrix from isolated growth centers. Of particular interest during this study was the nature of the reaction front.

The boxed region at the periphery of a colony shown in Fig. 42(b) is imaged at high resolution in Fig. 43. The resulting lattice image

of the (200) matrix planes is sufficiently sharp to be measured to within $\pm$ 0.5% error limits. A rigorous study incorporating direct fringe measurement and optical diffraction in the vicinity of the growth front completely surrounding a colony up to the grain boundary of its origin failed to reveal any change in fringe spacing or orientation in the affected region. Fringes were continuous through both colony and matrix, losing visibility only in the areas of the Zn-rich precipitates (e.g. Fig. 43, lower left-hand corner). Since the lattice image was unaffected by the high density of matrix R-phase precipitates, this study provides definitive evidence for a lack of any change in orientation or composition within the matrix across the growth front.

Stereo analysis (Fig. 44) indicates that in the region studied, the discontinuous product was continuous through the depth of the foil, and not merely a surface-nucleated reaction. Verification was provided by stereo pairs at both the grain boundary vicinity (44(a)) and within a matrix colony (44(b)).

7. DISCUSSION

7.1 Structural Analysis

The usefulness of the lattice imaging technique in grain boundary structural analysis is graphically illustrated by its success in providing the first direct substantiation of the plane matching model.[37,38] Characteristic linear contrast features like those seen at the grain boundary precipitate interface in Fig. 13 are shown by this study to be structural in nature, rather than a mere optical interference pattern (Moiré). The lattice image directly reveals the presence of terminating fringes in boundary regions of high opacity, indicating that mismatch accommodation takes place within actual boundary regions having high atomic density. It should be noted that these periodic structural features are not associated with either matrix, but are an intrinsic characteristic of the interphase interfacial structure. In Pumphrey's description[27] the misfit lines represent dislocations with Burgers vectors equal to the interplanar spacing. A direct visual representation of this effect is provided in Fig. 14.

It would of course be advantageous to correlate similar high resolution observations on intrinsic dislocations (e.g. Fig. 35) with the CSL model, particularly since Burgers vector identification may be extremely difficult using conventional techniques.[56] Unfortunately in order to apply the CSL model, the axis/angle description of the boundary must be known with high precision, requiring the presence of Kikuchi lines in electron diffraction patterns.[77-82] This condition is obviously prevented by the use of thin foils necessary for lattice imaging; therefore such correlations were not attempted during this research.

Nevertheless, insight into the mechanisms of growth of grain boundary precipitates is considerably enhanced by high resolution analyses. An example from this research is the detection of 1 to 2 atomic layer microledges at the growth front of the grain boundary precipitates in Fig. 17. In conjunction with the observed near perfect flatness of the precipitate facets, this finding is a strong indication for a ledge mechanism of precipitate growth, where the ledges are less than 5 Å high. It is noted that these defects are present on both facets, demonstrating that they are an integral structural feature of the precipitate and hence responsible for the development of precipitate morphology.

As an additional consequence of its superior resolution capabilities, lattice imaging has shown a distinct advantage in overcoming the gross contrast features associated with interfacial structure. Reference to Fig. 40 demonstrates this effect at a Moiré boundary very poorly represented in a conventional image (cf. Fig. 39). The lattice fringe terminations within the boundary again indicate periodic structural relaxation at the same relative positions with respect to the high density Moiré bands. This structural component to the Moiré interface furthermore suggests the presence of a mismatch strain which is believed to be responsible for the high surface tension effects induced by the interlamellar boundaries on the R-phase discontinuous reaction fronts (Fig. 37). The existence of a mismatch strain is consistent with both the lamellar misorientation evident in the lattice image of Fig. 41, and the contracted fringe spacing (~2.2 Å) observed in the vicinity of the boundary (Figs. 40,41) relative to the matrix fringe spacing (2.3 Å) at some distance from the boundary.

7.2 Compositional Analysis

The interplanar spacings determined from this study for well developed precipitates (e.g. Figs 21,23) are in excellent agreement with prior x-ray results.[143,145,146] However the use of an internal magnification standard permits equivalent accuracy in considerably more localized regions with the lattice imaging technique. The results of the analysis on Fig. 8 indicates that compositional changes at grain boundaries producing lattice parameter variations of only 1.28% can be detected within ≈10 Å of the boundary plane. Significantly, this level of resolution was observed in spite of very dubious electron diffraction evidence (Fig. 7(b)). Data of this kind indicates the potential for similar lattice imaging studies of solute or impurity segregation at grain boundaries.

By extension to precipitate growth, a comparison of Figs. 9(b) and 11 reveals that although the weak beam image accentuates a difference in structure factor between "wedge" and precipitate regions (cf. the nature of the thickness contours), the lattice image identifies its origin. It is suggested, especially in view of its relative size in Fig. 9(b), that the wedge region may have been formed during the quench or during a short duration at low temperature where the decomposition tie line extends to higher Zn concentrations. Afterwards it obviously provides an acceptable substrate for precipitate growth at higher aging temperatures.

Unfortunately no evidence was obtained on solute concentrations within the Zn-rich phase of the low temperature discontinuous reaction (Fig. 43). As such the mechanism of the reaction remains uncertain; however it is suggested by the lack of detectable orientation or matrix

composition changes across the reaction front that only a small driving force may be necessary to propagate the reaction.

Although all compositional analysis of lattice images performed during this research consisted of fringe spacing measurements, the results of Sec. 4 above indicate that fringe visibility is also a function of composition (e.g. see Fig. 5). Obvious differences in fringe visibility were noted in this study, but they were more often due to variations in diffraction condition (e.g. Fig. 28). Only in Fig. 11 was it found that the higher Zn region, in addition to appearing darker in some areas, also showed a higher visibility (i.e. more intense dark fringes for the same level white fringes) than the lower Zn precipitate. No quantitative evaluations of fringe visibility were attempted in the present study; however compositional analysis by this method may be a viable alternative to direct measurements in systems characterized by a small difference in component lattice parameters.

In contending with low visibility fringes, the advantages of optical diffraction analysis are clearly revealed by this research. Its use in Fig. 19 is indicative of the accuracy which can be obtained ($\pm$ 1-2% error) in compositional analysis despite the poor quality of the lattice fringes surveyed (cf. Fig. 18). Similar problems with low visibility fringes are to be expected when lattice imaging grain boundary regions due to the misorientation of contiguous grains.

The extreme sensitivity of the optical diffraction method under these circumstances is demonstrated below for the lattice image in Fig. 45. The darkened region at the center of this micrograph is a precipitate residing at the (vertical) grain boundary. Shown in the left-hand grain at high visibility is the 1.4 Å fringe image of the (220)

matrix planes. In addition, a set of $(01\bar{1}2)$ precipitate planes are seen at very low visibility to pervade the darkened image region. These observations correspond well with the intense (220) and weak $(01\bar{1}2)$ reflections included within the objective aperture during image formation (Fig. 46(a)). However the optical diffraction pattern (Fig. 46(b)) taken from Fig. 45 reveals that two additional periodicities have been recorded in the lattice image. These are (1) the $(1\bar{1}02)$ precipitate reflection (large arrow in 46(a)) and (2) the result of an interference between $(1\bar{1}02)$ and $(01\bar{1}2)$ precipitate reflections (excluding the transmitted beam). Although the latter fringe image serves no useful purpose in compositional analysis, it illustrates the usefulness of optical diffraction in applications to negatives of questionable fringe visibility. Notably this example demonstrates that optical diffraction is capable of revealing spatial periodicities on negatives which appear completely blank by visual inspection.

7.3 Effect of Boundary Plane on Precipitation Behavior

Although every effort was made to obtain as wide a sampling of grain boundary precipitation as possible in the Al-Zn system, the micrographs resulting from this research indicate that particular orientations of the grain boundary plane are strongly favored as reaction sites. In Figs. 7, 12, 13, 15, 33(b), and 34 heterogeneous nucleation is observed to have occurred at grain boundaries which parallel a {200} trace of one of the bordering grains. In Figs. 9, 16 and 27 the boundary plane parallels a {111} matrix trace. Furthermore, by high resolution analysis, distinguishing characteristics of each of these boundaries have been observed.

The most significant difference, revealed by compositional analysis of the lattice images, is that precipitates at {111} boundaries appear to have attained equilibrium composition. Evidence is provided by the (0001) reflections in the optical diffraction patterns (Fig. 19) from Fig. 16 and the direct lattice image of these planes visible in Fig. 28. Hence boundaries of this orientation appear to provide a distinct advantage in the kinetics of grain boundary precipitate growth. The observation of macroledges (Fig. 15) and microledges (Fig. 17) along {111} orientations suggest an obvious structural impetus for rapid decomposition. It is also noted that in lattice images of {111} planes normal to grain boundaries (for identically aged foils) no evidence of total decomposition has been obtained (e.g. Figs. 7,22). The slight misorientation between matrix and precipitate fringes ($\theta \approx 3$ to 6°) as well as direct fringe spacing measurements (e.g. Fig. 23) reveal a rhombohedral distortion characteristic of the intermediate phase.[143]

Alternatively, {200} boundaries appear to be energentically favorable in spite of their structural deficiencies for enhancing kinetics. It is seen that even in Fig. 16 where a {111} boundary habit is observed, the left-hand border of the precipitate shows a facet approaching an {002} trace. At lower resolution, Figs. 32 and 33 indicate that for those low angle boundaries not parallel to a {200} matrix trace, defect substructure dominates the catalysis of the precipitation reaction. However in the case of exact {200} coincidence, the precipitates appear to be unaffected by the low angle boundary dislocation net (Fig. 33(b)). The lattice image in Fig. 13 also reveals that at low angle tilt boundaries where conditions are favorable a precipitate nucleated on a (200) boundary of one grain will establish

a facet paralleling the (200) trace of the other grain. Clearly at the observed level of resolution the ability to define crystallographic directions is greatly enhanced and extremely beneficial to this type of analysis.

7.4 On Imaging the Zn Basal Planes

From crystallographic considerations it is anticipated that the (111) fcc Al-rich matrix planes in the Al-Zn system should act as a habit for (0001) hexagonal Zn precipitate growth. This orientation relationship has in fact been documented experimentally by x-ray studies.[145] Nevertheless the appearance of (0001) fringes in the lattice images of Figs. 16 and 28 (seen in the former only by optical diffraction analysis) was unexpected. These images reveal directly an orientation relationship of the type

$$(111)_M^{fcc} \;//\; (0001)_p^{hcp}$$

in spite of the structure factor rules[170] forbidding diffracted intensities at (0001) hcp reciprocal lattice positions.

The origin of the forbidden reflections in SAD patterns from double diffraction (cf. Figs. 27(b) and 29) is responsible for the appearance of a 4.9 Å periodicity in the lattice images. It has been shown (Fig. 46) that spurious periodicities may result in fringe images from the interference of unwanted beams within the objective aperture. However in the present case compositional analysis reveals the spacing expected of the Zn basal planes to $\leq$0.5% error. It is emphasized that the information contained in the lattice image is no less accurate because it originates from a doubly-diffracted beam. The lattice planes responsible for double diffraction are located only within the hexagonal precipitate, hence the lattice image reflects the structure

of only the pure Zn region. This effect was also observed in lattice images produced by beams arising from double diffraction at grain boundaries in thin film bicrystals.[139]

With the inclusion of a third beam in the objective aperture (Fig. 27) analysis of the lattice image in Fig. 28 becomes more difficult. Unfortunately the imaging of $(1\bar{1}1)$ fringes at the periphery of the precipitate in this figure was not duplicated in any other specimen during this research, and may in fact be unique to this particular 3-beam case. Due to the considerable variation in visibility with thickness (Fig. 4) computed for the 2-beam case above, it is possible that a similar effect may augment {111} fringe visibility at the thinner regions of the precipitate area if some overlap with the matrix occurs. A more conclusive analysis of this figure awaits further comparison with 3-beam computed images.

7.5 Comments on Structural Models

The direct visual verification of plane matching conditions at interphase boundaries provided by this research is a singular achievement of increased resolution. In fact the plane matching model was tailored to T.E.M. observations of grain boundaries using conventional imaging modes.[37,38] Higher resolution clearly makes possible the examination of such models on a much finer scale.

Consequently the high resolution results presented here suggest that in studies of grain boundary reactions, emphasis should be placed on the nature of the boundary plane with respect to both bordering crystals rather than the transition superlattice which continuously spans the boundary. The selection of a reaction site in the Al-Zn system appears to be strongly affected by the ability of the

precipitate to satisfy a low-index plane-matching relationship with one of the grains bordering the grain boundary. Hence the structure of the boundary described in terms of any of the transition lattice models[24-27] assumes a far less significant role.

In his treatment of the role of "special" grain boundaries in precipitate nucleation, Pumphrey[107] argues that grain boundary precipitates are likely to seek a habit plane relationship with one of the matrix grains in order to reduce surface and strain energies. He further adds that the differences in these energy terms resulting from variations in boundary structure are of secondary importance. Clearly the results of the present study show fundamental agreement with this description.

A particular advantage of the CSL or O-lattice models is the ability to precisely describe the defect structures at grain boundaries.[26,43] Such information is especially helpful when the bordering grains are misoriented at relatively high angles. However the only results obtained above which indicate a preference for nucleation on mismatch defects are for low angle boundaries where the dislocation network is composed of lattice defects. In addition such boundaries are not parallel to low index matrix planes and the general nature of the reaction is more accurately described as heterogeneous nucleation on dislocations rather than grain boundary precipitation.

It has been emphasized[171] that grain boundary structural models are presently capable of elucidating only the equilibrium configuration of grain boundaries. Obviously during the course of a grain boundary reaction there is considerable opportunity for dynamic change which questions their applicability. Definitive conclusions on the accuracy

of such structural models are therefore dependent upon further applications of high resolution electron microscopy as demonstrated here.

8. SUMMARY AND CONCLUSIONS

A review of previous experimental and theoretical investigations into the relationship between grain boundary structure and boundary-nucleated phase transformations indicated the need for high resolution research in this area. A study was undertaken in which lattice imaging and conventional transmission electron microscopy were applied to an analysis of grain boundary reactions in the Al-Zn system. Included in the study were computer image calculations to aid in the interpretation of fringe images based upon applications of fringe spacing measurements, microdensitometer traces and optical diffraction analysis. Three reactions associated with grain boundaries in the Al-Zn system were investigated: heterogeneous nucleation at grain boundaires, discontinuous precipitation involving the R-phase and the low temperature discontinuous reaction. The following conclusions have been drawn.

(1) Structural effects at grain boundaries are secondary to the orientation of the boundary plane in promoting effective nucleation of grain boundary precipitation reactions. In the Al-Zn system, boundary segments which parallel the trace of a low index matrix plane are energetically favored reaction sites. Boundaries parallel to a {111} matrix trace show an additional kinetic advantage.

(2) The first direct substantiation of the plane matching model has been obtained by lattice imaging at interphase interfaces of heterogeneously nucleated grain boundary precipitates. Structural relaxation occurs within the plane matching boundaries at positions of high atomic density.

(3) Regions of solute enrichment extending ≤ 10 Å from a grain boundary plane can be identified by lattice image analysis.

(4) Heterogeneously nucleated grain boundary precipitates in {111} matrix habit relationships grow by propagation of microledges, one to two atom layers in thickness.

(5) Composition profiles in both matrix and precipitate phases can be detected in lattice images to within ~10 Å of the boundary plane.

(6) The discontinuous R-phase reaction in higher Zn alloys is characterized by a $\leq 3^{\circ}$ misorientation between neighboring lamellae. Mismatch strain is accommodated by structural relaxation within the boundary and lamellar terminations can be effected by a single matrix dislocation.

(7) The low temperature discontinuous reaction exhibits continuity in orientation and composition across its reaction front within the Al-rich matrix phase.

(8) Lattice imaging has demonstrated superior capabilities in structural and chemical analysis at grain boundary regions. Errors of $\leq 1\%$ can be achieved by only 10-fringe samplings from enlarged micrographs when using internal magnification standards. Optical diffraction is particularly beneficial in enhancing fringe visibility and circumventing aberration errors during microdiffraction studies.

ACKNOWLEDGEMENTS

The author takes pleasure in acknowledging the encouragement and support of Professor Gareth Thomas who guided this research with active interest. Deep appreciation is extended to Dr. Robert Sinclair for his patient instruction in lattice imaging and enjoyable working companionship. Helpful discussions with Professor Robert M. Glaeser, Dr. David R. Clarke and Dr. David G. Howitt are also gratefully acknowledged.

Research facilities and technical staff were provided by the Energy Research and Development Administration through the Materials and Molecular Research Division of the Lawrence Berkeley Laboratory. Financial support was obtained by a grant from the National Science Foundation.

The author remains forever obligated to his wife Andrea, his daughter Kristin and his son Damian for their indulgence during the many hours spent away from them.

APPENDIX

Applications of Lattice Imaging in Compositional Analysis: An Assessment of Experimental Accuracy

A. Introduction

The ability to determine crystalline interplanar distances by direct measurement of fringe spacings is an extremely attractive feature of the lattice imaging technique. It follows that with proper care in choice of imaging conditions, magnification standards and statistical analysis, lattice imaging can be used to determine composition variations essentially at the atomic plane level. The purpose of this section is to describe the limits of accuracy associated with the detection, measurement and use of lattice images in chemical analysis.

B. Methods

A pictorial summary of the three methods used during this research for lattice image analysis is presented in Fig. 47. They are respectively (a) measurements of fringe separation distances in enlarged micrographs, (b) measurements of peak-to-peak distances in microdensitometer traces across lattice image negatives and (c) measurements of diffraction spot spacings in optical diffraction patterns also taken from lattice image negatives. In this figure, all three techniques are illustrated for an evaporated Au film formed by [001] epitaxial deposition onto a heated NaCl substrate. Due to its absolute regularity in (200) d-spacing such a specimen provides for highly accurate evaluations including identification of spurious effects introduced by experimental procedures.

(1.) Direct Image Measurement

Success in obtaining accurate measurements from enlarged micrographs is fundamentally enhanced by high quality printing. The negative must be maintained flat, dust free and in focus to assure faithful reproduction in the final image. High contrast also facilitates the positioning of a rule with equal precision (i.e. at the "center" or "edge" of a fringe) at each measurement. Provided these precautions are taken, accuracy in measurement of fringe spacing will then increase as magnification increases. For example, a rule scaled to 0.5mm is capable of distinguishing 0.5 Å on a print reproduced at a total magnification of 10 million times (i.e. a 20x enlargement of a 500 kX negative). If the print is further processed to a total magnification of 20 million times (viz. by re-photographing and enlarging 2x), the same rule is accurate to 0.25 Å. Because each fringe image width is also increased during magnification, difficulties in positioning the rule are alleviated (image quality assumed constant).

The error involved in measuring the position of any single fringe obviously decreases when averaged over a single measurement of many fringes. If very localized changes in composition are being monitored then a greater number of smaller groupings can be used, e.g. 10 fringes per measurement, advancing 1 fringe each time.

Even under the most carefully controlled conditions, the process of enlargement can introduce considerable error when external magnification standards (e.g. the (200) fringes of Au) are employed during analysis of unknown d-spacings. Sandwiching negatives during enlargement may furthermore complicate differentiation of standard and unknown fringes and extreme care must be taken under these circumstances.

(2.) Microdensitometer Traces

The use of a microdensitometer is indicated when higher magnifications are desired or comparisons between negatives are to be made. This instrument is capable of one-step magnification ratios greater than 1000 : 1 directly from the negative and is found to yield highly reproducible measurements. A source of difficulty however is the accurate location of "peak" positions on the trace, judged to be more difficult in most cases than determining the "center" of a fringe on an equal quality enlargement. This problem may be lessened however by increasing magnification and altering optical wedge densities. Once the peaks have been located, the same measurement errors as in (1) above apply.

(3.) Optical Diffraction

Figure 48 illustrates schematically the justification for employing an optical diffraction technique. In the electron microscope, the specimen is related by a Fourier transform to the electron diffraction pattern and by an inverse transform, the lattice image is generated. Under the action of one further transform, the electron optical image is related to the optical diffraction pattern. It therefore follows that if the lattice iamge truly represents the specimen, then the optical diffraction pattern should duplicate the electron diffraction pattern to the same order reflections used in image formation.

A primary advantage of optical diffraction is its sensitivity to periodicities which may escape detection by either of the above ((1) or (2)) techniques. Recognition of this fact prompted an early use of optical diffraction from simulated atomic arrangements to aid in the interpretation of x-ray results.[172,173] Likewise the technique

can reveal composition effects in lattice images which may aid in the interpretation of electron diffraction results.

Accuracy in measuring the spacing of diffracted intensities increases as the spots become more sharply defined, primarily because the maximum signal may not always be located at the center of a diffuse intensity region. Definition of spots may then be enhanced by using optical diffraction apertures which are sufficiently large to incorporate an increased number of fringes.

However another significant advantage of the technique is its microdiffraction capabilities, since the aberrations usually restricting selected area electron diffraction are not a factor in the optical case.[166] Hence by sacrificing some accuracy, enhanced diffraction resolution can be obtained. A lower limit on aperture size is established by interference from the small angle diffraction effects of a reduced aperture; however some resolution may be regained in this case by suitable apodization.[54]

C. Example--Spinodally Decomposed Au-Ni

The relative merits of each of these techniques for chemical analysis was judged by application to a particularly challenging example, a spinodal alloy with a sinusoidal composition variation. The Au-Ni system was chosen for study due to its large difference ($\Delta a \approx 14\%$) in component lattice parameters.[174] Sheet specimens of a Au-50 wt % Ni (77 at % Ni) alloy were homogenized at 900°C followed by an iced brine quench in order to trap a high vacancy concentration and allow sufficient atomic diffusion at low temperature. Aging at 150°C is known to give rise to satellite reflections in diffraction patterns[175] and was consequently chosen for this research. Thin foils were prepared by jet-electropolishing in a heated cyanide electrolyte.

The micrograph shown in Fig. 49 was taken from a specimen aged for 21 hrs. at 150°C. It displays both the fine lattice fringe periodicity of the (200) planes and the coarse variation in image contrast which is typical of a modulated microstructure imaged under two-beam conditions. Direct measurement of the coarse background contrast yields an average composition wavelength (λ) of 31 ± 5 Å.

A plot of lattice fringe spacing against distance normal to a reference fringe is presented in Fig. 50(a). Each point represents a single peak-to-peak distance from a microdensitometer trace scaled according to a Au lattice image standard. Although a periodicity in d-spacing is suggested by this analysis, quantitative evaluation is limited by the wide scatter in data points.

By comparison the smoothed plot in Fig. 50(b) affords direct evidence of a periodic variation in fringe spacing. Each point n ($n = 1,2,3...$) on this plot represents the average of raw data points n to $(n + 4)$, with the error bars indicating the standard deviation introduced by the averaging process. The periodicity of the modulation from an extended analysis of this type, averaged over 12 wavelengths, is 29 ± 8 Å.

Satellites are clearly visible about the (400) spot in the electron diffraction pattern (Fig. 51(a)) which records the tilted illumination imaging condition used to form this lattice image. The corresponding optical diffraction pattern (Fig. 51(b)) identically reproduces all essential diffraction effects, viz. the intense high angle and weak low angle satellites symmetrically positioned along <100> reciprocal lattice directions about <h00> fundamental lattice reflections. The difference in satellite intensities is due to the

asymmetrical (Ni-rich) alloy composition. Complementary analysis of satellite spacings reveals that both diffraction patterns are also in excellent quantitative agreement. As determined from the electron diffraction patterns, $\lambda = 29 \pm 3$ Å, while from the optical diffraction patterns, $\lambda = 29 \pm 2$ Å.

Optical microdiffracion was also performed on this specimen using an aperture diameter less than the wavelength. Fig. 52(a) depicts the result for an aperture equivalent to ~20 Å diameter at the specimen plane. By moving the aperture in ~10 Å increments, an obvious variation in diffraction spot spacing is produced (cf. Fig. 52(b)). In this case not only is the local wavelength rapidly recorded, but the amplitude of the composition modulation is captured as well. It is emphasized that the microdiffraction capabilities demonstrated by this example represent an improvement by three orders of magnitude[166] over that attainable in conventional transmission electron microscopy.

D. Summary

The results of this evaluation are presented in Table I for compositional analysis on ~2 Å lattice fringes. Image magnifications typical of high quality primary (10^7X) and secondary (2×10^7X) enlargements are included to emphasize the effect of magnification in direct image measurement accuracy.

It is concluded that the best method for precise analysis of uniformly-spaced fringes is direct print measurement using an internal standard of magnification. When comparisons with an external standard are necessary, microdensitometer analysis is suggested due to the difficulties involved in retaining comparative scales during multi-step photographic enlargement. Both of these techniques however still require

high quality negatives. If it is desired to extract information from low visibility lattice images, optical diffraction is the only feasible method for acceptable accuracy. Finally optical microdiffraction has shown a distinct advantage in localized fringe analysis and is recommended for applications where comparisons with selected area electron diffraction patterns are contemplated.

REFERENCES

1. E. O. Hall, Proc. Roy. Soc. (London) B64, 747 (1951).

2. N. J. Petch, J. Iron Steel Inst. 174, 25 (1953).

3. R. C. Gifkins, in Fracture, B. C. Averbach (ed.), Interscience, N. Y., 1959, p. 579.

4. G. Greenwood, in Interfaces, R. C. Gifkins (ed.), Butterworths, London, 1969, p. 223.

5. B. C. Woodfine, J. Iron Steel Inst. 173, 229 (1953).

6. J. R. Low, Jr., Trans. A.I.M.E. 245, 2481 (1969).

7. J. W. Cahn, Act Met. 4, 449 (1956).

8. E. Hornbogen, Met. Trans. 3, 2717 (1972).

9. M. Hillert, Met. Trans. 3, 2729 (1972).

10. R. A. Fournelle and J. B. Clark, Met. Trans. 3, 2757 (1972).

11. J. D. Livingston and J. W. Cahn, Acta Met. 22, 495 (1974).

12. R. Gronsky and G. Thomas, Acta Met. 23, 1163 (1975).

13. B. E. Sundquist, Met. Trans. 4, 1919 (1973).

14. M. Hillert, Met. Trans. 6A, 5 (1975).

15. R. Watanabe and S. Koda, Trans. Nat. Res. Inst. Metals, Japan 7, 86 (1956).

16. G. R. Speich, Trans. A.I.M.E. 242, 1359 (1968).

17. J. G. Allpress and J. V. Sanders, J. Appl. Cryst. 6, 165 (1973).

18. V. A. Phillips, Modern Metallographic Techniques and Their Application, J. Wiley & Sons, New York, 1971.

19. E. P. Butler, V. Ramaswamy and P. R. Swann, Acta Met. 21, 517 (1973).

20. H. Gleiter, Phys. Stat. Sol. (b) 45, 9 (1971).

21. R. King and B. Chalmers, Prog. Metal Phys. 1, 127 (1949).

22. D. McLean, Grain Boundaries in Metals, Oxford University Press, London, 1957.

23. S. Amelinckx and W. Dekeyser, Sol. St. Phys. 8, 325 (1959).

24. P. Chaudhari and J. W. Matthews (eds.), Grain Boundaries and Interfaces, North-Holland Publishing Company, Amsterdam, 1972.

25. L. E. Murr, Interfacial Phenomena in Metals and Alloys, Addison-Wesley Publishing Co., Massachusetts (1975).

26. W. Bollmann, Crystal Defects and Crystalline Interfaces, Springer-Verlag New York, 1970.

27. G. A. Chadwick and D. A. Smith (eds.), Grain Boundary Structure and Properties, Academic Press, London (1976).

28. D. G. Brandon, B. Ralph, S. Ranganathan and M. S. Wald, Acta Met. 12, 813 (1964).

29. M. B. Kronberg and F. H. Wilson, Trans. A.I.M.E. 185, 501 (1949).

30. S. Ranganathan, Acta Cryst. 21, 197 (1966).

31. P. H. Pumphrey and K. M. Bowkett, Scripta Met. 5, 365 (1971).

32. D. G. Brandon, Acta Met. 14, 1479 (1966).

33. G. H. Bishop and B. Chalmers, Scripta Met. 2, 133 (1968).

34. M. J. Weins, B. Chalmers, H. Gleiter and M. Ashby, Scripta Met. 3, 601 (1969).

35. M. J. Weins, H. Gleiter and B. Chalmers, J. Appl. Phys. 42, 2639 (1971).

36. R. C. Pond and D. A. Smith, in Proc. of the Sixth International Congress on Electron Microscopy, Jerusalem, 1976, p. 233.

37. P. H. Pumphrey, Scripta Met. 6, 107 (1972).

38. P. H. Pumphrey, Scripta Met. 7, 893 (1973).

39. D. H. Warrington and H. Grimmer, Phil. Mag. 30, 461 (1974).

40. B. Loberg and H. Norden, Acta Met. 21, 213 (1973).

41. J. Levy, Phys. Stat. Sol. 31, 193 (1969).

42. T. Schober and R. W. Balluffi, Phil. Mag. 21, 109 (1970).

43. T. Schober and R. W. Balluffi, Phys. Stat. Sol (b) 44, 115 (1971).

44. R. W. Balluffi, Y. Komen and T. Schober, Surf. Sci. 31, 68 (1972).

45. P. B. Hirsch, A. Howie, R. B. Nicholson, D. W. Pashley and M. J. Whelan, Electron Microscopy of Thin Crystals, Butterworths, London, 1965.

46. K. J. Hanszen, in Advances in Optical and Electron Microscopy, Vol. 4, R. Barer and V. E. Cosslett (eds.), Academic Press, New York, 1971, p. 1.

47. D. L. Misell, J. Phys. A6, 62 (1973).

48. Idem, 205.

49. D. L. Misell and A. J. Atkins, J. Phys. A6, 218 (1973).

50. J. M. Cowley, Acta Cryst. 12, 367 (1959).

51. J. M. Cowley, Diffraction Physics, North-Holland Publishing Co., Amsterdam, 1975.

52. R. D. Heidenreich, Fundamentals of Transmission Electron Microscopy, Interscience, N. Y. 1964.

53. J. W. Goodman, Introduction to Fourier Optics, McGraw-Hill, N. Y., 1968.

54. G. R. Fowles, Introduction to Modern Optics, Holt, Rinehart and Winston, Inc., New York, 1975.

55. O. Scherzer, J. Appl. Phys 20, 20 (1949).

56. W. C. T. Dowell, in Proc. of the Fifth International Congress for Electron Microscopy, Vol. I, S. S. Breese (ed.), Academic Press, New York, 1962, p. KK-12.

57. W. C. T. Dowell, J. Phys. Soc. Japan 17, B-II, 175 (1962).

58. W. C. T. Dowell, Optik 20, 535 (1963).

59. A. Bourret, J. Desseaux and A. Renault, Acta Cryst. A31, 746 (1975).

60. H. C. Sorby, J. Iron Steel Inst. 1, 255 (1887).

61. R. Dehoff and F. Rhines, Quantitative Microscopy, McGraw-Hill, N. Y. (1968).

62. F. L. Vogel, Acta Met. 3, 245 (1955).

63. S. R. Rouze and W. L. Grube, Proc. of the Int. Microscopy Symposium, Vol. 5, Academic Press, N. Y. (1960).

64. J. Nutting and S. R. Rouze, in Proc. of the Fifth Int. Cong. for Electron Microscopy, Academic Press, N. Y., 1962, Vol. 2, CC-7.

65. W. L. Grube and S. R. Rouze, Can. Met. Quart. 2, 31 (1965).

66. D. B. Holt, M. D. Muir, P. R. Grant and I. M. Boswarva, Quantitative Scanning Electron Microscopy, Academic Press, London (1974).

67. M. J. Attardo and J. M. Galligar, Acta Met. 15, 395 (1967).

68. D. A. Smith and M. J. Coringe, Phil. Mag. 25, 1505 (1972).

69. P. L. Bolin, R. J. Bayuzick and B. N. Ranganathan, J. Micros. 102, 355 (1974).

70. P. L. Bolin, R. J. Bayuzick and B. N. Ranganathan, Phil. Mag. 32, 891 (1975).

71. Idem, 895.

72. S. L. Sass, T. Y. Tan and R. W. Balluffi, Phil. Mag. 31, 559 (1975).

73. K. N. Tu, Scripta Met. 4, 959 (1970).

74. D. Y. Guan, B. W. Batterman and S. L. Sass, Phil. Mag. 33,199 (1976).

75. D. Y. Guan and S. L. Sass, Phil. Mag. 27, 1225 (1973).

76. S. L. Sass, in Proc. of the Sixth European Congress on Electron Microscopy, Jerusalem, 1976, p. 221.

77. G. Thomas, Trans. A.I.M.E. 233, 1608 (1965).

78. S. Amelinckx, R. Gevers, G. Remaut and J. Van Landuyt (eds.), Modern Diffraction and Imaging Techniques in Material Science, North Holland Publishing Co., Amsterdam, 1970.

79. P. C. Hancock and G. W. Lorimer, in Proc. of the Seventh International Congress on Electron Microscopy, Vol. II, Grenoble, 1970, p. 187.

80. P. H. Pumphrey and K. M. Bowkett, in Proc. of the Seventh International Congress on Electron Microscopy, Vol. II, Grenoble, 1970, p. 189.

81. C. T. Young, J. H. Steele, Jr., and J. L. Lytton, Met. Trans. 4 2081 (1973).

82. D. A. Smith, J. de Phys. 36, C4-1 (1975).

83. J. P. Hirth and R. W. Balluffi, Acta Met. 21, 929 (1973).

84. H. Gleiter, in Proc. of the Sixth International Congress on Electron Microscopy, Jerusalem, 1976, p. 218.

85. L. E. Murr, in Proc. of the Eighth International Congress on Electron Microscopy, Vol I, Canberra, 1974, p. 604.

86. L. E. Murr, Met. Trans. 6A, 505 (1975).

87. L. E. Murr, in Physical Aspects of Electron Microscopy and Microbeam Analysis, B. M. Siegel and D. R. Beaman (eds.), J. Wiley & Sons, 1975, p. 163.

88. M. J. Marcinkowski, in Electron Microscopy and Structure of Materials, G. Thomas, R. M. Fulrath and R. M. Fisher (eds.), Univ. of California Press, Berkeley, 1972, p. 382.

89. R. C. McDonald and A. J. Ardell, Phys. Stat. Sol.(a) 18, 407 (1973).

90. M. J. Marcinkowski, W. F. Tseng and E. S. Dwarakadasa, Phys. Stat. Sol. (a) 22, 659 (1974).

91. P. Humble and C. T. Forwood, Phil. Mag. 31, 1011 (1975).

92. Idem, 1025.

93. A. R. Thölén, in Proc. of the Eighth International Congress on Electron Microscopy, Vol I, Canberra, 1974, p. 606.

94. R. W. Balluffi, P. J. Goodhew, T. Y. Tan and W. R. Wagner, J. de Phys. 36, C4-17 (1975).

95. A. R. Jones, P. R. Howell and B. Ralph, Phys. Stat. Sol. (a) 33, 107 (1976).

96. H. Gleiter, Acta Met. 17, 565 (1969).

97. R. C. Pond, J. de Phys. 36, C4-315 (1975).

98. S. Toney and H. I. Aaronson, Trans. AIME 221, 909 (1961).

99. D. Turnbull and R. E. Hoffman, Acta Met. 2, 419 (1954).

100. J. B. Clark, in High Temperature, High Resolution Metallography, AIME Conf. Proc., Vol. 38, Gordon and Breach, 1965, p. 347.

101. D. Vaughan, Acta Met. 16, 563 (1968).

102. P. N. T. Unwin and R. B. Nicholson, Acta Met. 17, 1379 (1969).

103. J. LeCoze, C. Ranson and C. Goux, C. R. Acad. Sci. Paris C271, 1120 (1970).

104. Idem, 1225.

105. J. LeCoze, M. Biscondi and C. Goux, C. R. Acad. Sci. Paris C274, 129 (1973).

106. H. G. Aaron and G. F. Bolling, Scripta Met. 6, 553 (1972).

107. P. H. Pumphrey, Scripta Met. 7, 1043 (1973).

108. D. Vaughan, Acta Met. 18, 183 (1970).

109. K. C. Russell and H. I. Aaronson, Scripta Met. 10, 463 (1976).

110. C. J. Simpson, K. T. Aust and W. C. Winegard, Met. Trans. 1, 1482 (1970).

111. E. P. Butler and P. R. Swann, in Physical Aspects of Electron Microscopy and Microbeam Analysis, B. M. Siegel and D. R. Beaman (eds.), J. Wiley & Sons, Inc., N. Y. (1975).

112. H. Hashimoto, M. Mannami and T. Naiki, Phil. Trans. Roy. Soc. London A253, 459 (1961).

113. J. G. Allpress, E. A. Hewat, A. F. Moodie and J. V. Sanders, Acta Cryst. A28, 528 (1972).

114. D. F. Lynch and M. A. O'Keefe, Acta Cryst. A28, 536 (1972).

115. G. R. Antis, D. F. Lynch, A. F. Moodie and M. A. O'Keefe, Acta Cryst. A29, 138 (1973).

116. M. A. O'Keefe, Acta Cryst. A29, 389 (1973).

117. D. F. Lynch, A. F. Moodie and M. A. O'Keefe, Acta Cryst. A31, 300 (1975).

118. M. A. O'Keefe and J. V. Sanders, Acta Cryst. A31, 307 (1975).

119. J. M. Cowley and S. Iijima, Z. Naturforsch. 27a, 445 (1972).

120. R. Gronsky, EMSA Bul. 6, 7 (1976).

121. T. Komoda, J. Appl. Phys. Japan 5, 452 (1966).

122. J. R. Parsons and C. W. Hoelke, J. Appl. Phys. 40, 866 (1969).

123. V. A. Phillips and J. A. Hugo, Acta Met. 18, 123 (1970).

124. J. R. Parsons and C. W. Hoelke, Phil. Mag. 22, 1071 (1970).

125. D. J. H. Cockayne, J. R. Parsons and C. W. Hoelke, Phil. Mag. 24, 139 (1971).

126. V. A. Phillips and R. Wagner, J. Appl. Phys. 44, 4252 (1973).

127. V. A. Phillips, Acta Met. 20, 1143 (1972).

128. J. R. Phillips, M. Rainville and C. W. Hoelke, Phil. Mag. 21, 1105 (1970).

129. L. M. Howe and M. Rainville, Rad. Eff. 16, 203 (1972).

130. V. A. Phillips, Acta Met. 21, 219 (1973).

131. V. A. Phillips, Acta Met. 23, 751 (1975).

132. V. A. Phillips and L. E. Tanner, Acta Met. 21, 441 (1973).

133. A. L. J. Chang, S. L. Sass and W. Krakow, Acta Met. 24, 29 (1976).

134. K. Schneider, R. Sinclair and G. Thomas, in Proc. of the Eighth International Congress on Electron Microscopy, Vol. I, Canberra, 1974, p. 520.

135. R. Sinclair, K. Schneider and G. Thomas, Acta Met. 23, 873 (1975).

136. R. Sinclair and G. Thomas, J. Appl. Cryst. 8, 208 (1975).

137. J. Dutkiewicz and G. Thomas, Met. Trans. 6A, 1919 (1975).

138. R. Sinclair and J. Dutkiewicz, Acta Met. (in press).

139. T. Y. Tan, S. L. Sass and R. W. Balluffi, Phil. Mag. 31, 575 (1975).

140. D. T. Hawkins and R. Hultgren, in Metals Handbook, Vol. 8, American Society for Metals, Metals Park, Ohio, 1973, p. 265.

141. G. J. C. Carpenter and R. D. Garwood, Met. Sci. J. 1, 202 (1967).

142. L. E. Larson, Acta Met. 15, 35 (1967).

143. M. Simerska and V. Synecek, Acta Met. 15,223 (1967).

144. T. R. Anatharaman, Scripta Met. 3, 899 (1969).

145. A. V. Dobromyslov, Phys. Met. Metallogr. 33, 63 (1972).

146. K. K. Rao, H. Herman and E. Parthe, Mat. Sci. Eng. 1, 162 (1966).

147. K. N. Melton and J. W. Edington, Scripta Met. 6, 501 (1972).

148. K. B. Rundman and J. E. Hilliard, Acta Met. 15, 1025 (1967).

149. W. Truszkowski and J. Dutkiewicz, Bull. Acad. Polon. Sci. Ser. Sci. Techn. 10, 19 (1973).

150. T. L. Bartel and K. B. Rundman, Met. Trans. 6A,1887 (1975).

151. D. T. Lewandowski and K. B. Rundman, Met. Trans. 6A, 1895 (1975).

152. A. Junqua, J. Mimault and J. Delafond, Acta Met. 24, 779 (1976).

153. K. K. Rao and H. Herman, J. Inst. Metals 94, 420 (1966).

154. K. K. Rao, L. E. Katz and H. Herman, Mat. Sci. & Engr. 1, 263 (1966).

155. D. L. Douglass and T. W. Barbee, J. Mat. Sci. 4, 138 (1969).

156. U. K. Malhotra and K. B. Rundman, Met. Trans. 3, 1521 (1972).

157. V. Ramaswamy, E. P. Bulter and P. R. Swann, J. Microscopy 97, 259 (1972).

158. K. N. Melton and J. W. Edington, J. Mat. Sci. 9, 1457 (1974).

159. K. N. Melton and J. W. Edington, Acta Met. 22, 1457 (1974).

160. R. D. Jones and K. G. Thomas, Phil. Mag. 22, 427 (1970).

161. P. A. Doyle and P. S. Turner, Acta Cryst. A24, 390 (1968).

162. A. K. Head, P. Humble, L. M. Clarebrough, A. J. Morton and C. T. Forwood, Computed Electron Micrographs and Defect Identification, North-Holland Publishing Co., Amsterdam (1973).

163. J. R. Parsons, in Interatomic Potentials and Simulation of Lattice Defects, P. C. Gehlen, J. R. Beeler, Jr. and R. I. Jaffee (eds.), Plenum Press, New York, 1972, p. 463.

164. B. V. Johansen, Micron 4, 121 (1973).

165. O. L. Krivanek, Optik 43, 361 (1975).

166. R. Sinclair, R. Gronsky and G. Thomas, Acta Met. 24, 789 (1976).

167. S. G. Lipson and H. Lipson, Optical Physics, Cambridge University Press, 1969.

168. R. Gronsky, R. Sinclair and G. Thomas, 34th Ann. Proc. Electron Microscopy Soc. Amer., Miami Beach, Florida, G. W. Bailey (ed.), 1976, p. 494.

169. G. Thomas, R. Sinclair and R. Gronsky, in Proc. of the Sixth European Congress on Electron Microscopy, Jerusalem, 1976, p. 114.

170. K. W. Andrews, D. J. Dyson and S. R. Keown, Interpretation of Electron Diffraction Patterns, Plenum Press, N. Y., 1968.

171. B. Ralph, J. de Phys. 36, C4-71 (1975).

172. C. A. Taylor, R. H. Hinde and H. Lipson, Acta Cryst. 4, 261 (1951).

173. H. Lipson and C. A. Taylor, Acta Cryst. 4, 458 (1951).

174. R. Gronsky, M. Okada, R. Sinclair and G. Thomas in 33rd Ann. Proc. Elec. Mic. Soc. Amer., G. W. Bailey (ed.), Las Vegas, Nevada, 1975, p. 22.

175. J. E. Woodilla and B. L. Averbach, Acta Met. 16 225 (1968).

Table 1

Accuracy in Compositional Analysis
(Basis: 2Å Lattice Images)

METHOD	MEASUREMENT ERROR		
	1 fringe	10 fringes	100 fringes
Direct print measurement (10^7X)	±5-25%	±1-2%	±0.1%
Direct print measurement ($2x10^7$X)	±2-12%	±0.5-1%	±0.05%
Microdensitometer Traces (50:1)	±10-30%	±1-3%	±0.1%
Optical Diffraction Patterns	±∞	±0.5-2%	±0.5-2%

FIGURE CAPTIONS

Fig. 1 Optical analogue for the plane matching model of grain boundary structure. The Moiré pattern of spacing d is produced by overlapping gratings d_1 and d_2 misoriented by an angle θ. The angle between the Moiré bands and the fringes of grating (1) is ρ.

Fig. 2 Ray diagram for two-beam tilted illumination lattice imaging. The object (lattice planes of spacing d_{hkl}) appears in the image at exact focus with spacing Md_{hkl}, M = magnification.

Fig. 3 Phase diagram for the Al-Zn system. The two alloys studied during this research have compositions Al-10 at.% Zn (alloy 1) and Al-30 at.% Zn (alloy 2).

Fig. 4 Calculated variation of visibility as a function of specimen thickness for the {200} planes in alloy 1. The computations included eight systematic beams, with imaging conditions as shown in Fig. 2 above.

Fig. 5 Composite plot of the intensity profile for the {111} planes in both pure Al and an alloy of 50 at.% Zn for a crystal thickness of 300 Å, calculated as in Fig. 4 above.

Fig. 6 Low magnification illustration of a two-beam lattice image (tilted illumination) in a defocused (a) and focused (b) state. Exact focus is determined by absolute superposition of the BF (dark) and DF (light) images.

Fig. 7 (a) Lattice image of a grain boundary region in alloy 1 aged 30 mins. at 180°C, shown at low magnification. The fringes running vertically through the upper grain are spaced 2.3 Å apart.

(b) Diffraction conditions used in (a). The upper grain is near a [110] zone (outlined), while the arrowed diffraction spike originates from the lower grain.

Fig. 8 (a) Enlargement of Fig. 7(a) showing $(\bar{1}\bar{1}\bar{1})$ fringes within the matrix and fringes of a different spacing and orientation at the boundary, corresponding to a higher Zn content. The white slash marks highlight the very weak Moire pattern within the solue-rich region.

(b) Another segment of the same boundary showing that the region of solute segretation maintains a distinct fringe identity down to a thickness of ~8 to 10 Å.

Fig. 9 Conventional (a, c, and d) and weak beam (b) images of a grain boundary precipitate in alloy 1, aged 30 mins. at 180°C. The defects arrowed in (a) are matrix slip dislocations. Note the internal facets arrowed in (b) visible only in the weak beam image.

Fig. 10 Comparison of DF (a) and lattice image (b) of a grain boundary precipitate in alloy 2 aged 1 min. at 135°C. The boxed region indicates a wedge similar to that seen in Fig. 9(b) above.

Fig. 11 Enlargement of the boxed region in Fig. 10. Careful analysis reveals that the fringes within the wedge region have a spacing

1.6% larger than those within the precipitate, indicating a higher Zn content in the lower wedge.

Fig. 12 Grain boundary precipitate in alloy 1 aged 30 min. at 180°C and imaged at increasing deviation parameter. The enhanced resolution of the weak beam image in (c) reveals the presence of the arrowed facet and grain boundary defects.

Fig. 13 (a) Lattice image of a grain boundary precipitate for the same aging conditions as in Fig. 12. The simultaneous appearance of fringes in both grains as well as the precipitate permits direct verification of the plane matching description of the interfacial Moiré lines.
(b) Diffraction conditions used in (a).

Fig. 14 Enlargement of the arrowed interphase boundary segment in Fig. 13(a). The terminating fringes identified by open arrows indicate that structural relaxation is occurring within regions of high atomic density.

Fig. 15 Bright field (a) and weak beam (b) images of a grain boundary precipitate in alloy 2 aged 1 wk. at room temperature. Ledges following {111} matrix traces are seen in (a). Also arrowed in (b) are interfacial structural lines as in Fig. 13(a) above.

Fig. 16 Low magnification lattice image of a grain boundary precipitate in alloy 1 aged 30 mins. at 180°C. The boxed regions indicate two primary facets in the growth front.

Fig. 17 High magnification versions of the boxed facets in Fig. 16 above. In (a), facet 1 is shown to parallel the $(1\bar{1}1)$ matrix trace of the grain into which growth is occurring. The arrows indicate microledges one to two atom planes in thickness which maintain the macroscopic facet orientation. Facet 2 is seen in (b) to be atomically flat with the exception of one to two atom-layer microledges. Its orientation parallels the $(1\bar{1}1)$ planes of the matrix grain in which nucleation occurred.

Fig. 18 Enlargements of the precipitate shown in Fig. 16 above indicating the interfacial regions on which optical microdiffraction analysis was performed.

Fig. 19 (a) Optical diffraction pattern from region 1 in Fig. 18(a) showing the distinct periodicities of the matrix (high angle) and precipitate (low angle) spots.

(b) Optical diffraction pattern from region 2 in Fig. 18(a) showing the sensitivity of this technique to the presence of weak fringes (diffraction spot arrowed).

(c) Optical diffraction pattern from region 1 in Fig. 18(b). The arrowed inner spots correspond to twice the periodicity of the imaged precipitate reflections.

(d) Optical diffraction pattern from region 2 in Fig. 18(b).

Fig. 20 Schematic illustration of the rhombohedrally distorted reciprocal lattice (solid lines) of the Zn-rich precipitate phase with respect to the fcc Al-rich matrix (dotted line).

Fig. 21 Plot of fringe spacing in region 1 of Fig. 18(b) as a function of distance across the boundary. Each measurement included 5 fringes, the error bar for which is drawn on the first data point.

Fig. 22 Lattice image of grain boundary precipitate for same aging conditions as in Fig. 16 above: (a) low magnification and (b) enlargement of the boxed region on which compositional analysis was performed.

Fig. 23 Plot of fringe spacing vs. distance for region of Fig. 22(b) above. Each measurement included 10 fringes (error bar shown on first data point). The presence of a composition gradient in both matrix and precipitate is revealed.

Fig. 24 Enlargement of the grain boundary region in Fig. 22 shown edge-on. The precipitate at bottom displays 45 fringes between the arrowed vertical dividers while the matrix shows 48 fringes in the same distance. A single terminating fringe is indicated by the open arrow on the matrix side.

Fig. 25 Enlargement of the grain boundary region in Fig. 22 showing the accommodation of boundary mismatch over 7 or 8 lattice planes between the open arrows. The black and white arrow connects a dark fringe from the precipitate with a light fringe from the matrix through a thickness extinction contour.

Fig. 26 Enlargement of the same boundary from Fig. 22 shown in an inclined orientation. Arrows emphasize the drastic fringe bending occurring over the trasition region.

Fig. 27 (a) Low magnification of a grain boundary precipitate in alloy 2 aged 1 wk. at room temperature showing boxed area of interest for subsequent analysis.

(b) Diffraction conditions used in (a). The arrow indicates the presence of a weak spot corresponding to an (0001) Zn reflection.

Fig. 28 High magnification of the boxed region in Fig. 27 above. The $(1\bar{1}1)$ fringes of the matrix are seen in addition to the (0001) fringes of the Zn precipitate. Matrix fringes are also seen at the growth front of the precipitate. The relative positions and visibilities of each of these fringe images remained unaffected by a −320 Å to +320 Å through-focus series.

Fig. 29 Indexing scheme for superimposed [110] fcc and $[11\bar{2}0]$ hcp diffraction patterns. Parentheses indicate the position of the (0001) reflections which are made possible by double diffraction.

Fig. 30 Microdensitometer traces of the matrix (top) and precipitate (bottom) regions of Fig. 28, to the same scale, indicating the separate occurrence of these fringe spacings in their respective image regions.

Fig. 31 Microdensitometer trace (a) and optical diffraction pattern (b) of the interphase boundary region in Fig. 28. Both matrix and precipitate fringe spacings are detected.

Fig. 32 Two images of the same low angle boundary in alloy 1 aged 30 mins. at 180°C showing that the dislocations comprising the misfit net (a) serve as nucleation sites for precipitates (b) which are elongated in the direction of the dislocation lines.

Fig. 33 (a) Aligned equiaxed precipitates within a pure tilt grain boundary.

(b) Hemispherical cap morphology of grain boundary precipitates which do not appear to be influenced by the dislocation net. Specimen identical to that of Fig. 32 above.

Fig. 34 Precipitates at a high angle boundary shown to be influenced by the presence of extrinsic dislocations arrowed in (a) and (c). A dislocation is seen in the weak beam image (b) to also connect the precipitate at the upper left. All interconnected precipitates were observed to be larger in size than those not attached to a dislocation (cf. lower right).

Fig. 35 Intrinsic dislocations (small arrows) at a high angle grain boundary with only a slight misorientation of (002) matrix planes. The intrinsic network increases in density at regions of sharper boundary curvature and near the precipitate. A large arrow (a) locates an extrinsic dislocation at the face of the precipitate.

Fig. 36 Bright field images of boundaries between colonies of the R-phase discontinuous reaction product in alloy 2 aged 15 mins. at 185°C. Both denuded regions (a) and complete continuity up to the boundary (b) were observed. Subsequent precipitation within the Al-rich phase is also evident.

Fig. 37 Micrographs of a grain boundary region indicating sharp cusps (arrowed in (b)) at positions of the R-phase interlamellar boundaries. The Zn-rich lamellae are preferentially etched and appear in (a) to be continuously curved at points of termination (small arrow).

Fig. 38 Bright field (a) and weak beam (b) images of an R-phase lamellar termination indicating that misorientation is accommodated by a single lattice dislocation (arrowed).

Fig. 39 (a) High magnification DF image of an R-phase interlamellar boundary.

(b) Diffraction conditions used in lattice imaging the area of (a), shown in Fig. 40. Diffraction spot splitting is observed.

Fig. 40 Lattice image of an R-phase interlamellar boundary. Fringe terminations are evident within the boundary at the same relative positions (arrowed) with respect to the Moiré bands. A slight compression in fringe spacing is also detected near the boundary.

Fig. 41 Lattice image at vicinity of an R-phase lamellar termination. A slight misorientation (~2°) is detected by direct fringe measurement, corresponding to the extent of diffraction spot splitting seen in Fig. 39(b) above.

Fig. 42 (a) Low magnification BF image of the low temperature discontinuous reaction product in alloy 2 aged 2 wks. at room temperature.

(b) High magnification image of the periphery of a colony showing boxed region of the lattice image in Fig. 43.

Fig. 43 Lattice image of the (200) matrix planes in the low temperature discontinuous reaction product. Fringes were found to be continuous in both spacing and orientation across the reaction front through the Al-rich phase.

Fig. 44 Stereo pair of low temperature discontinuous reaction product at a grain boundary (a) and within a grain (b) showing that the reaction is not limited to the foil surfaces.

Fig. 45 Lattice image of a grain boundary precipitate showing 1.4 Å fringes from the (220) matrix planes and 2.1 Å fringes from the $(01\bar{1}2)$ precipitate planes.

Fig. 46 Comparison of the electron diffraction pattern (a) used to form the image in Fig. 45 and the optical diffraction pattern (b) taken from the lattice image negative. Four periodicities are evident in (b), the (220) matrix fringes, the $(01\bar{1}2)$ precipitate fringes, the $(1\bar{1}02)$ precipitate fringes and the spatial periodicity resulting from the interference of the $(01\bar{1}2)$ and $(1\bar{1}02)$ reflections.

Fig. 47 Comparison of the three methods employed during this research for lattice image analysis: (a) direct fringe measurement, (b) microdensitometer traces, and (c) optical diffraction, illustrated here for the (200) lattice image of an evaporated Au film.

Fig. 48 Schematic illustration of the Fourier transform (F) relationship linking the object, electron diffraction pattern, lattice image and optical diffraction pattern. The optical diffraction pattern illustrated here is an enlarged version of the first order reflections in the electron diffraction pattern. A comparison of these patterns indicates the accuracy of the lattice image in representing the object.

Fig. 49 Lattice image of a spinodally decomposed Au-77 at.% Ni alloy aged 21 hrs. at 150°C. Both the fine lattice fringe periodicity of the (200) planes and the coarse background characteristic of a modulated microstructure are observed.

Fig. 50 (a) Plot of individual fringe spacings measured from a microdensitometer trace normal to the fringes in Fig. 49. (b) Smoothed version of (a). Each point n (n = 1,2,3, ...) represents the average of raw data points n to (n + 4). The average wavelength indicated by this analysis is 29 $\pm$ 8 Å.

Fig. 51 Comparison of the electron diffraction pattern (a) used in forming Fig. 49 and the optical diffraction pattern (b) taken from the lattice image negative. Agreement in satellite (s) intensities and spacing is evident (cf. the (400) spot in (a)).

Fig. 52 Results of an optical microdiffraction analysis of Fig. 49. By moving an aperture equivalent to ~20 Å at the specimen plane in ~10 Å increments normal to the fringes, a periodic variation in diffraction spot spacing is produced (a).

Satellites are not evident in these patterns (cf. the central insert from Fig. 51(b) above) because the aperture is smaller than the composition wavelength. The extent of the difference in spot spacing is emphasized by the enlargement shown in (b).

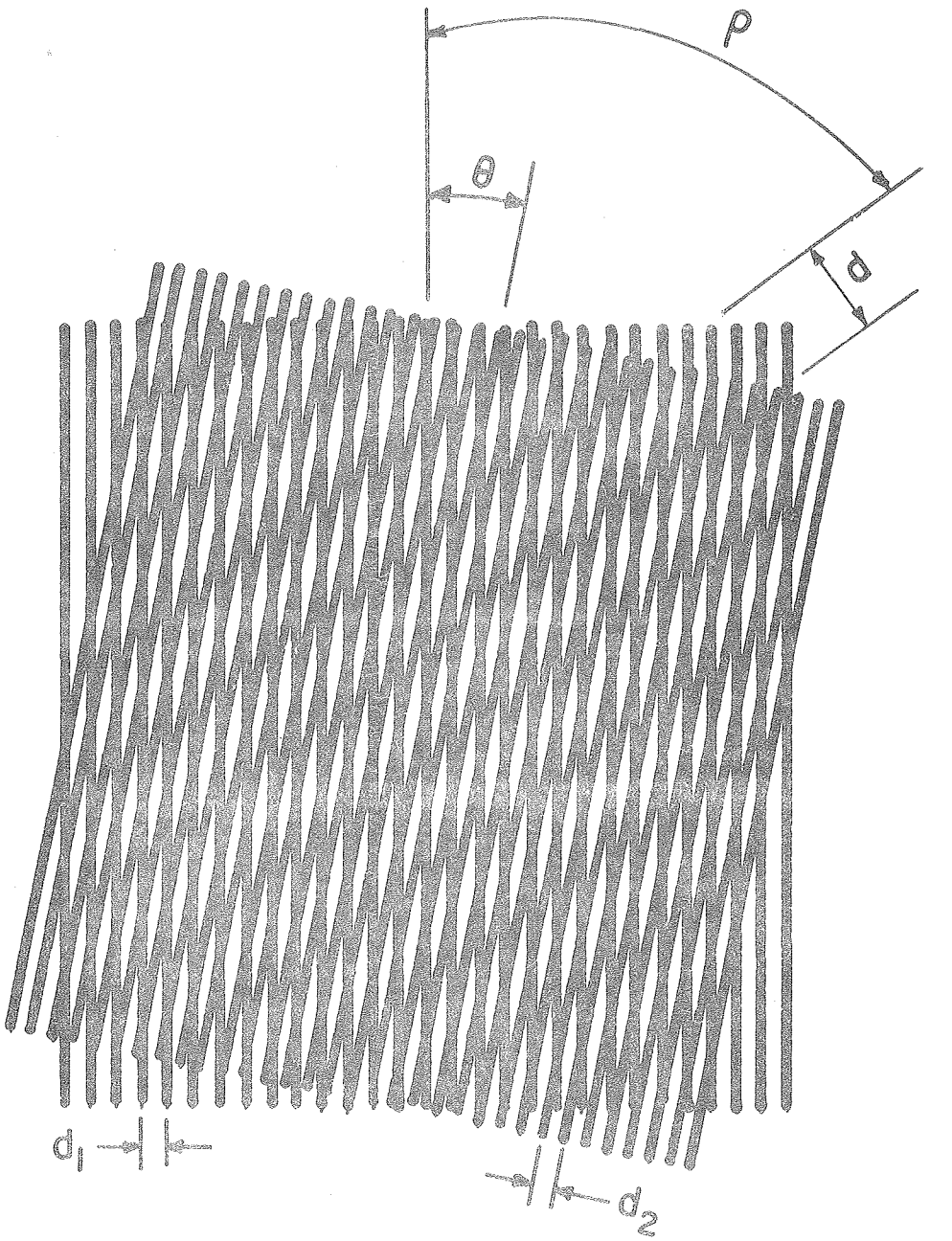

XBL 7611-7802

Fig. 1

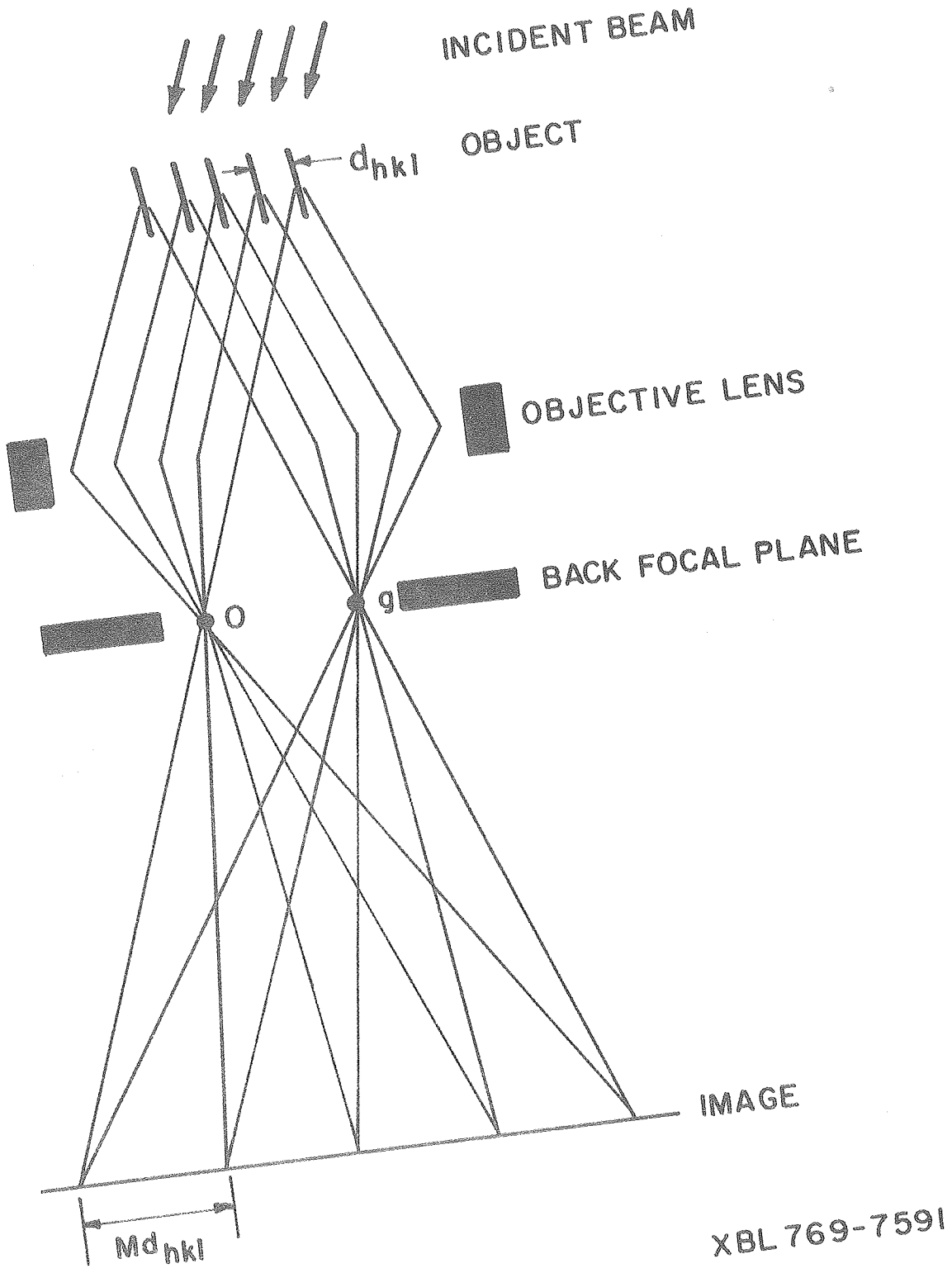
INCIDENT BEAM
d_{hkl}
OBJECT
OBJECTIVE LENS
BACK FOCAL PLANE
O
g
IMAGE
Md_{hkl}
XBL 769-7591

Fig. 2

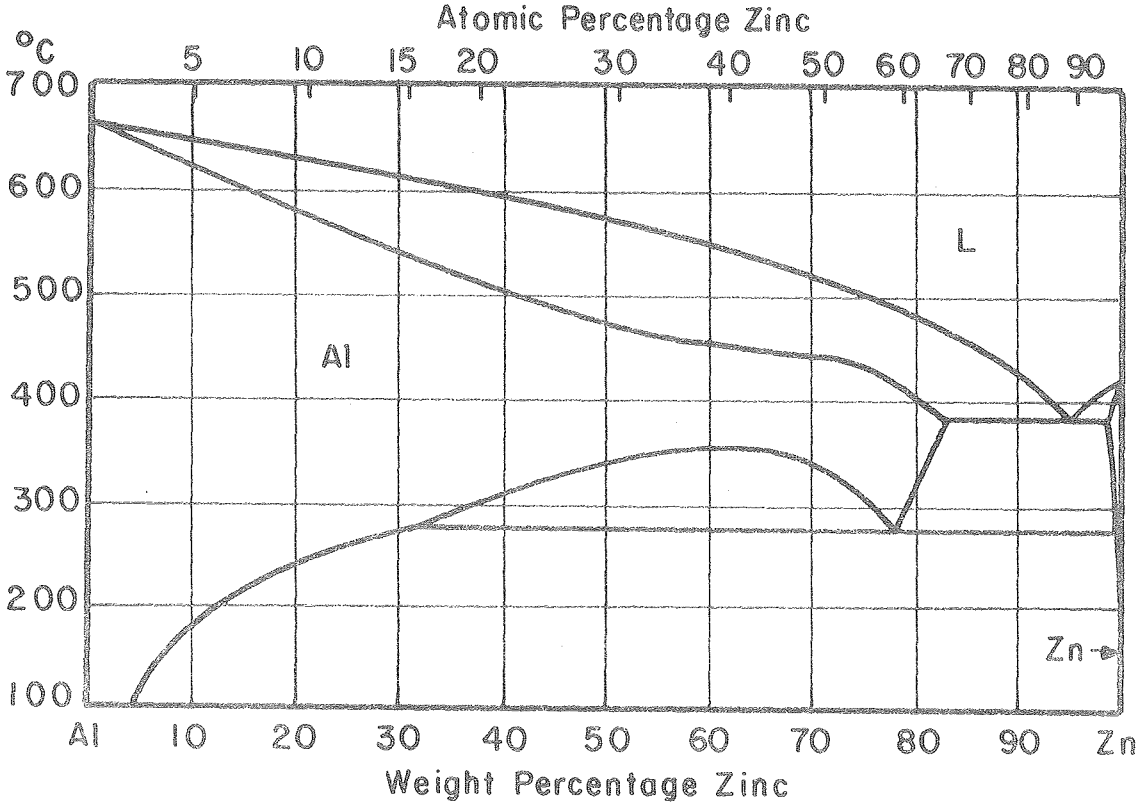

XBL 7611-7743

Fig. 3

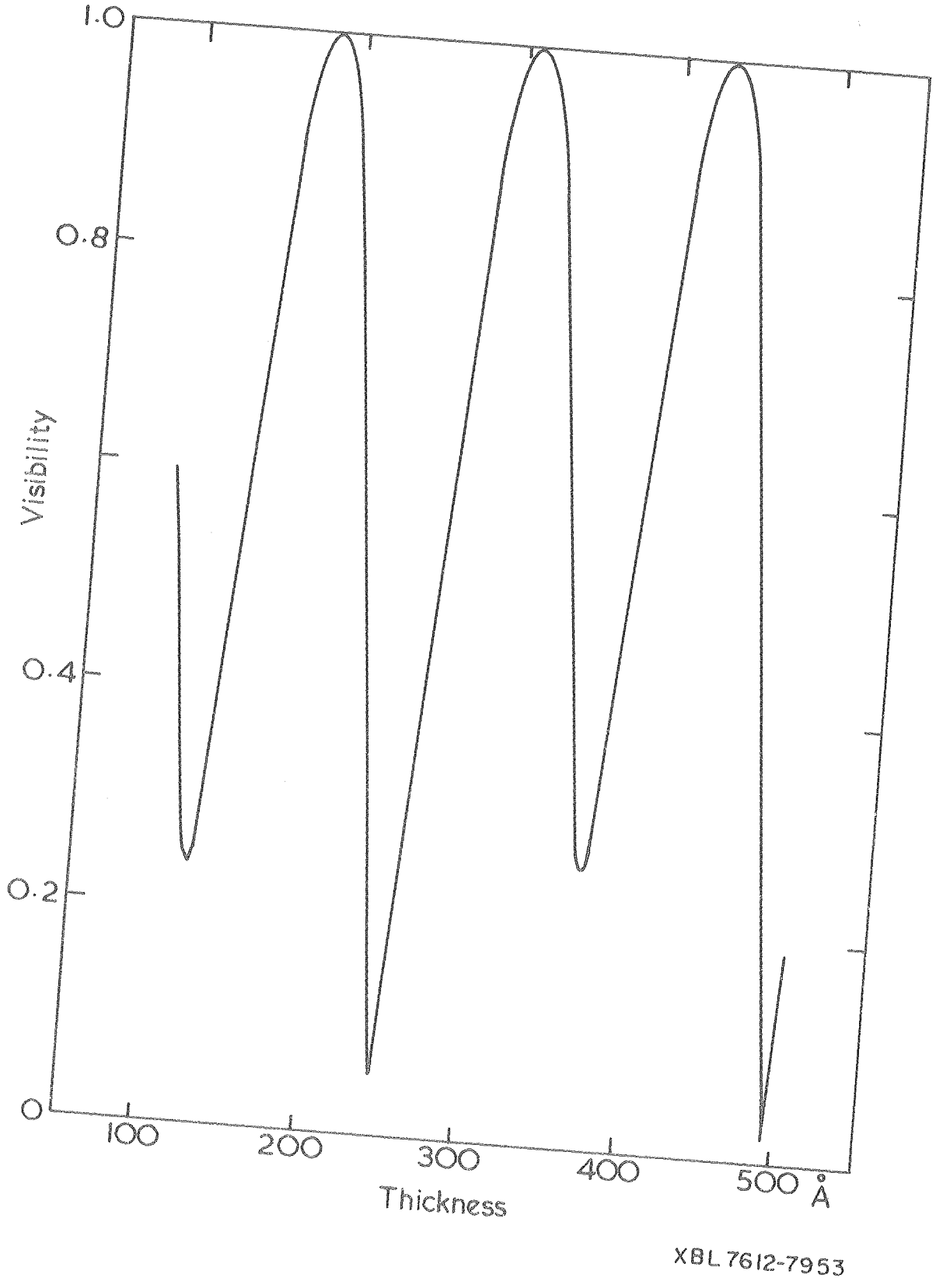
1.0
0.8
0.4
0.2
0
Visibility
100
200
300
400
500 Å
Thickness
XBL 7612-7953

Fig. 4

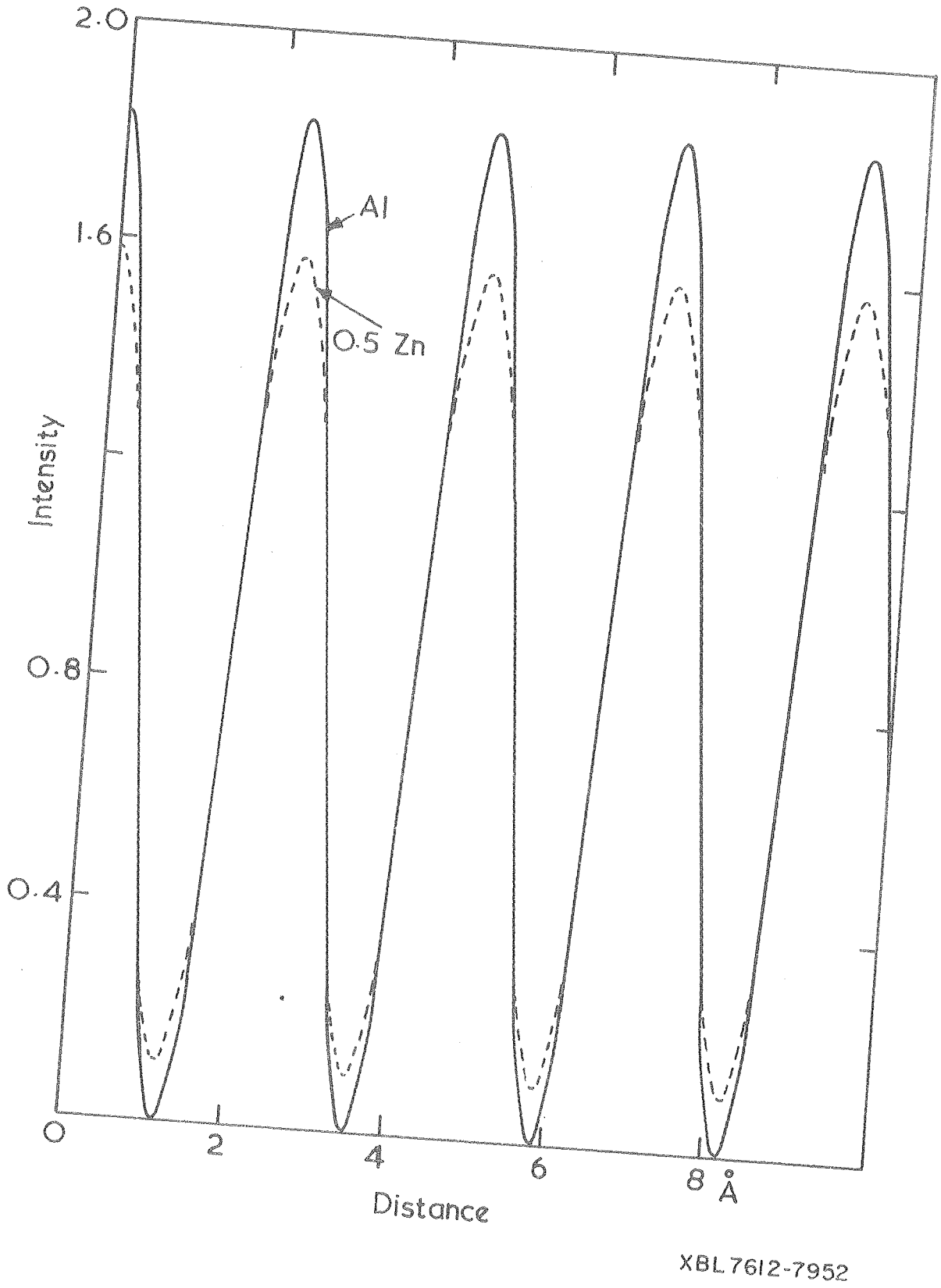

Fig. 5

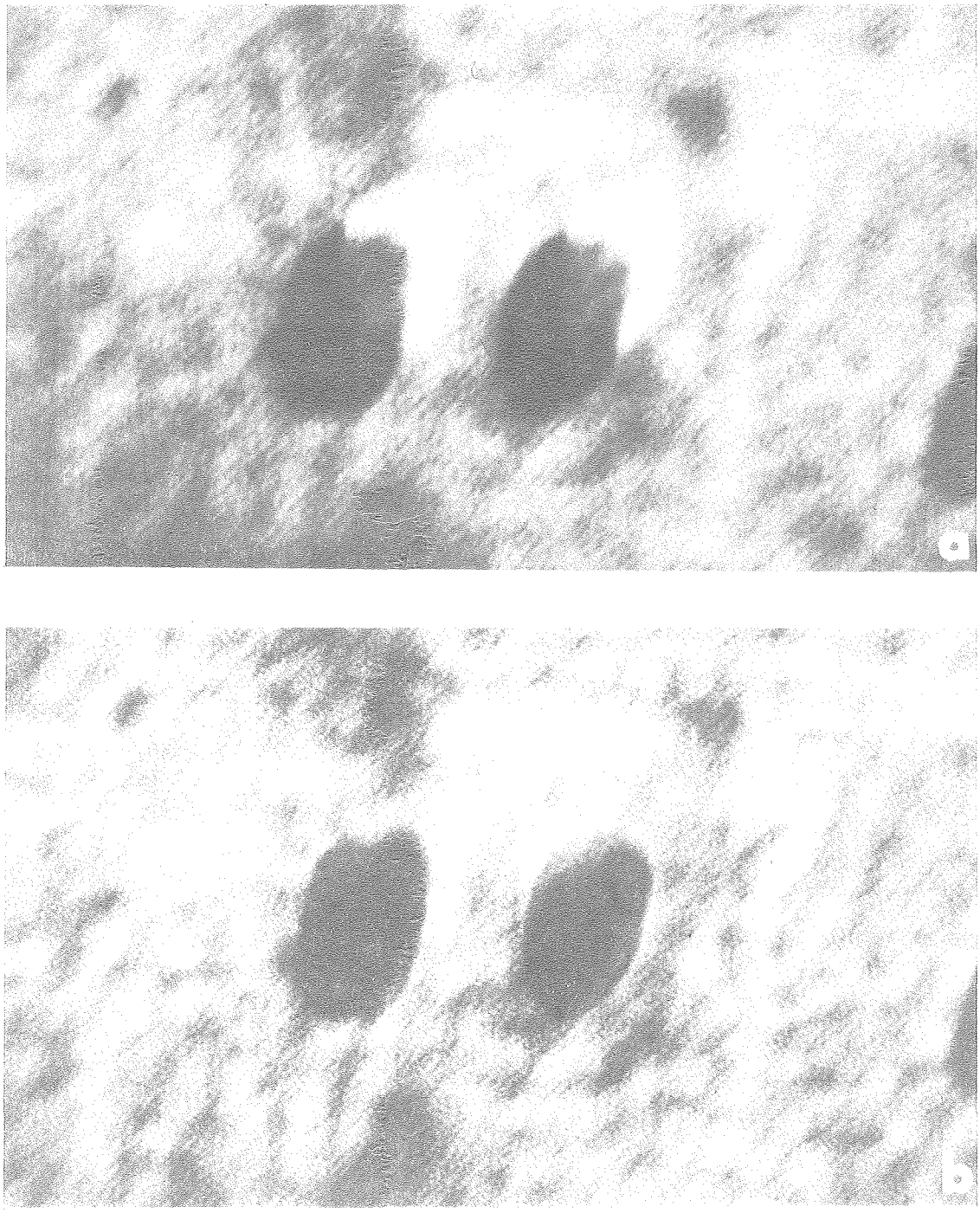

XBB 767-6525

Fig. 6

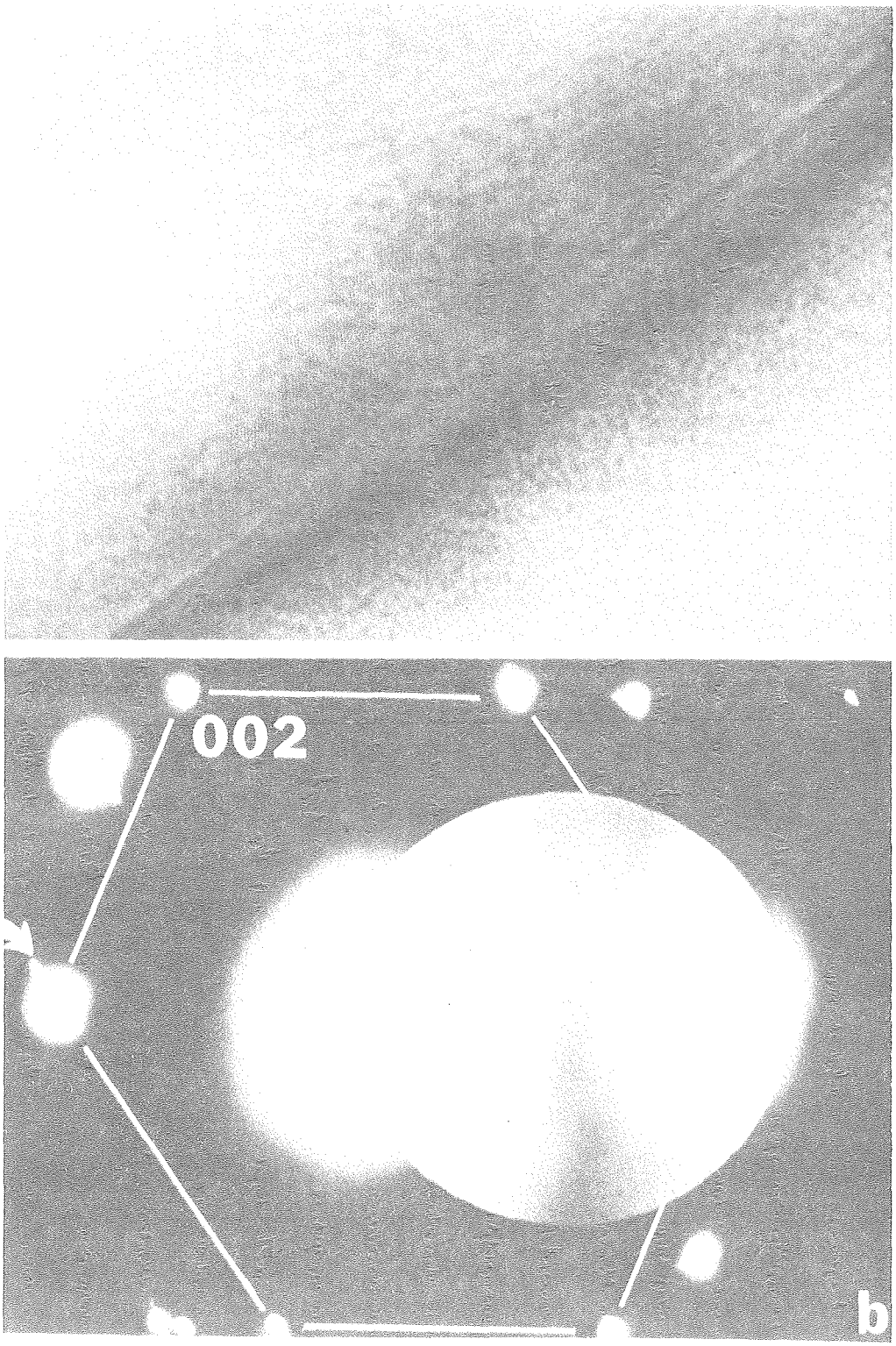

XBB 7611-10525

Fig. 7

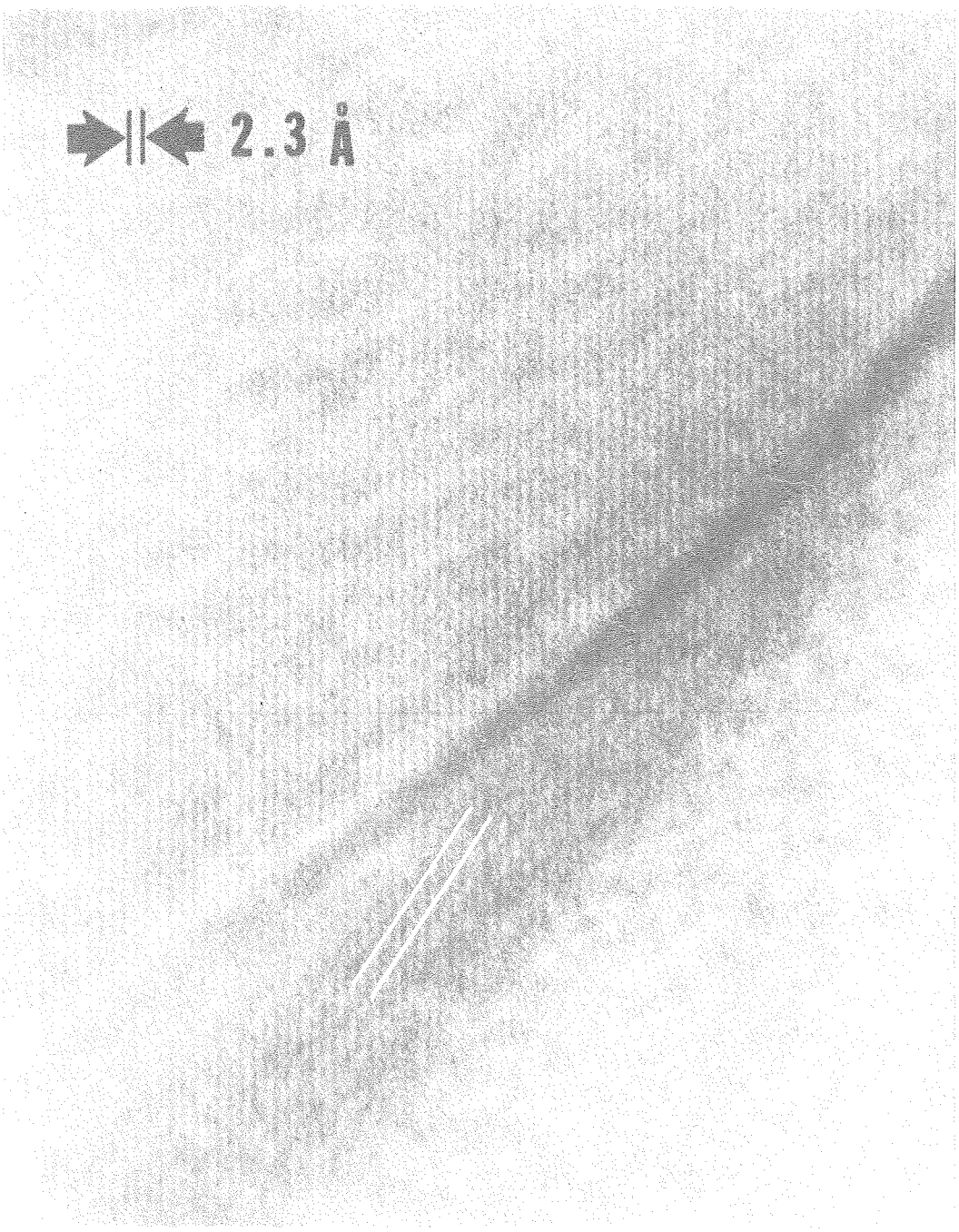

XBB 7611-10515

Fig. 8(a)

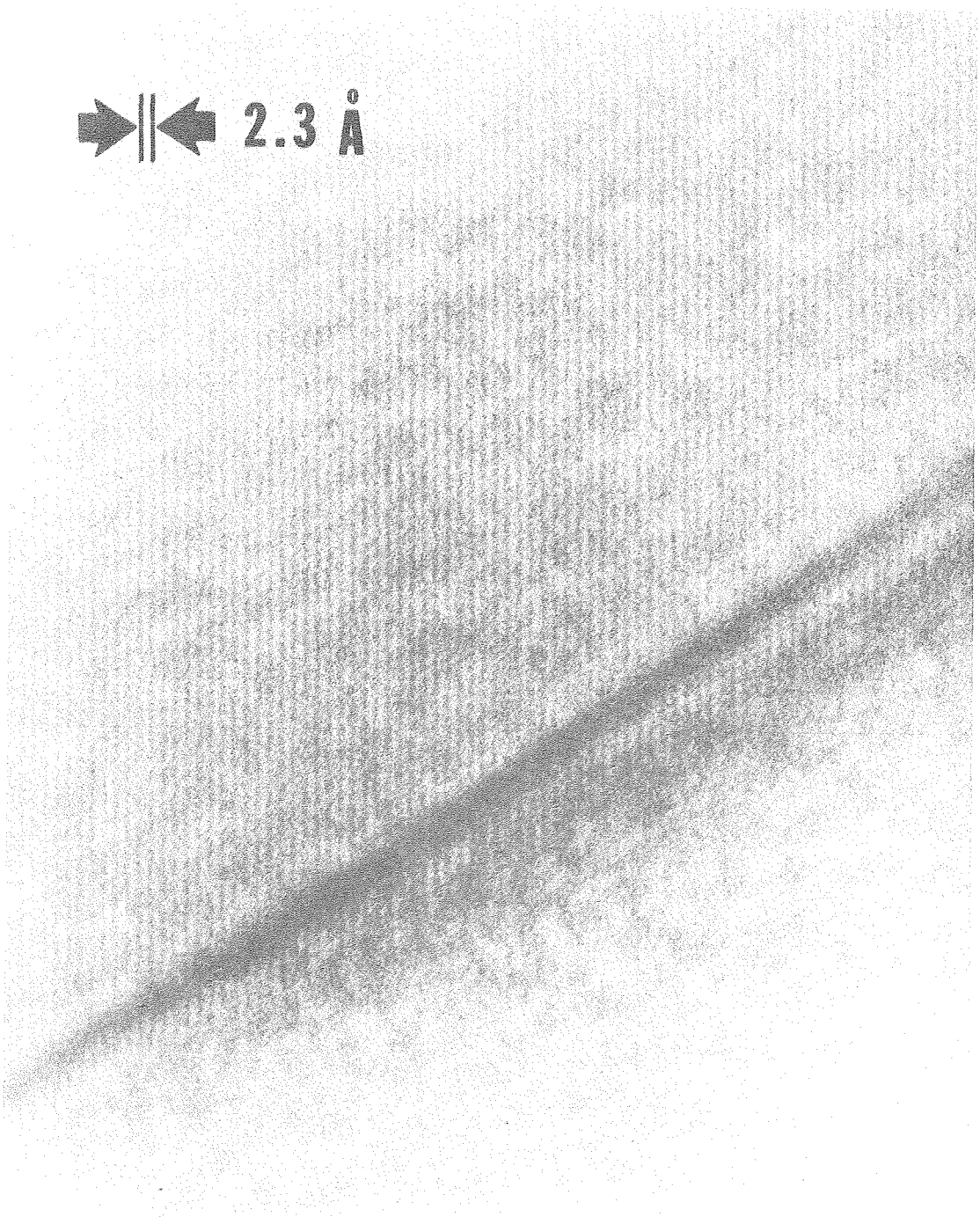

XBB 7611-10516

Fig. 3(b)

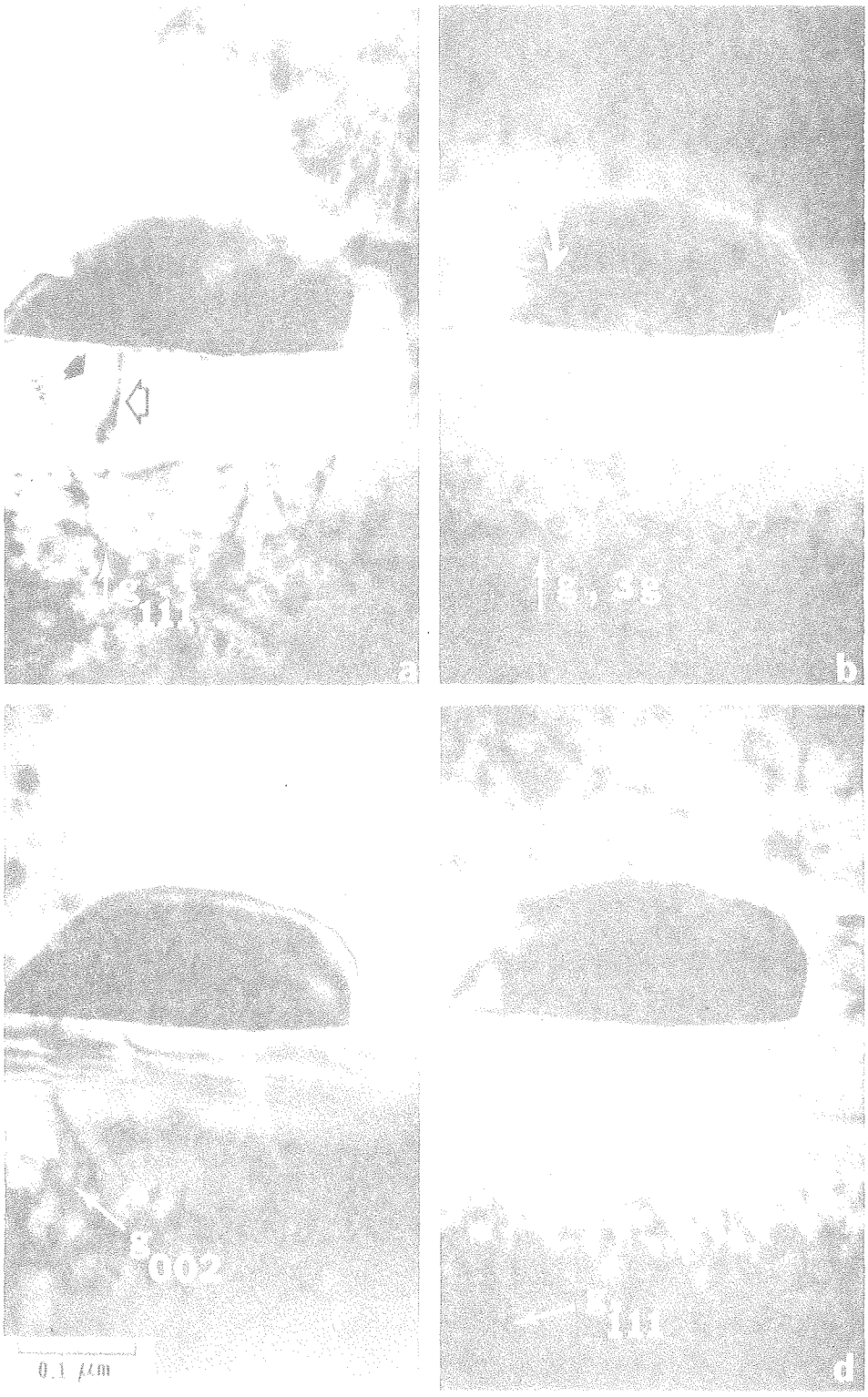

XBB 7611-10506

Fig. 9

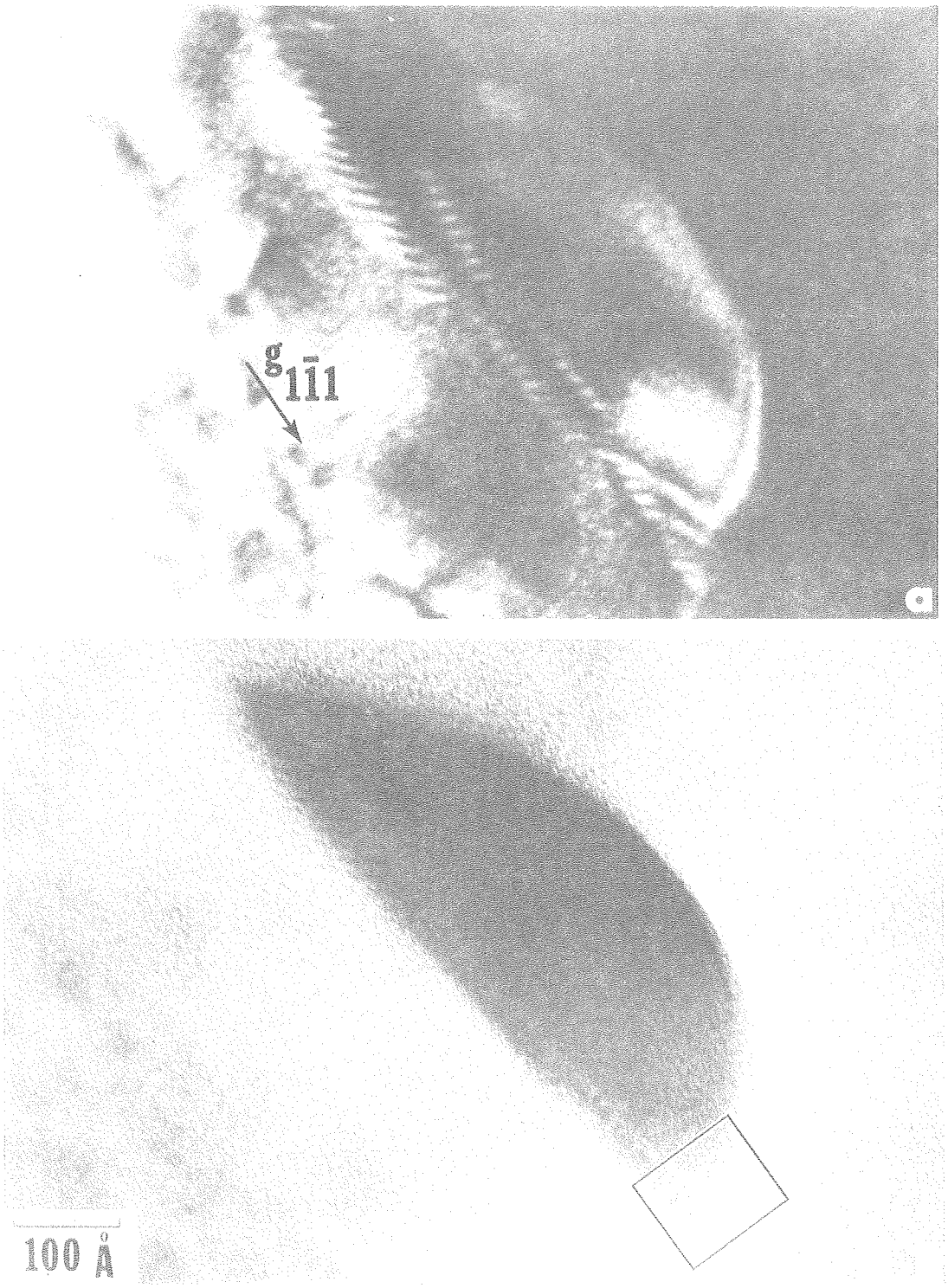

XBB 7611-10499

Fig. 10

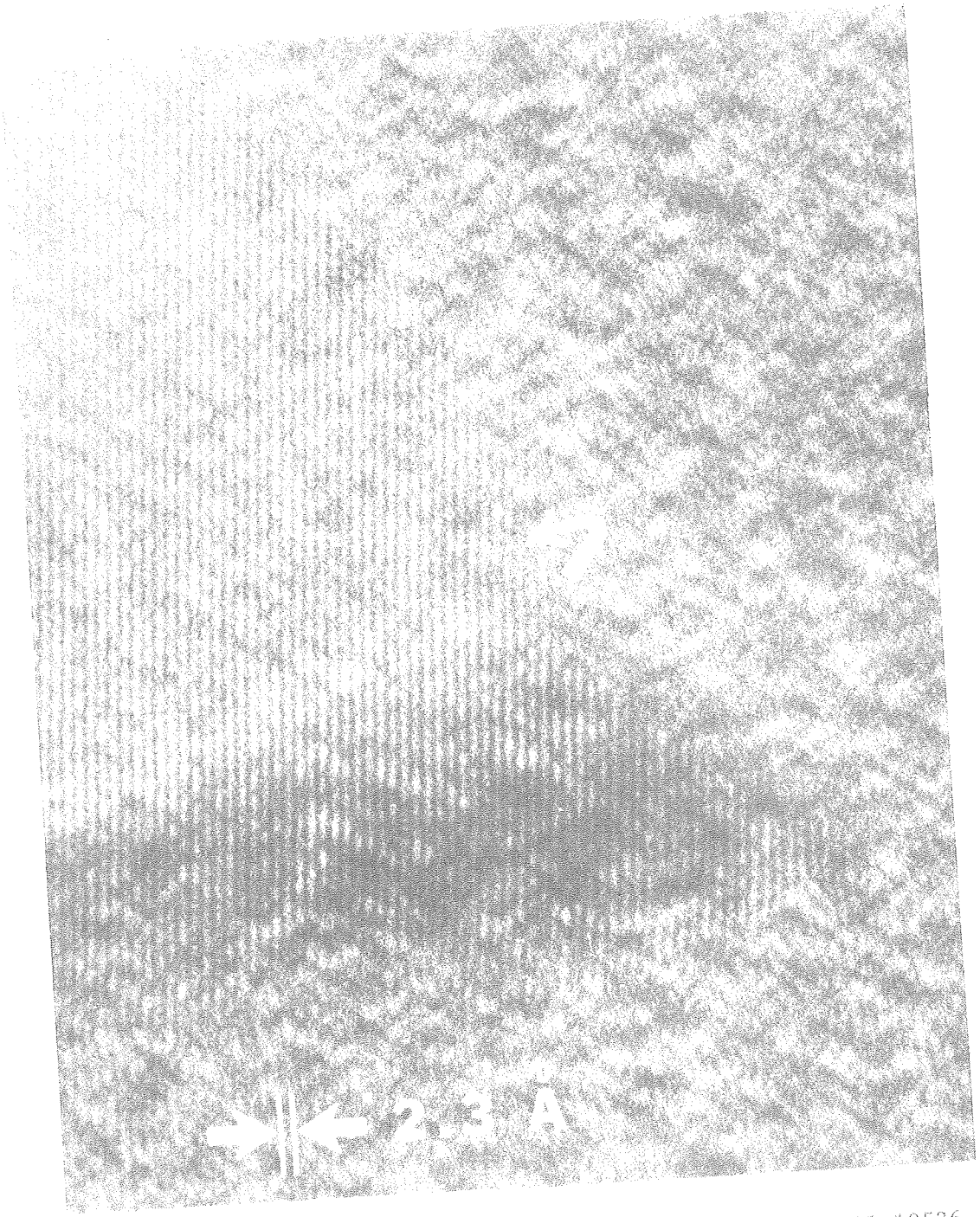

XBB 7611-10526

Fig. 11

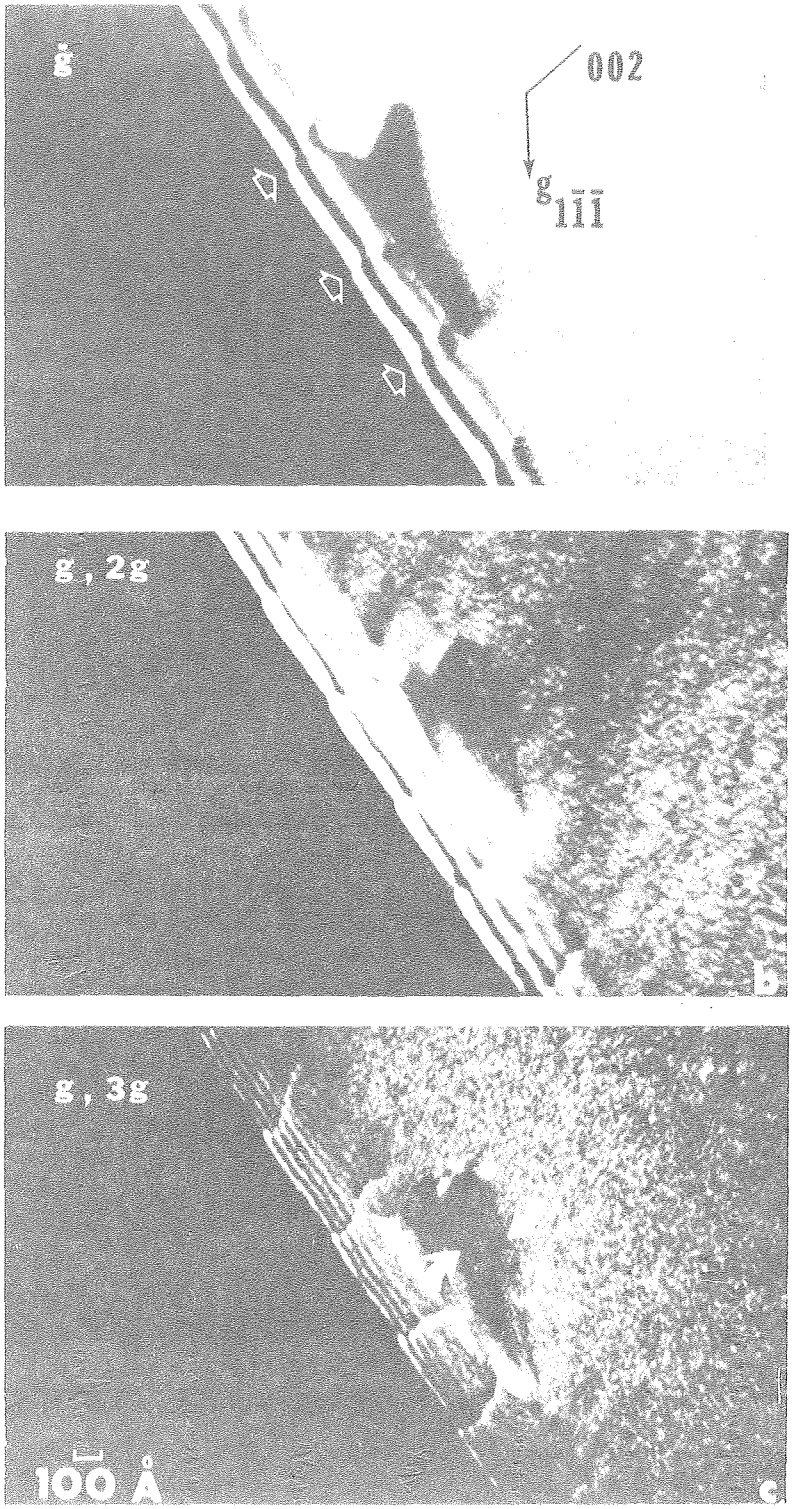

XBB 7611-10505

Fig. 12

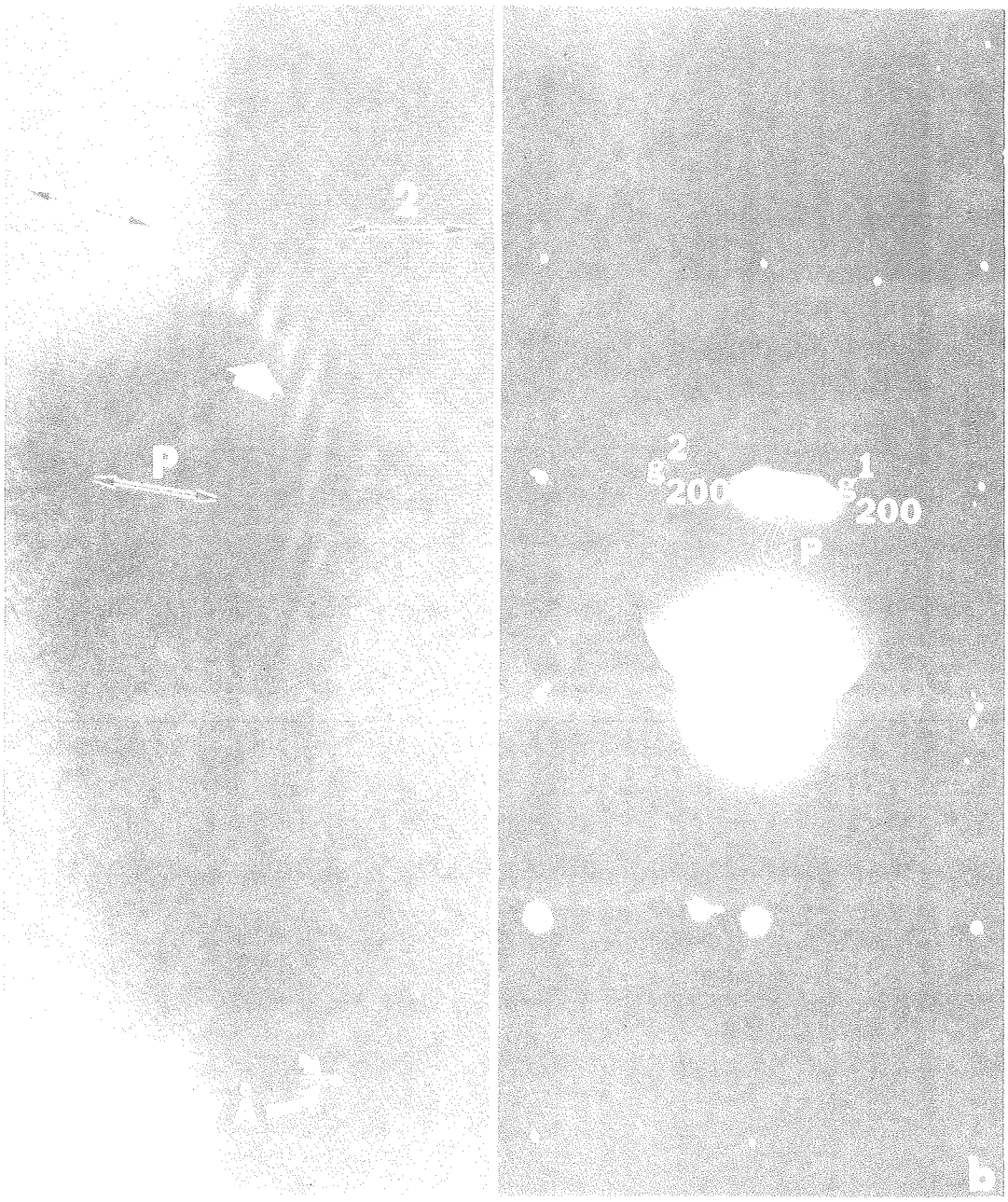

XBB 7611-10509

Fig. 13

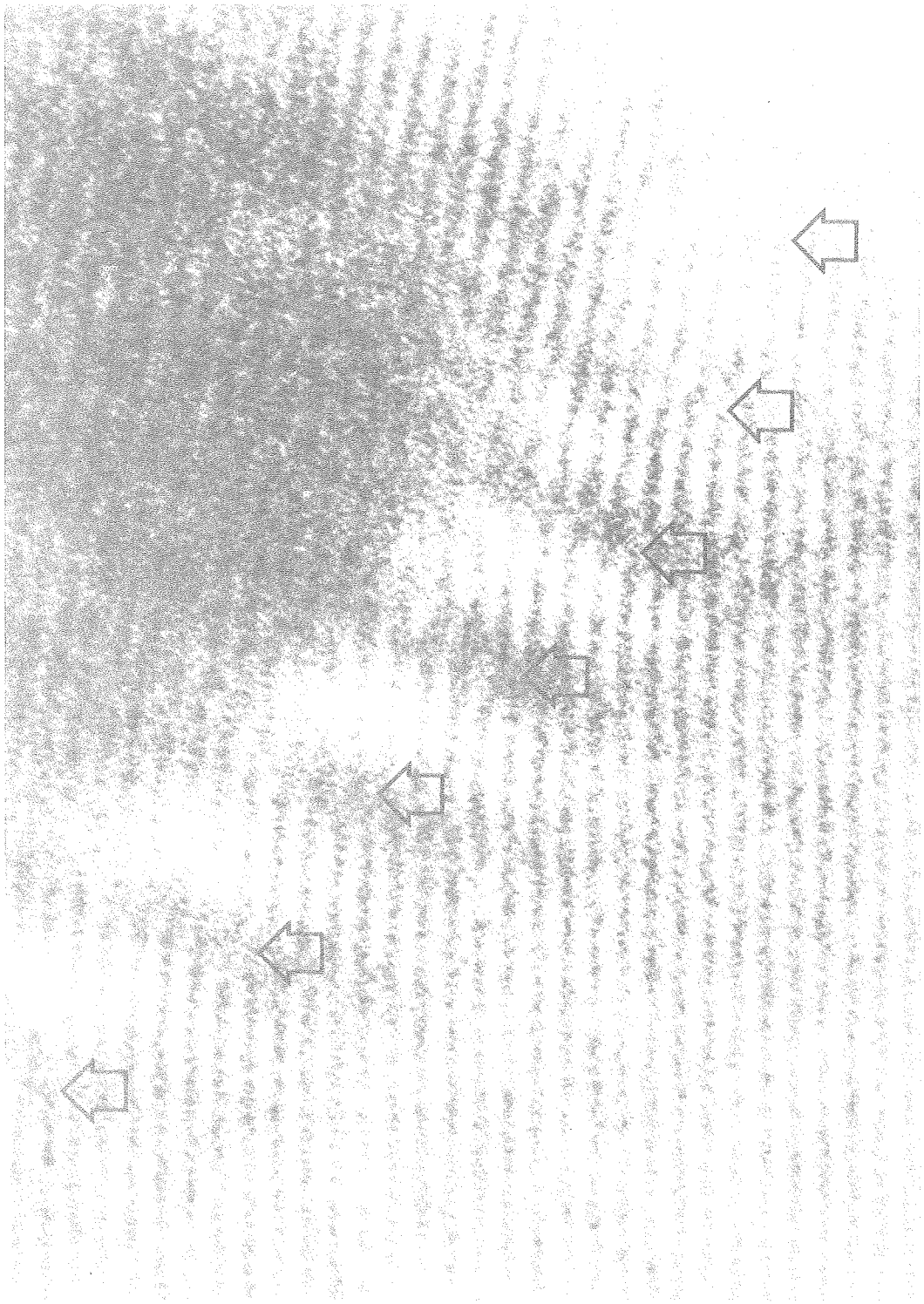

XBB 767-6627

Fig. 14

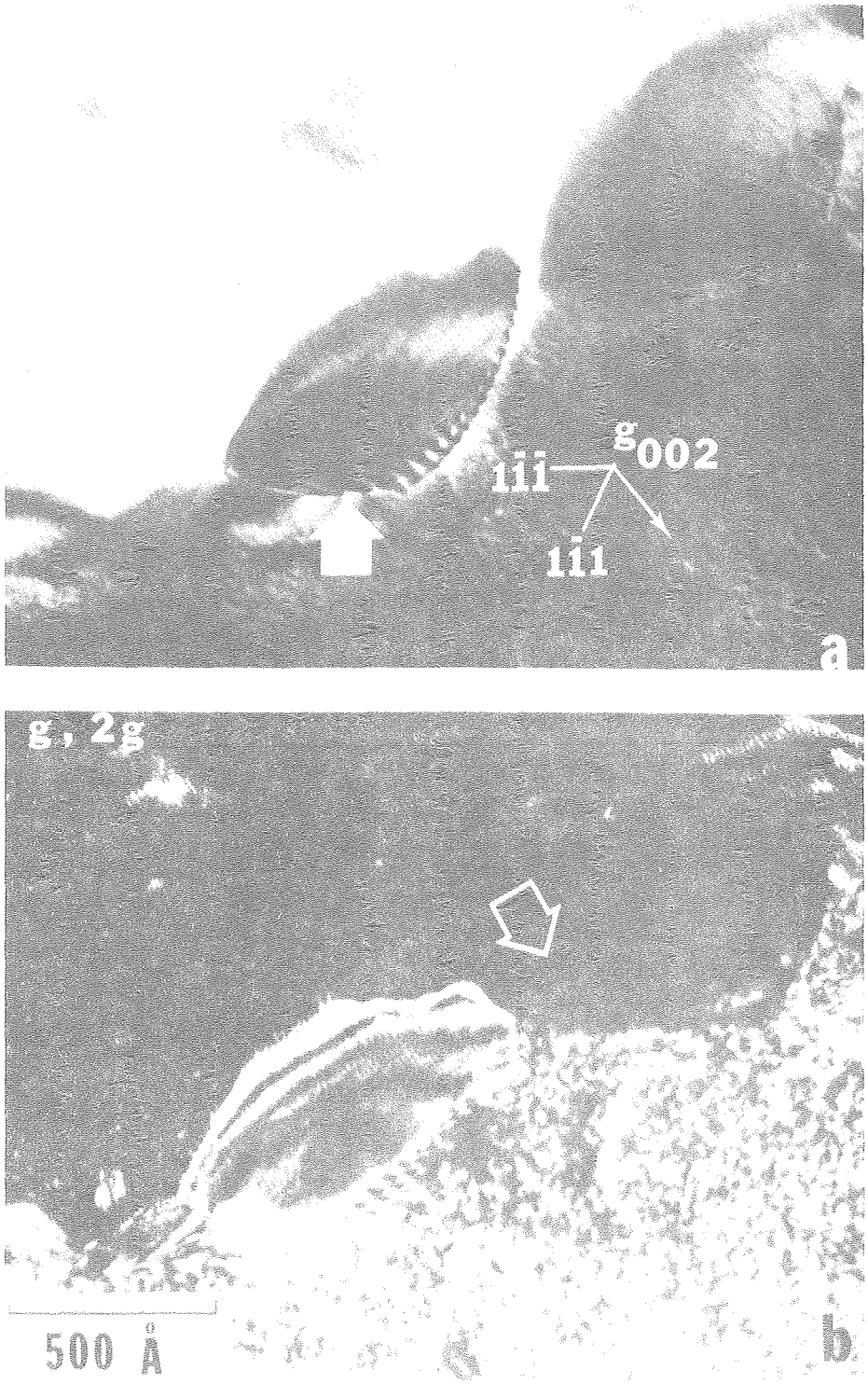

XBB 7611-10500

Fig. 15

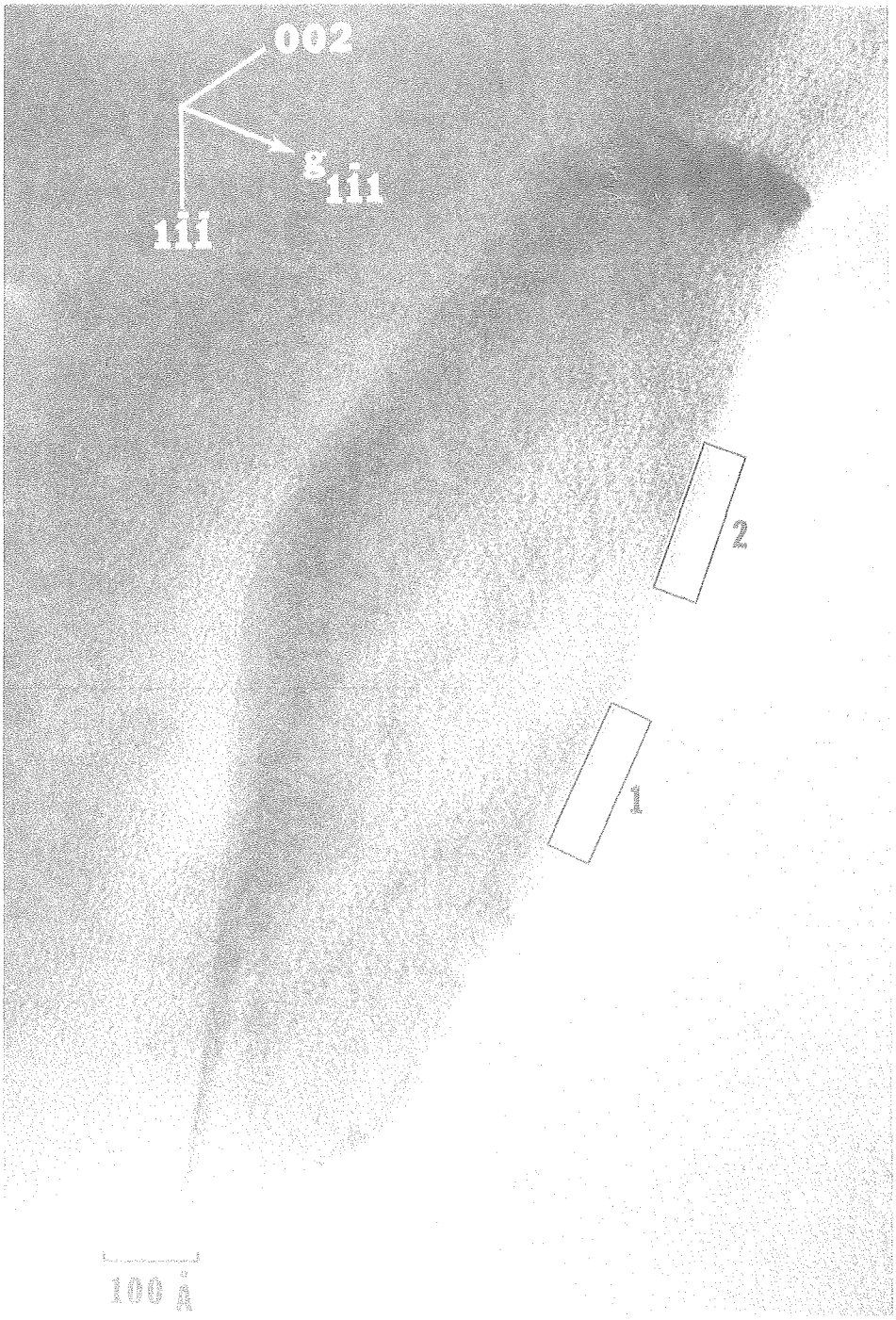

XBB 7611-10510

Fig. 16

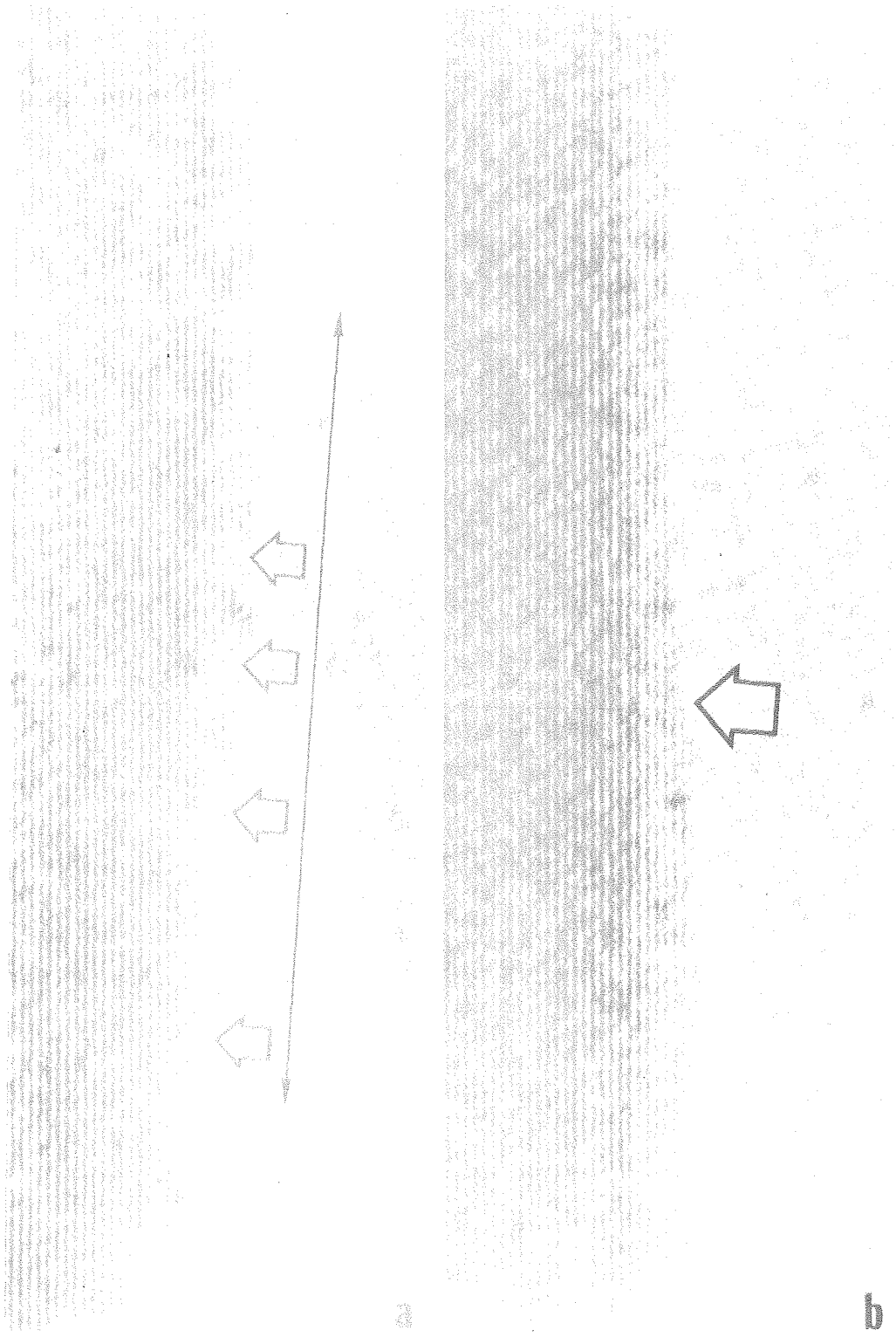

XBB 7611-10511

Fig. 17

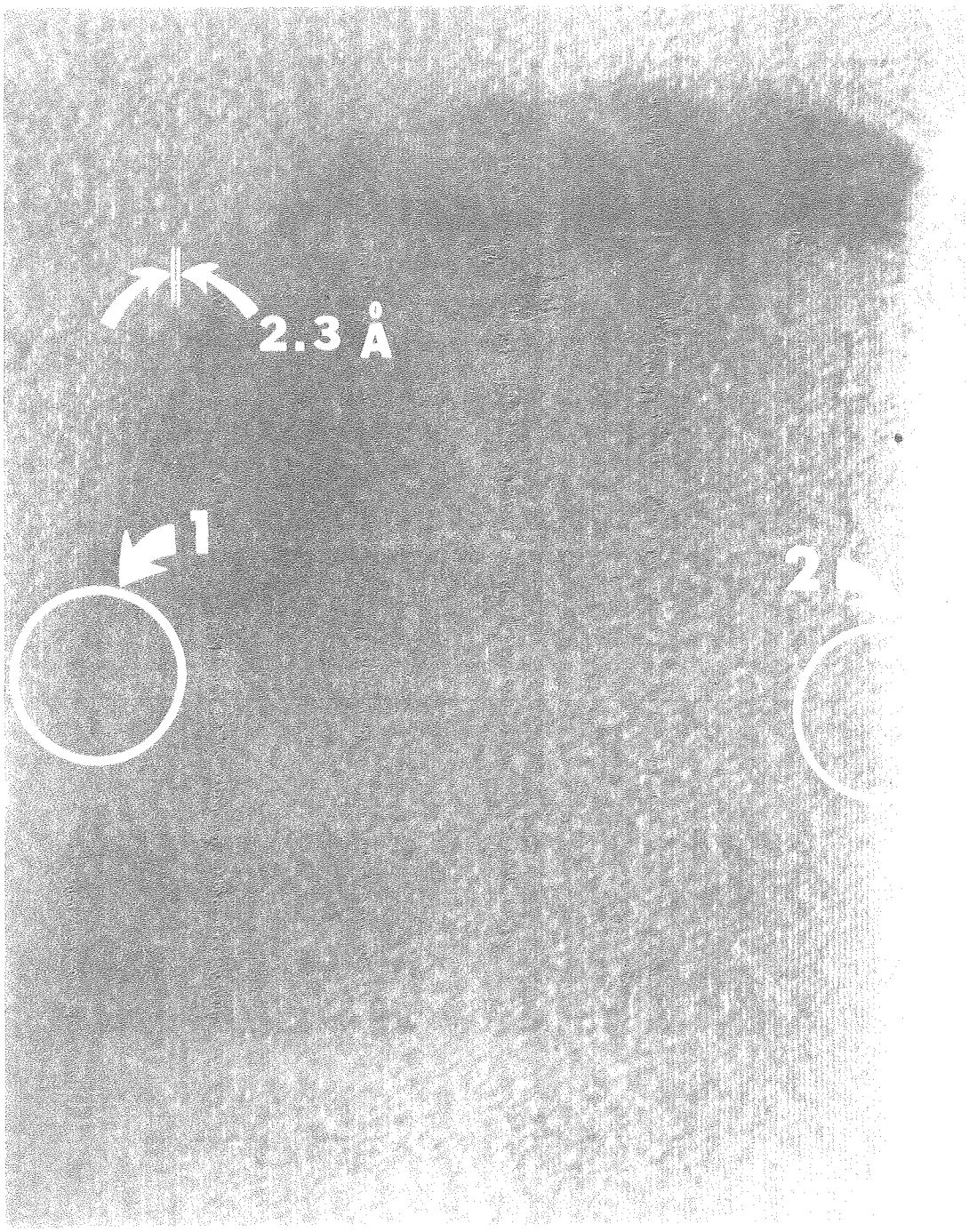

XBB 7611-10512

Fig. 18(a)

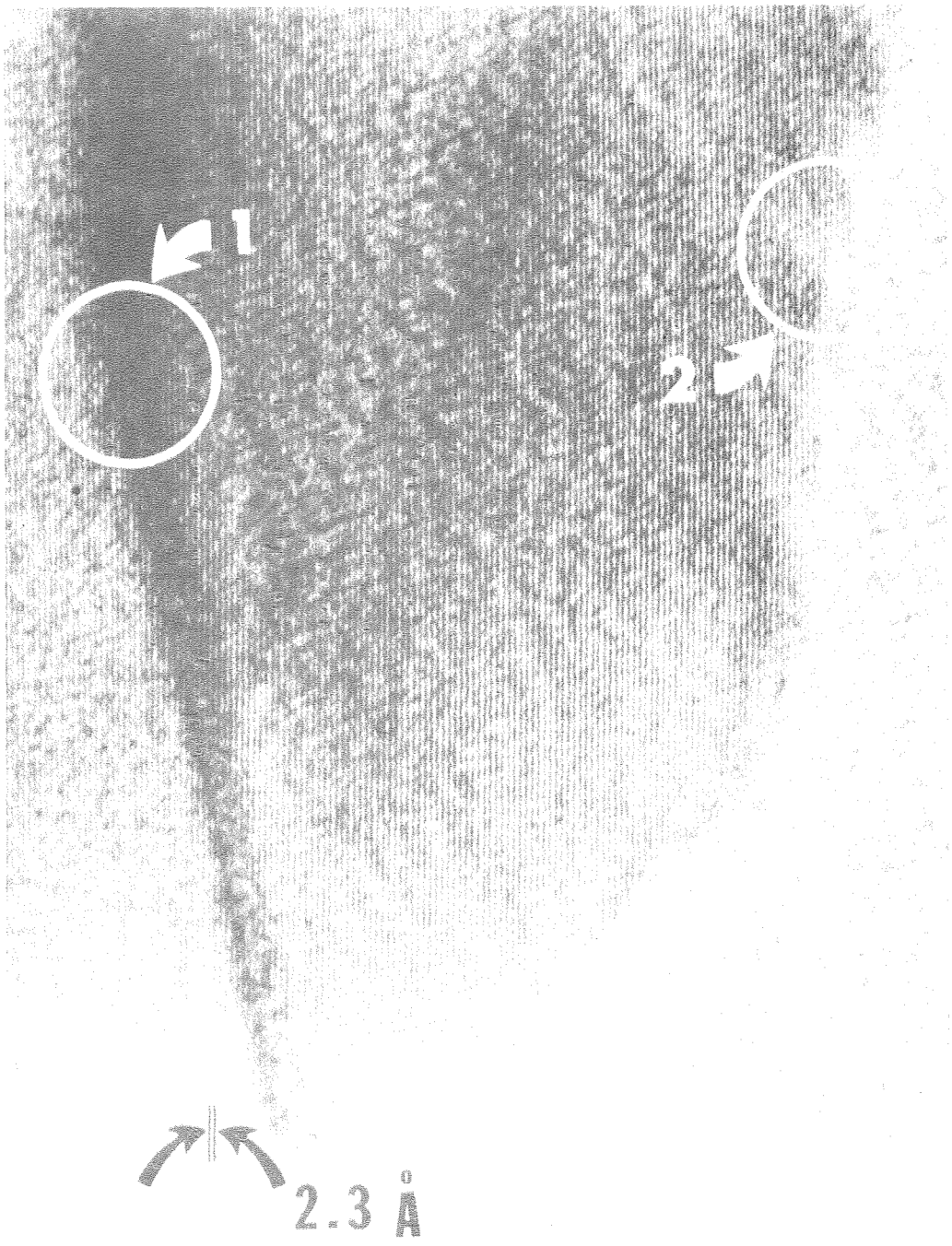

XBB 7611-10513

Fig. 18(b)

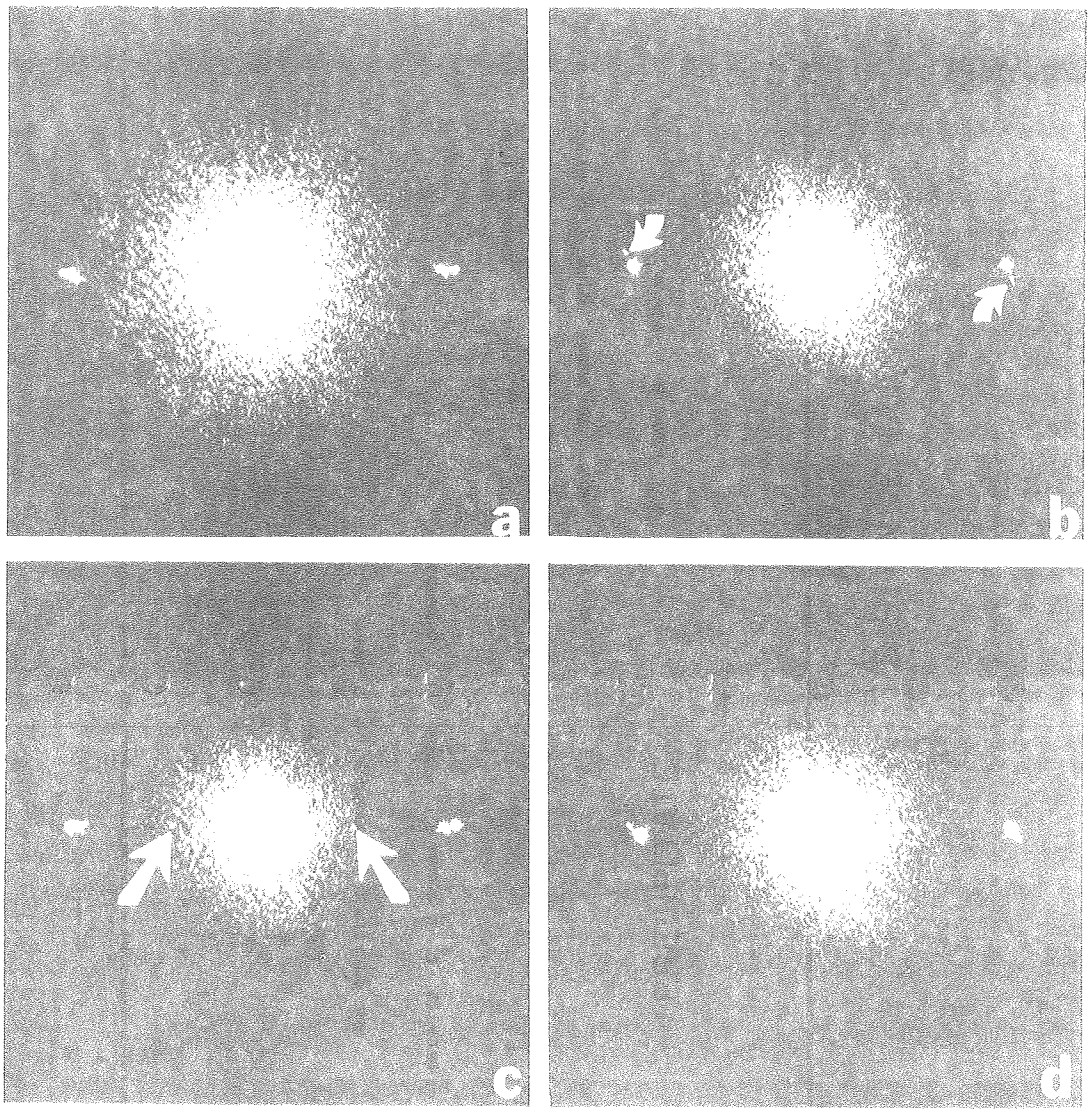

XBB 7611-10527

Fig. 19

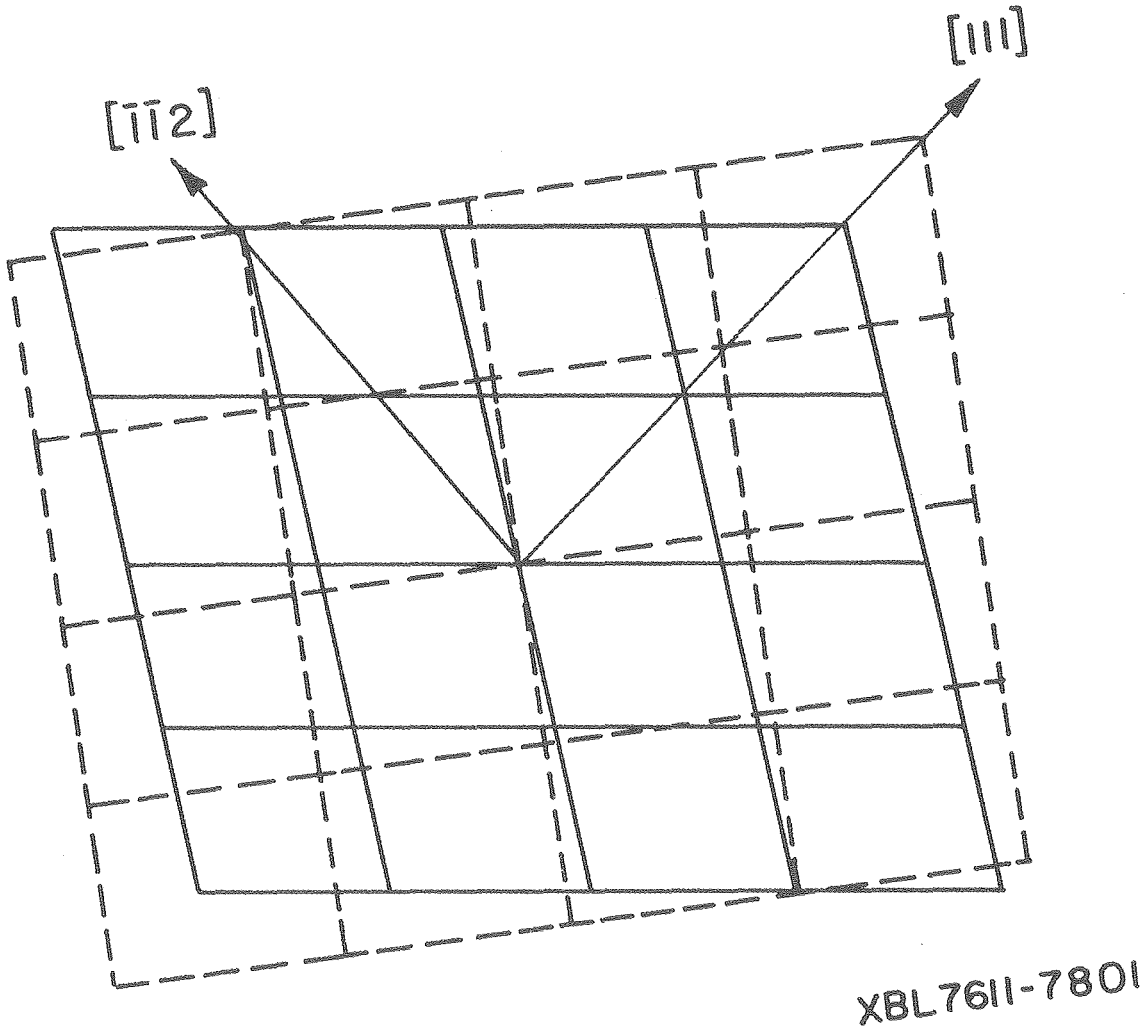

Fig. 20

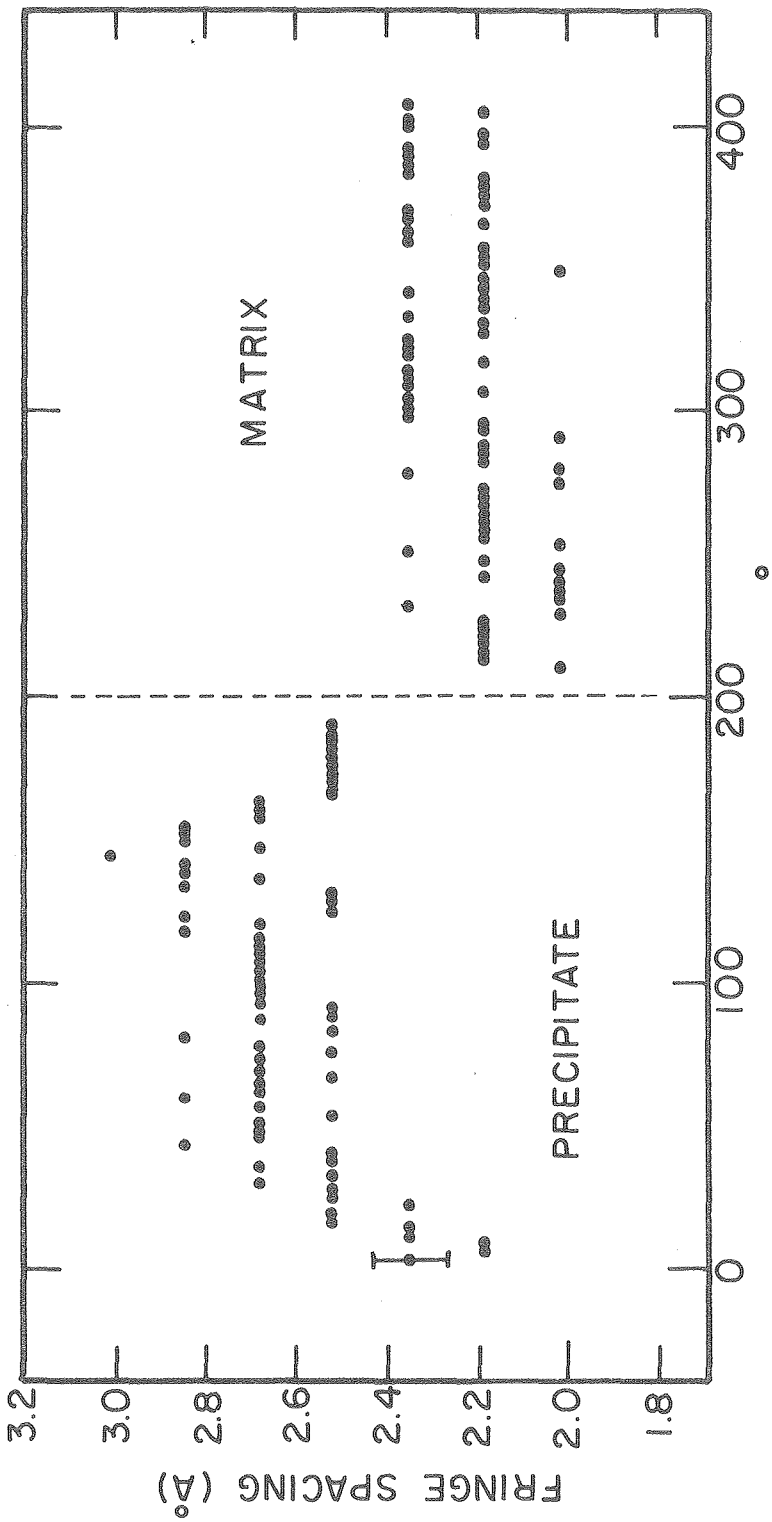

XBL 7611-7803

Fig. 21

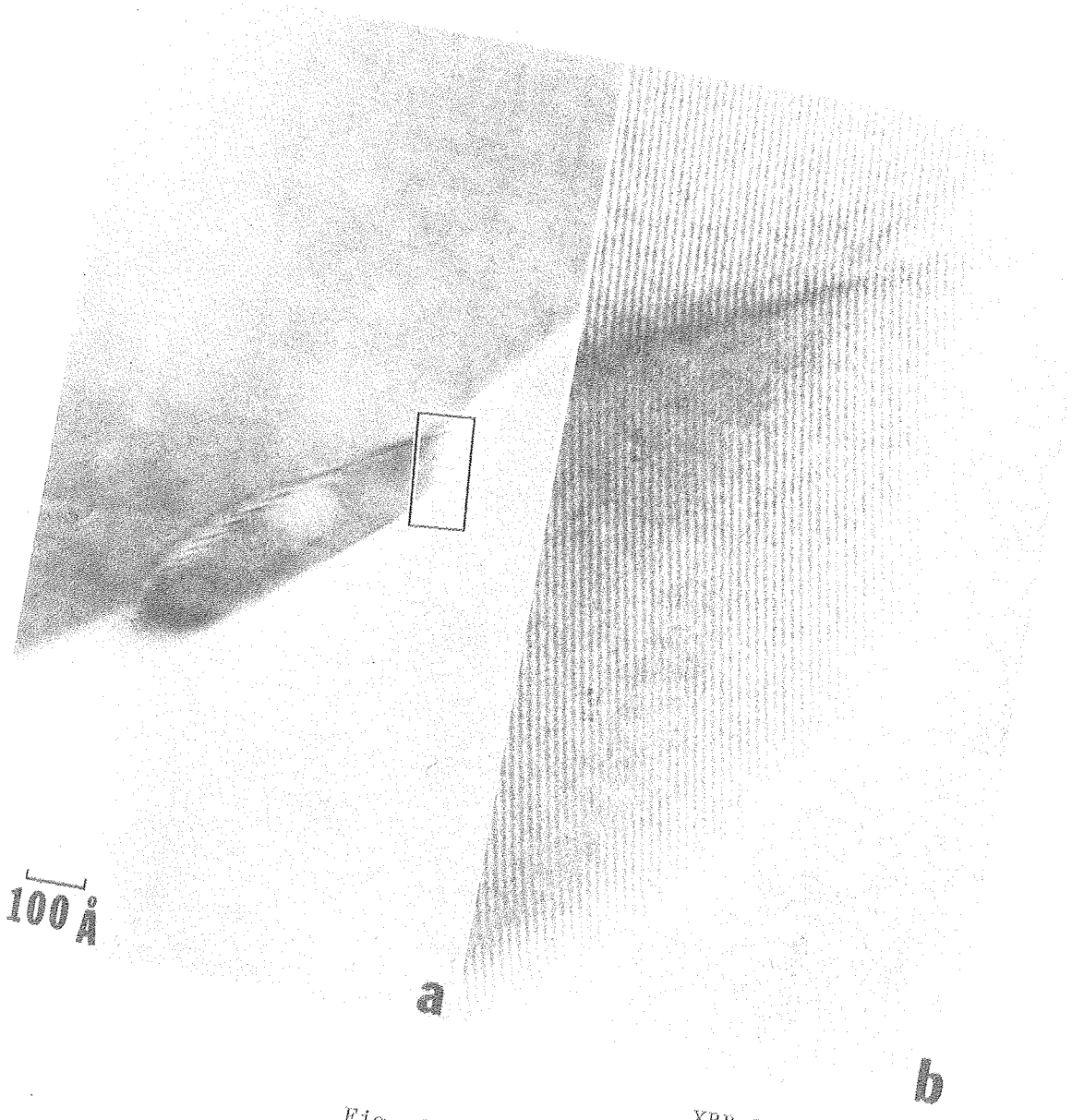

Fig. 22

XBB 7611-10514

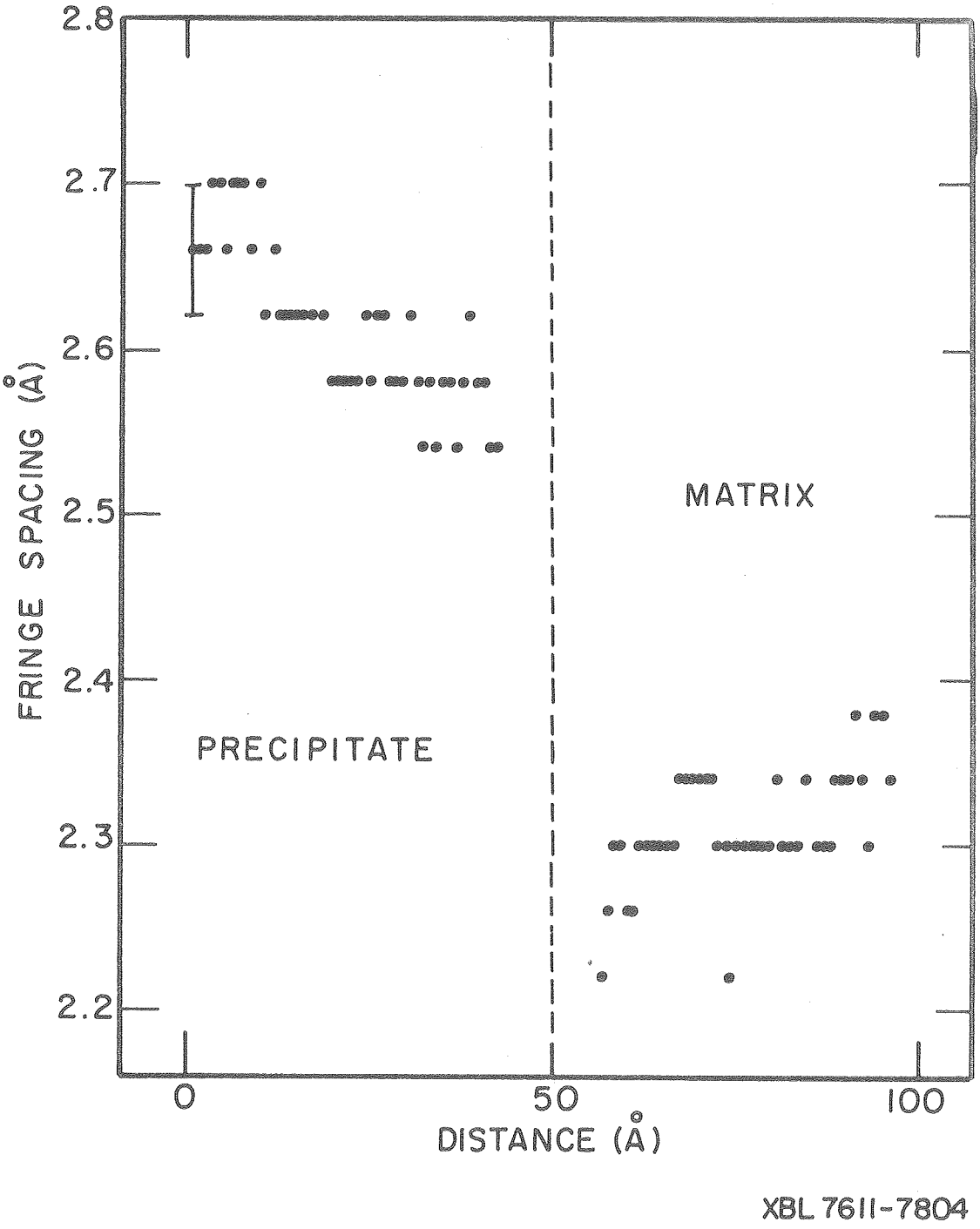

Fig. 23

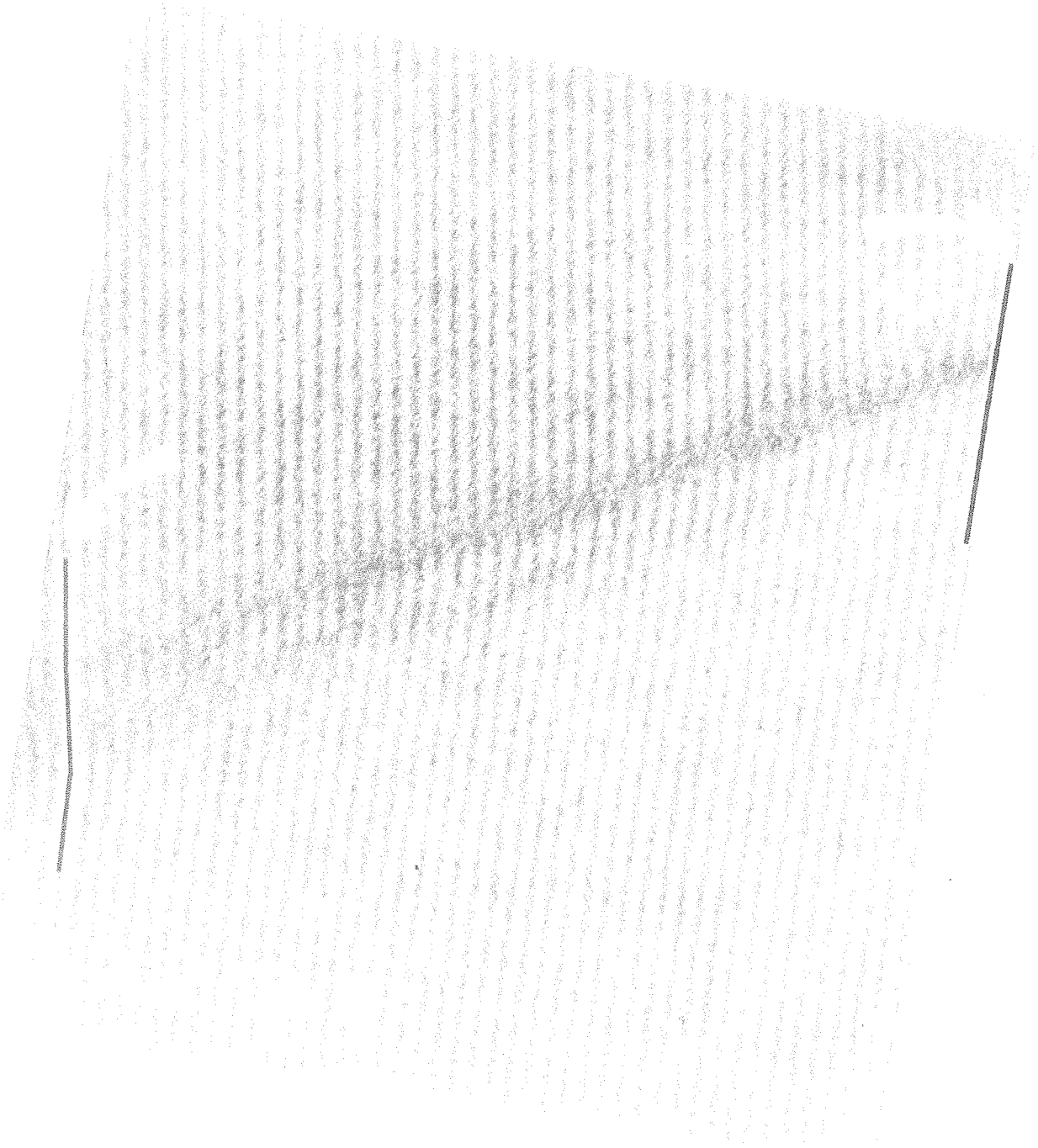

Fig. 24

XBB 7611-10532

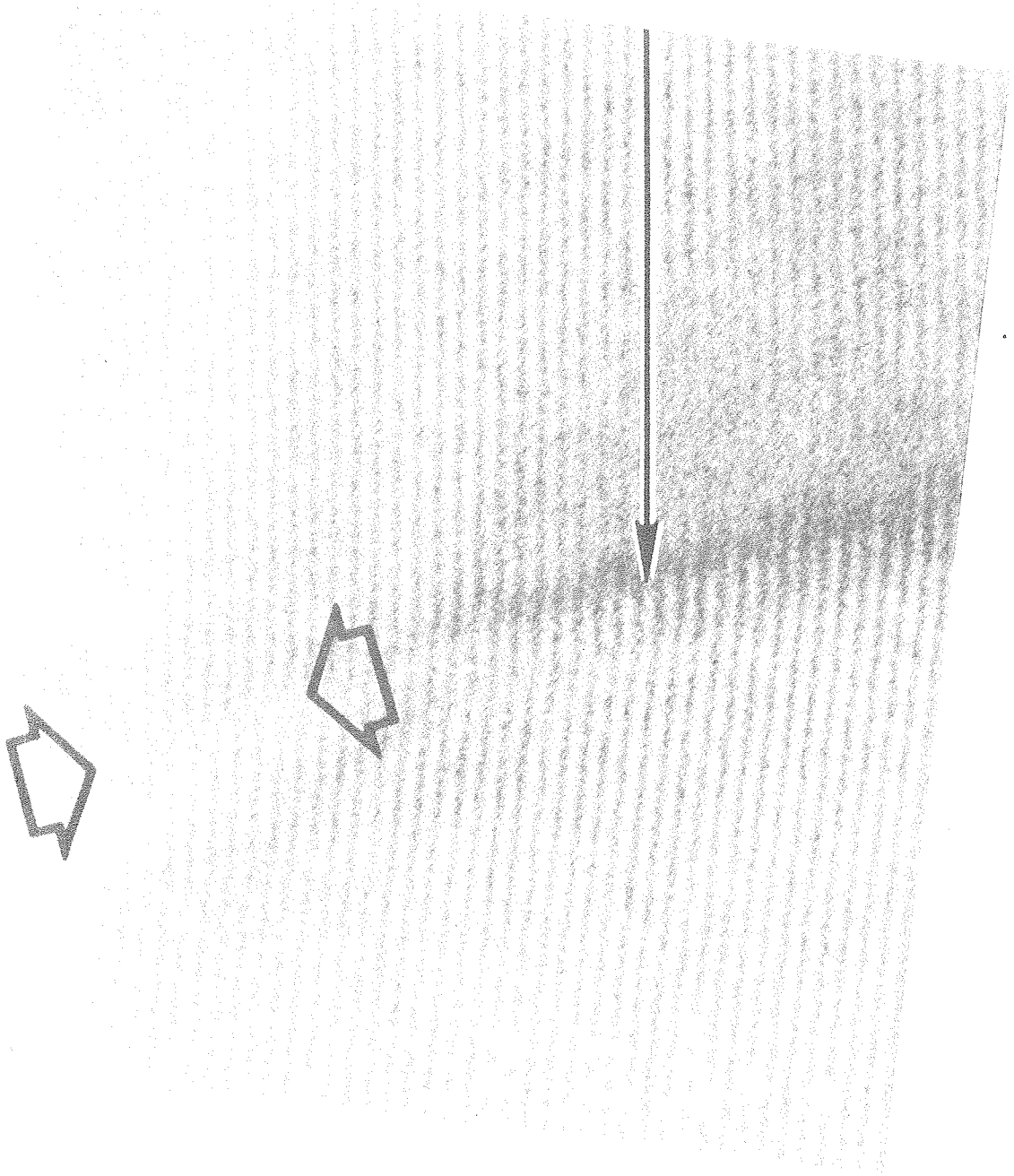

XBB 7611-10531

Fig. 25

XBB 7611-10533

Fig. 26

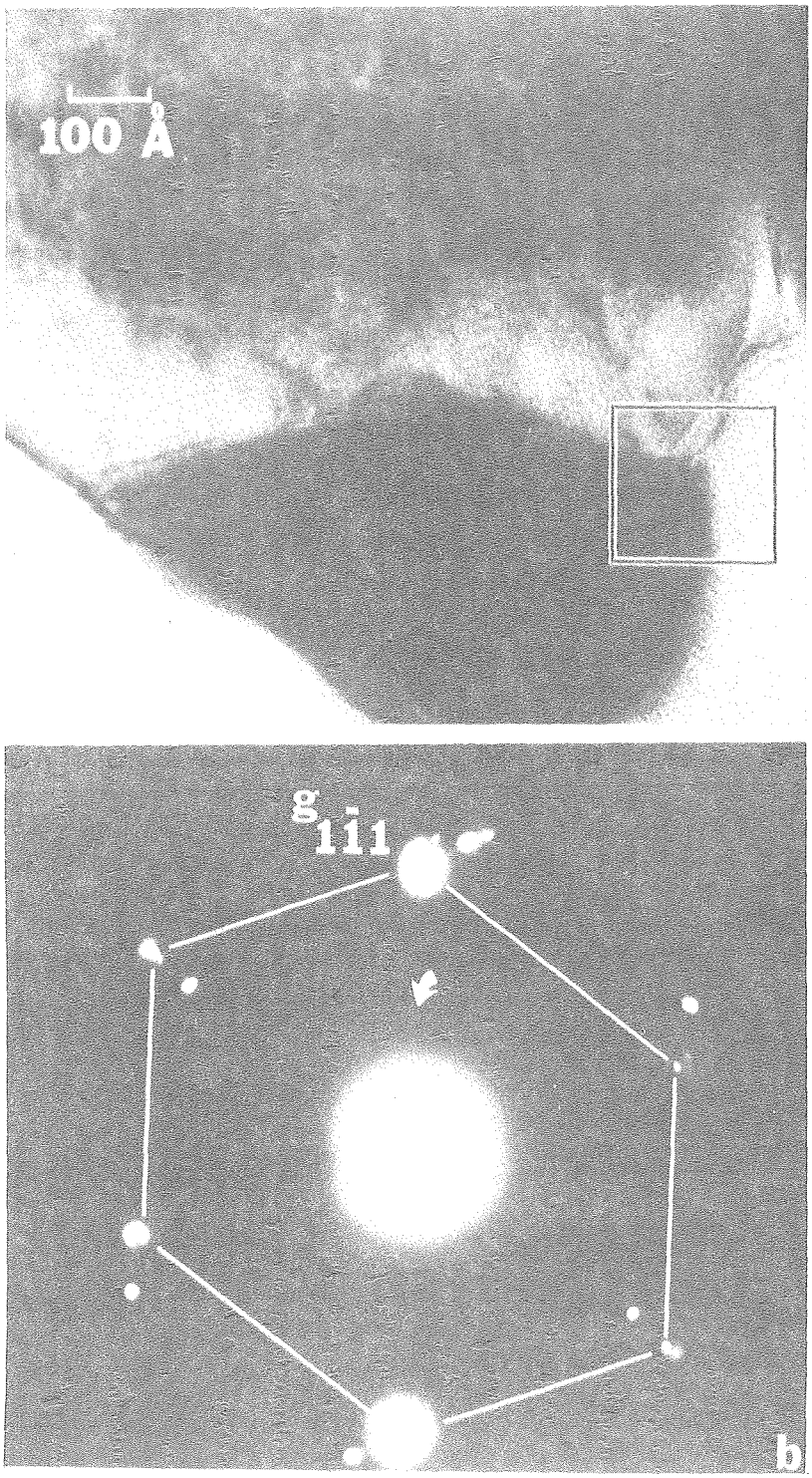

XBB 7611-10498

Fig. 27

XBB 767-6531

Fig. 28

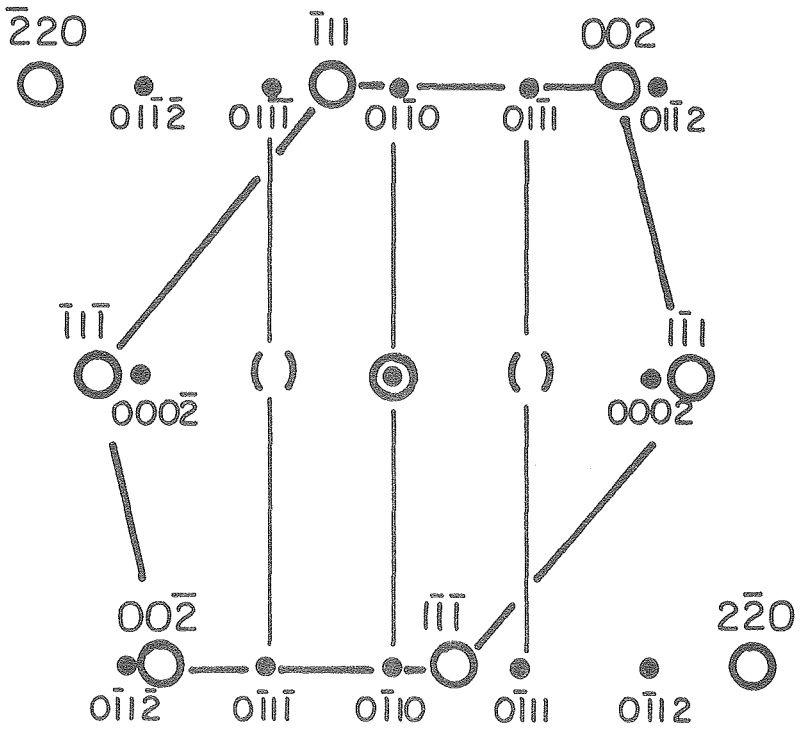

Fig. 29

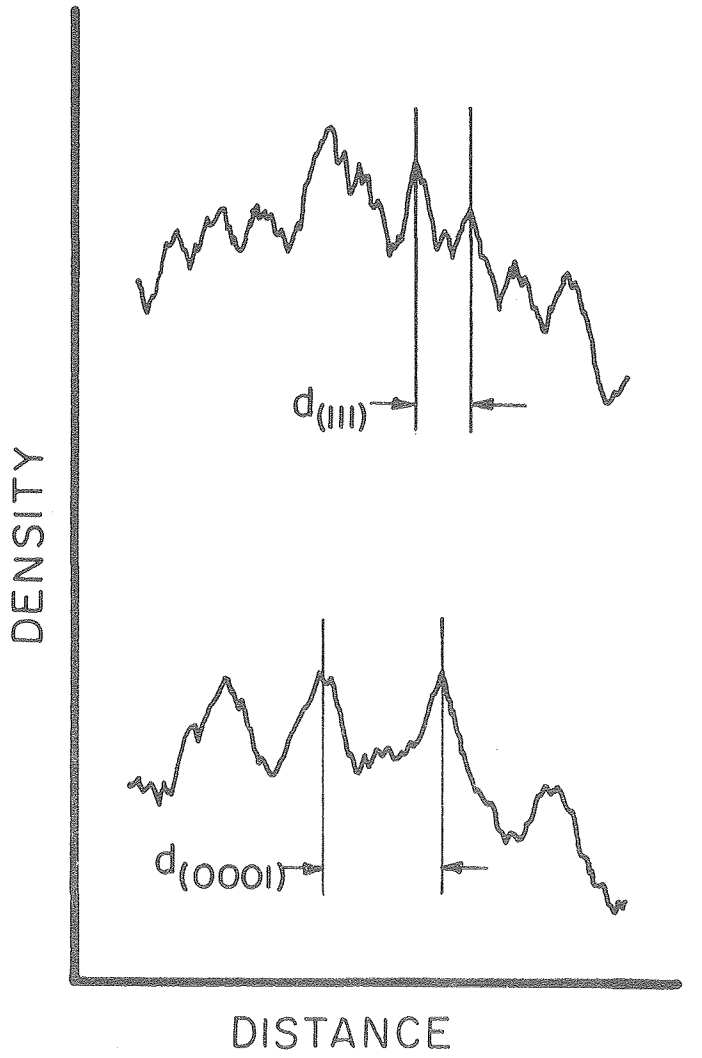

XBL7611-7799

Fig. 30

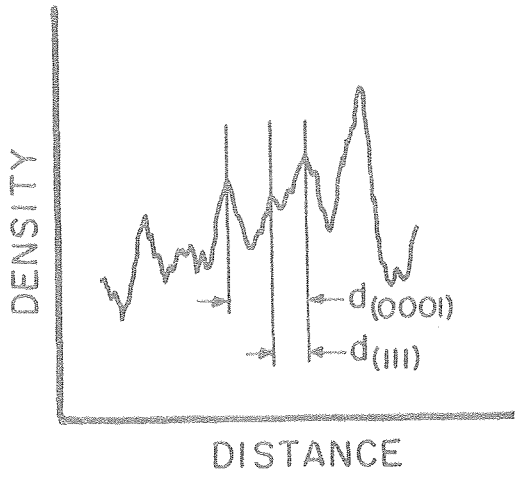

a

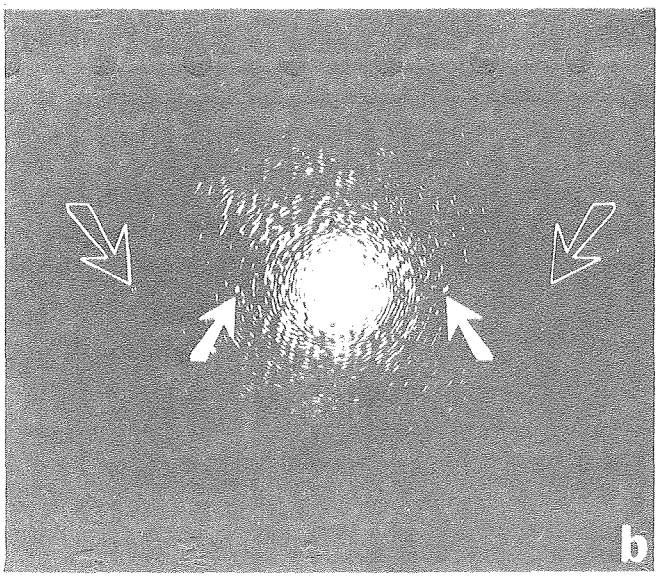

XBB 7611-10496

Fig. 31

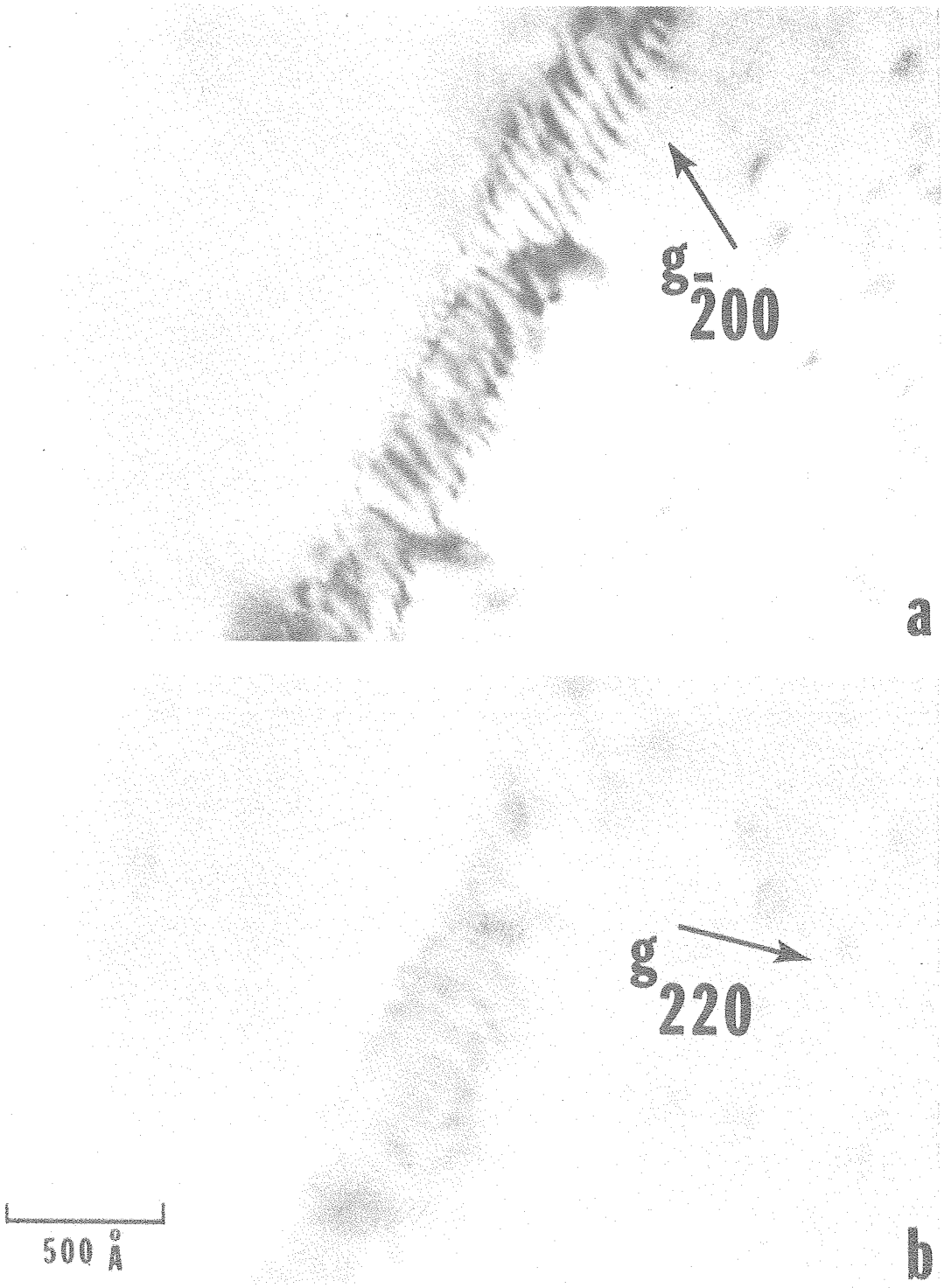

XBB 7611-10518

Fig. 32

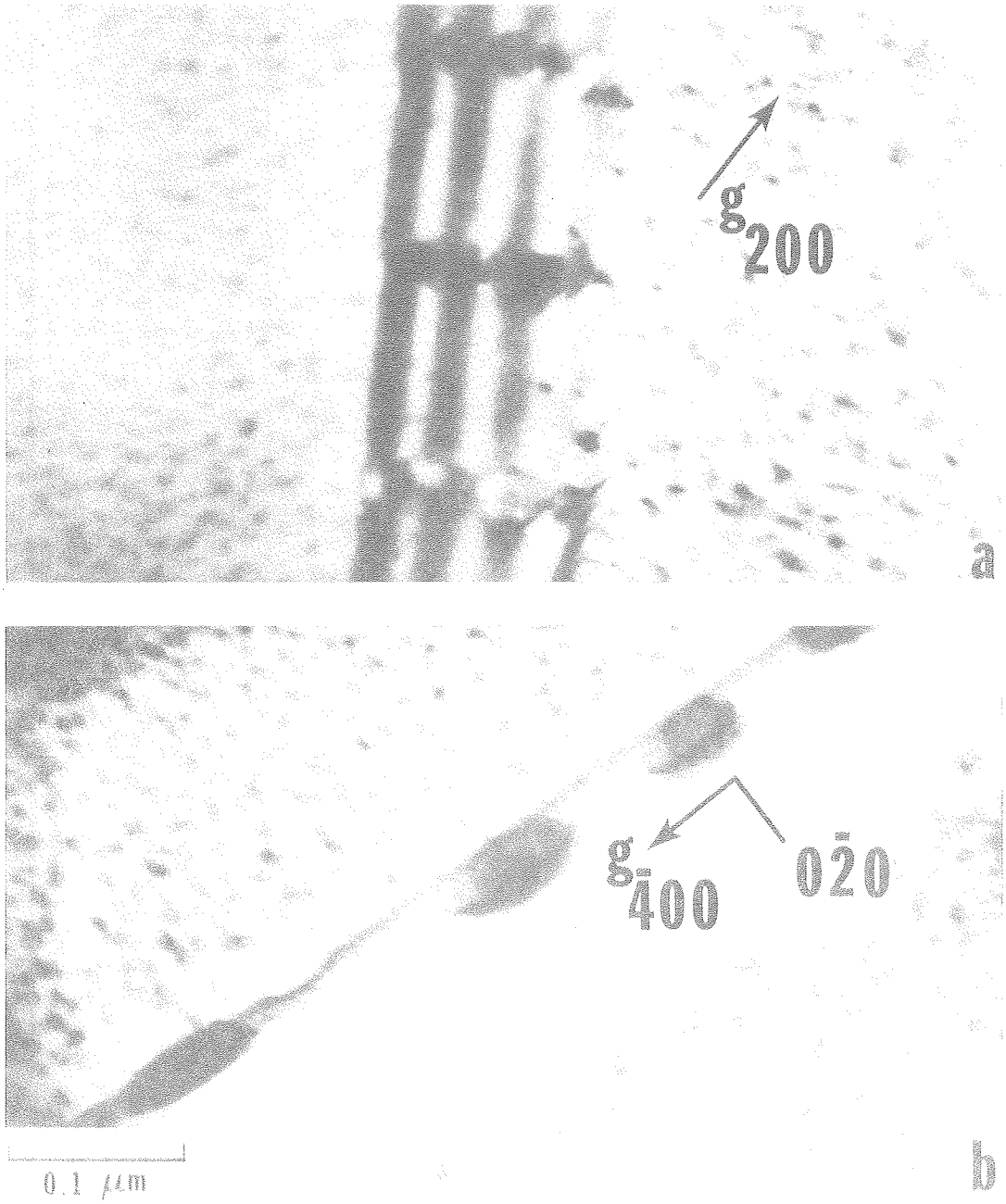

XBB 7611-10521

Fig. 33

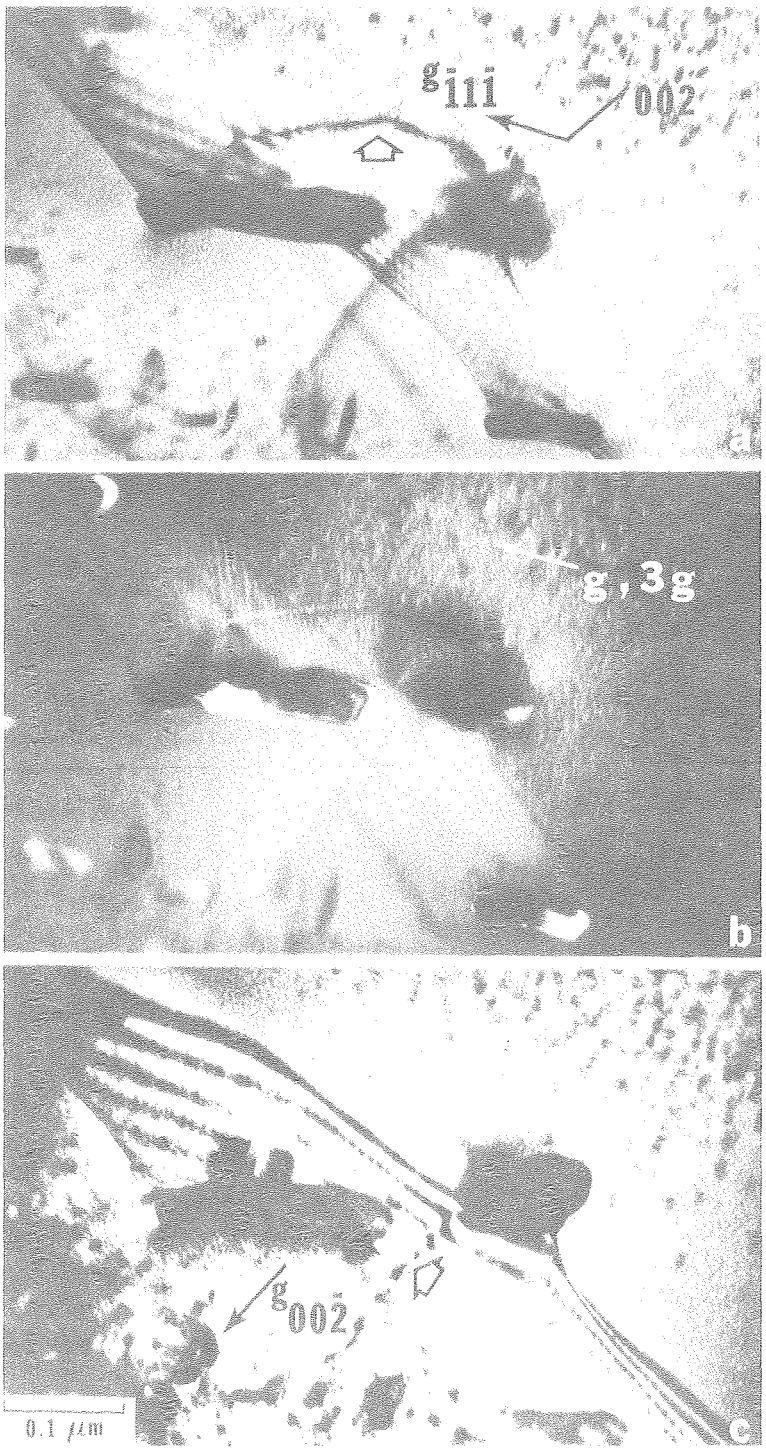

XBB 7611-10502

Fig. 34

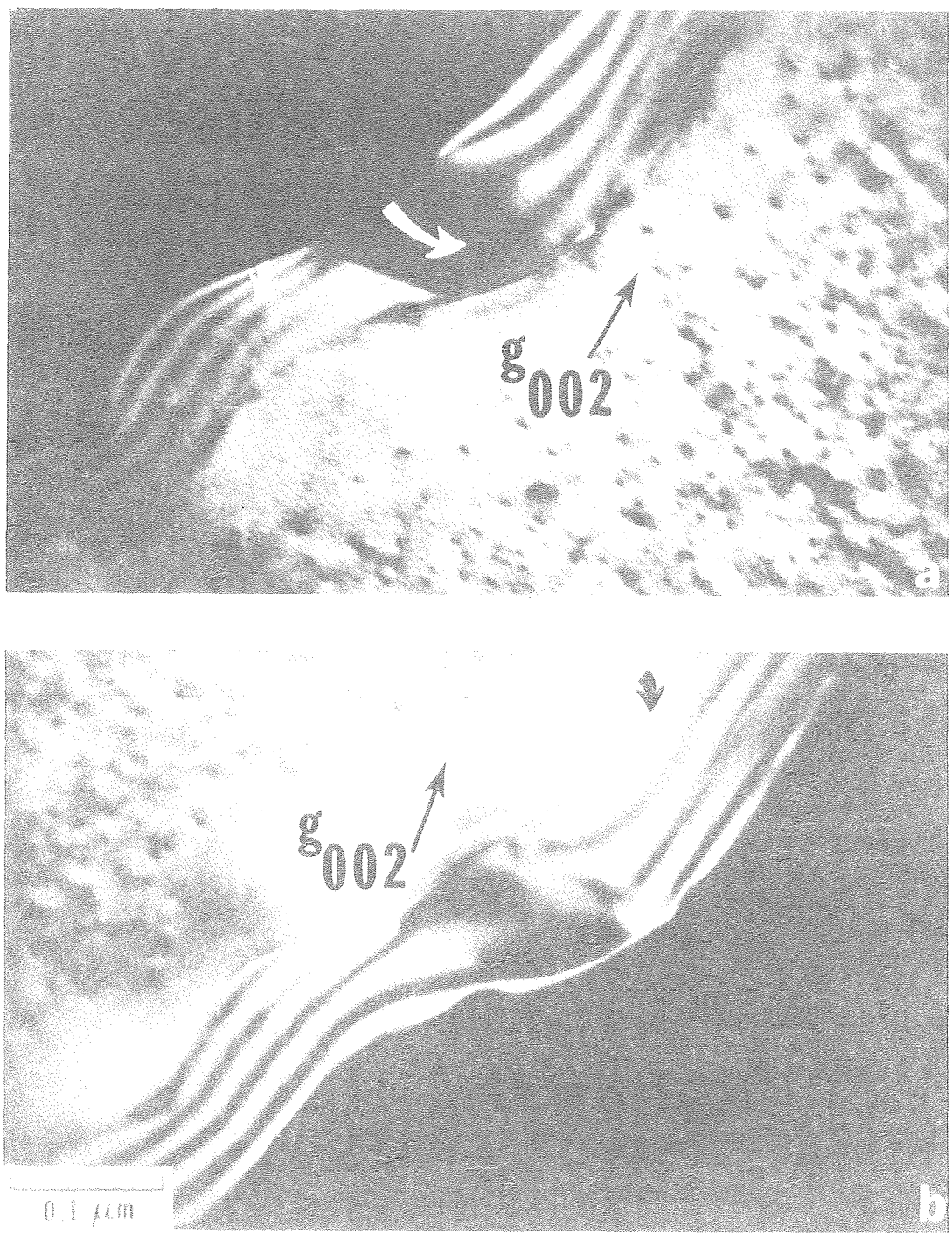

XBB 7611-10522

Fig. 35

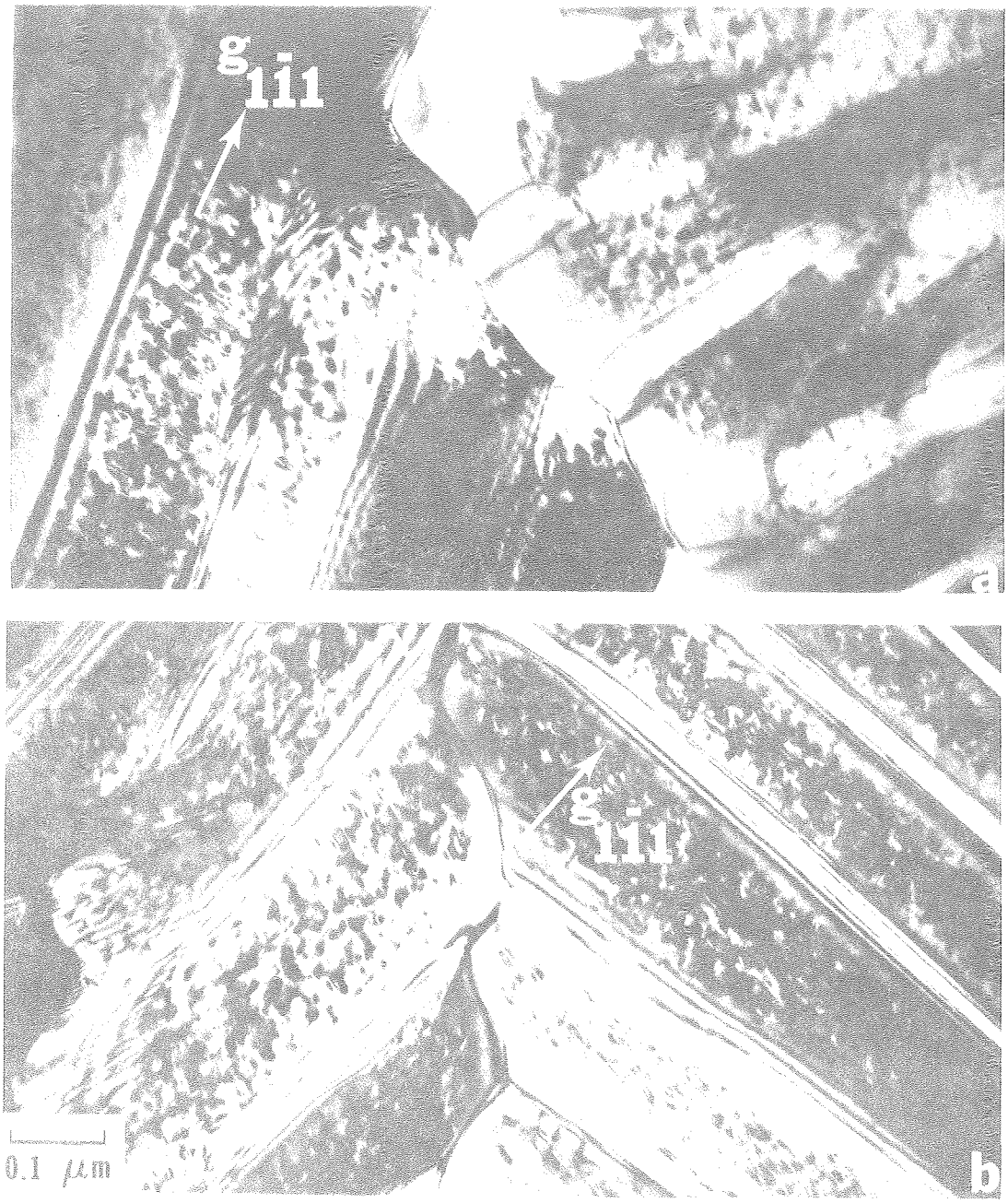

XBB 7611-10520

Fig. 36

XBB 7611-10507

Fig. 37

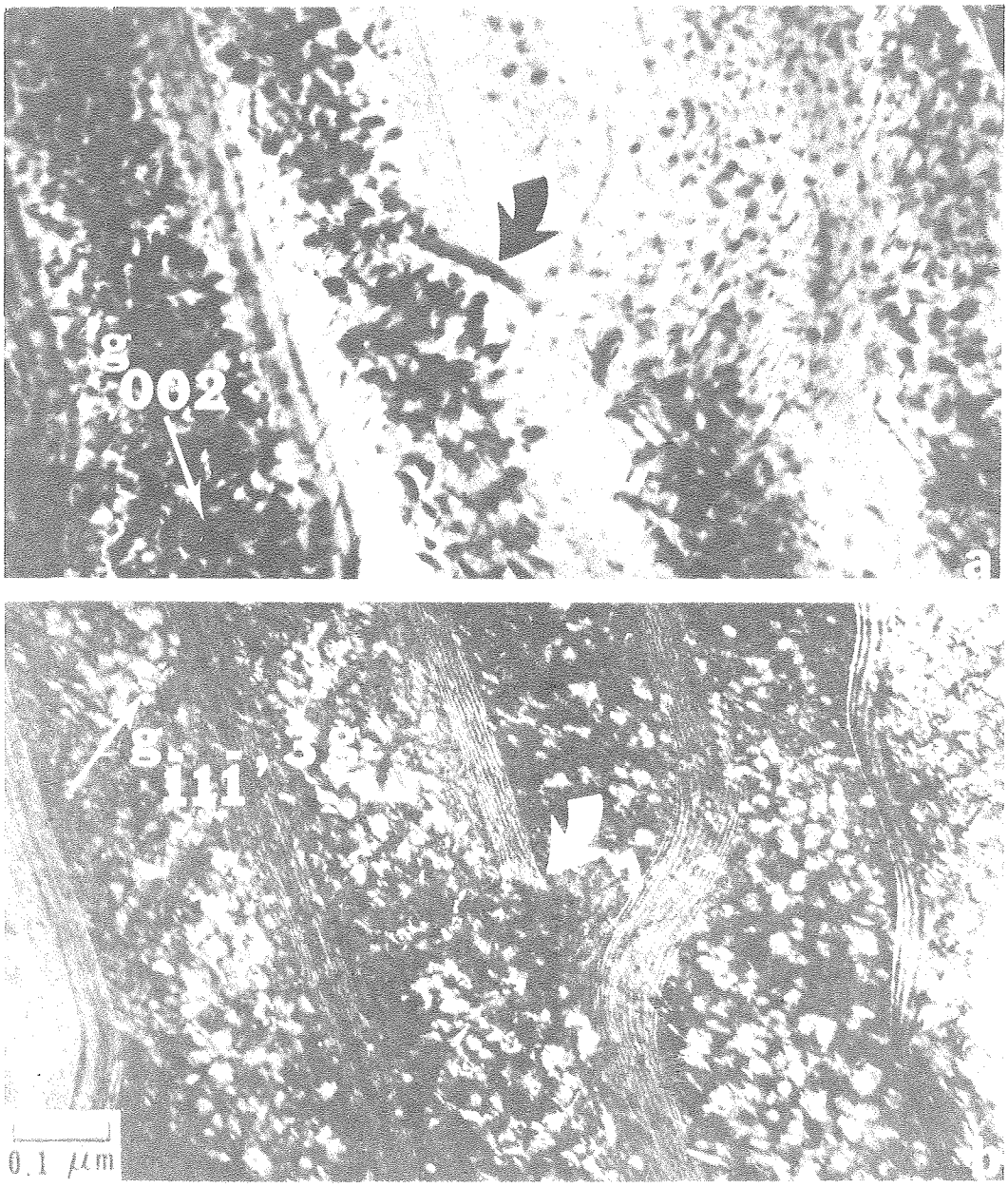

XBB 7611-10517

Fig. 38

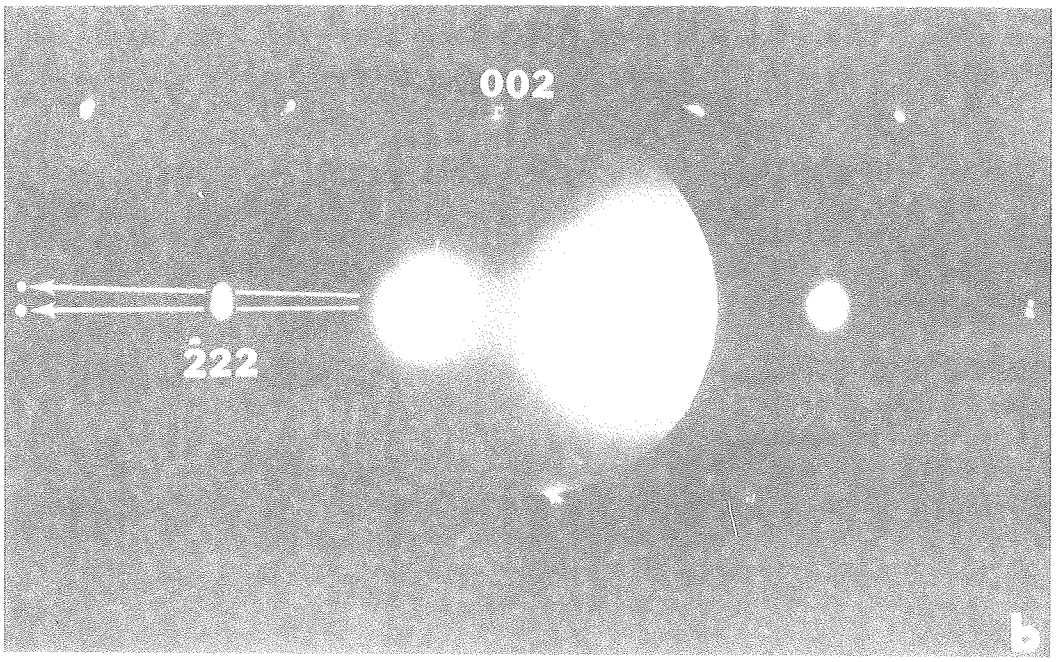

XBB 7611-10508

Fig. 39

XBB 767-6530

Fig. 40

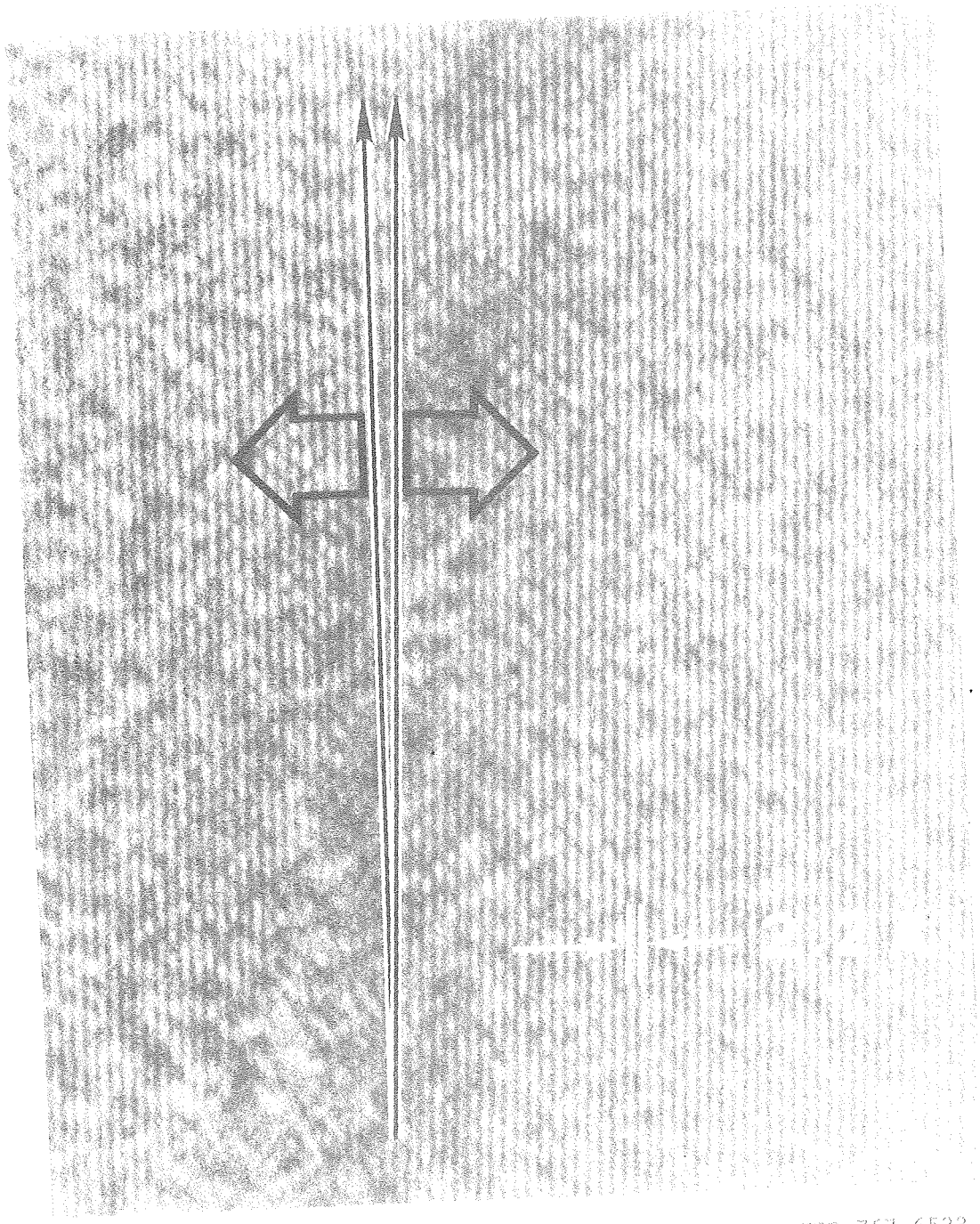

XBB 767-6533

Fig. 41

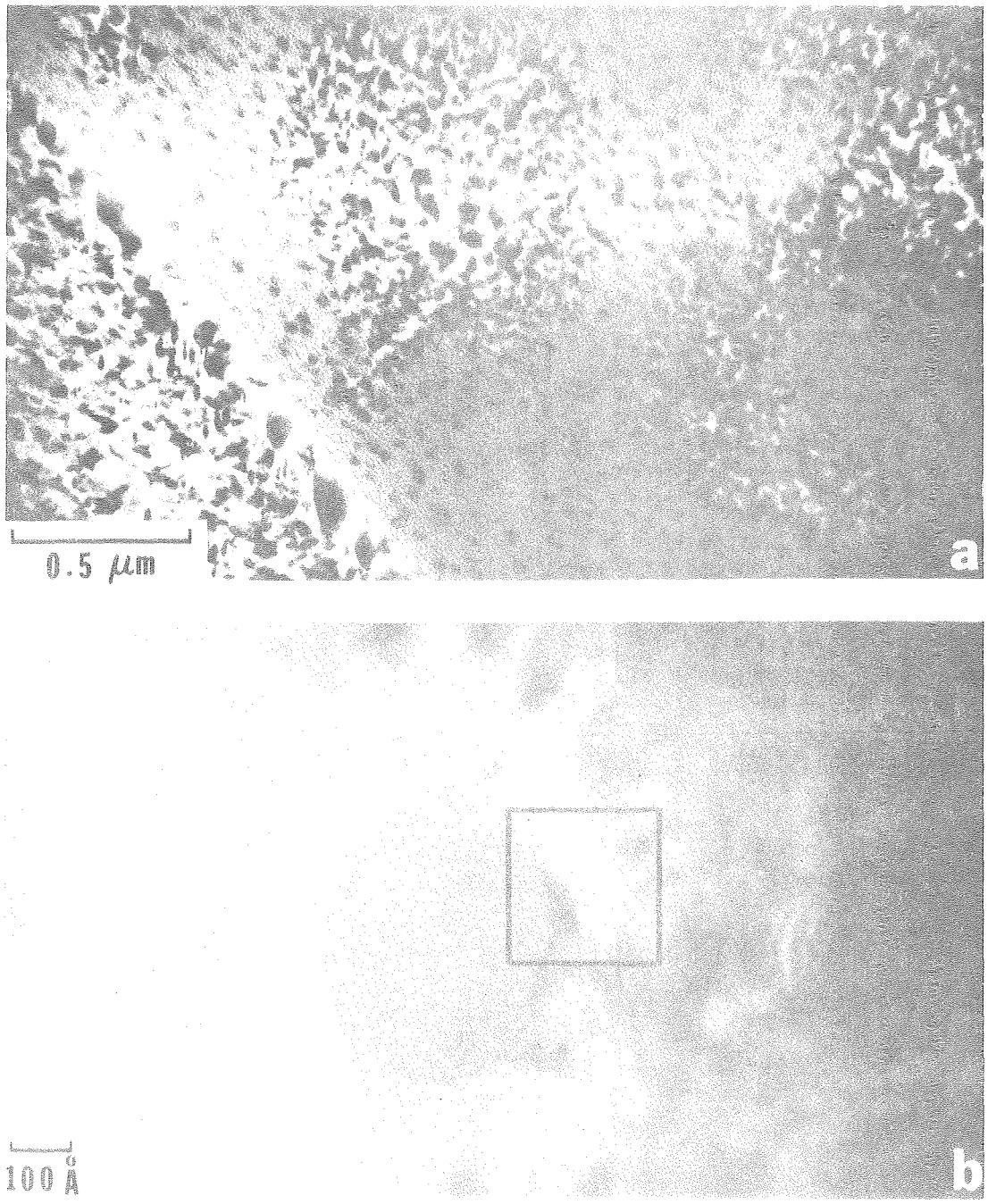

XBB 7611-10519

Fig. 42

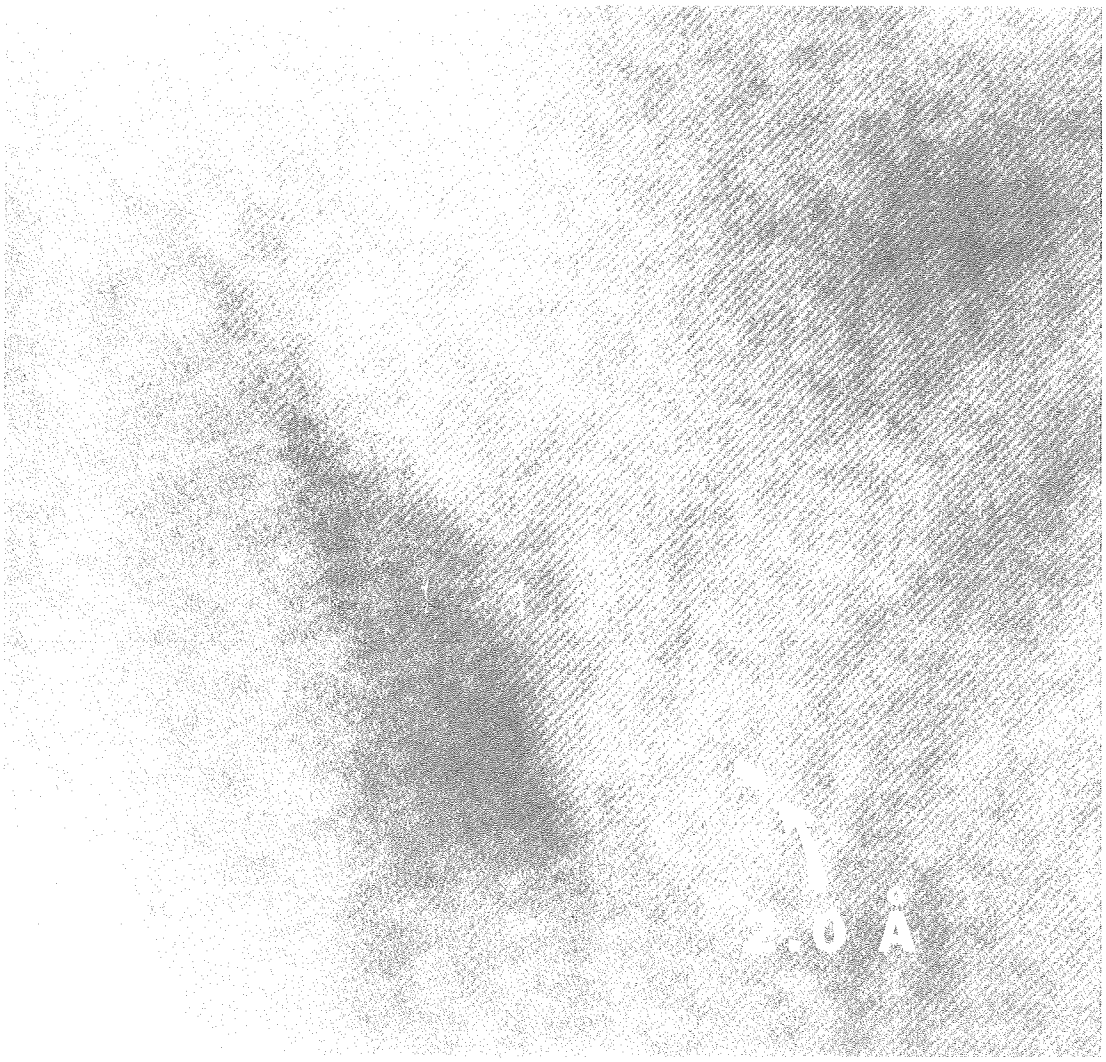

XBB 7611-10529

Fig. 43

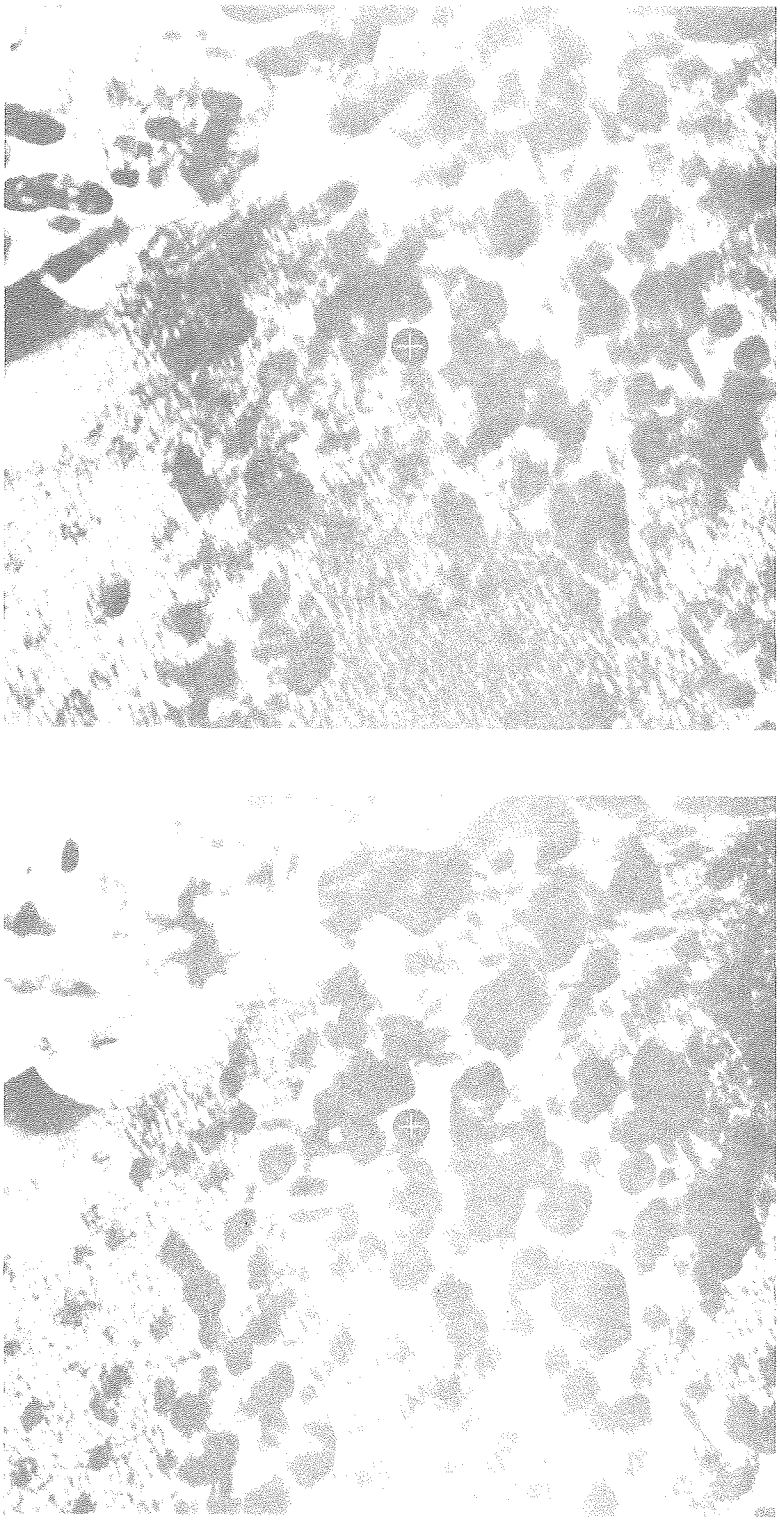

XBB 7611-10523

Fig. 44(a)

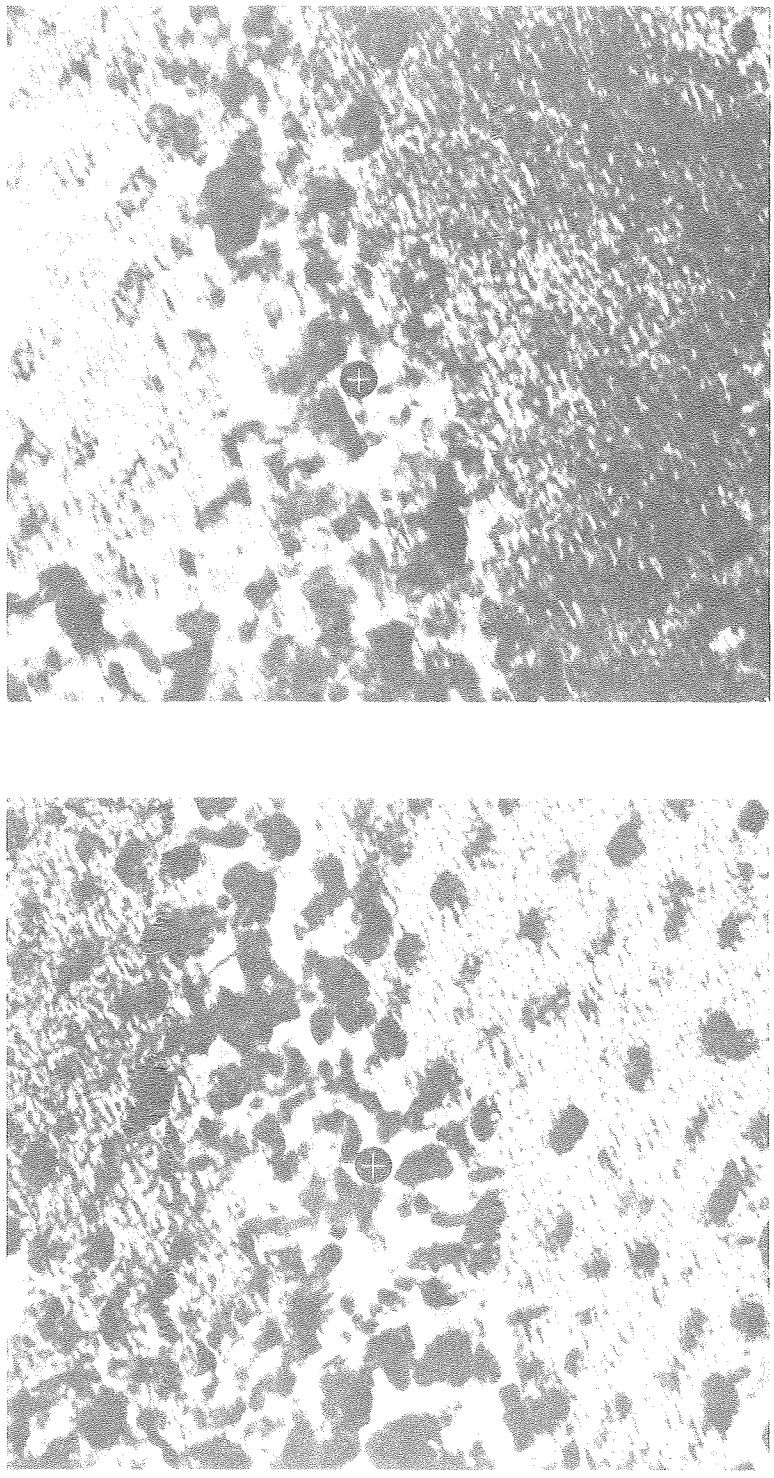

XBB 7611-10524

Fig. 44(b)

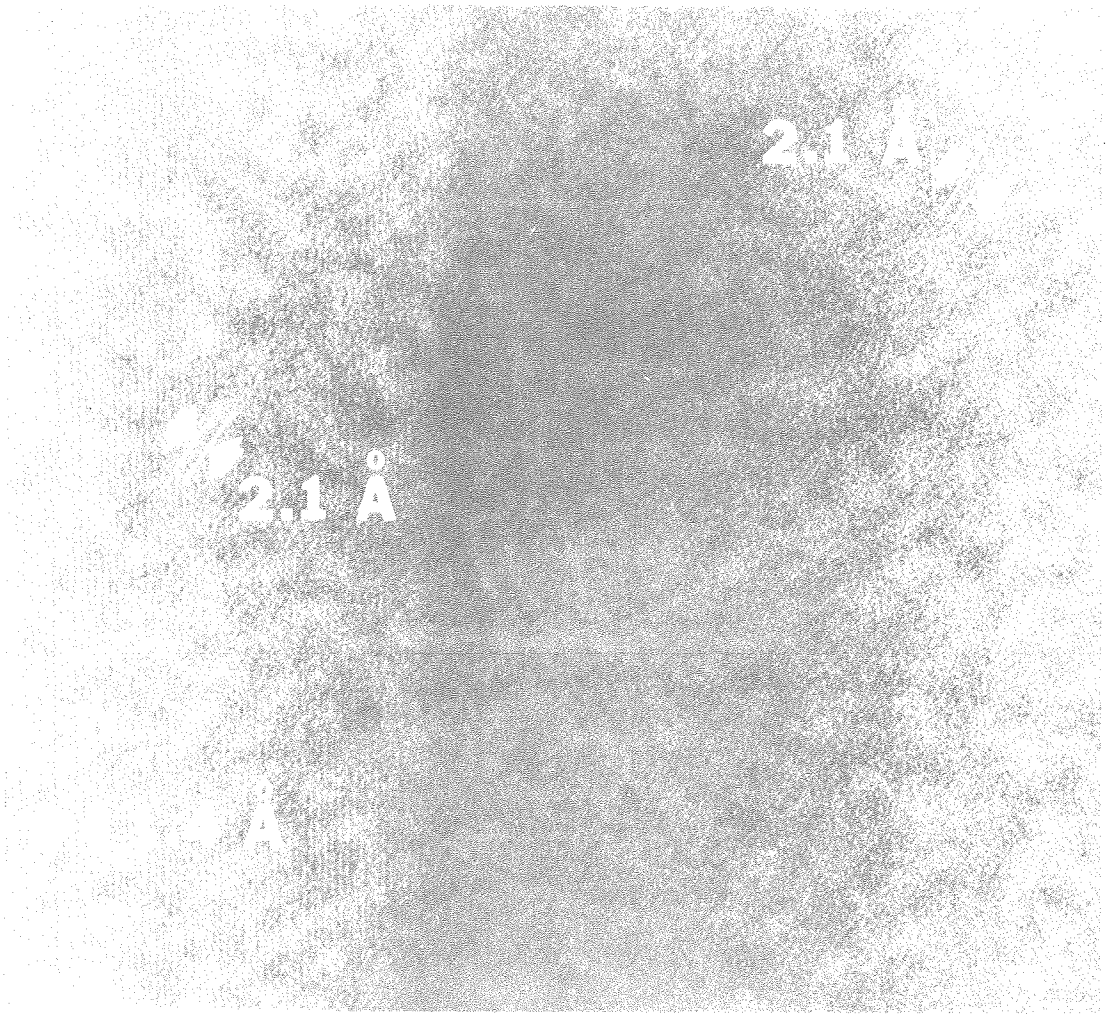

XBB 7611-10528

Fig. 45

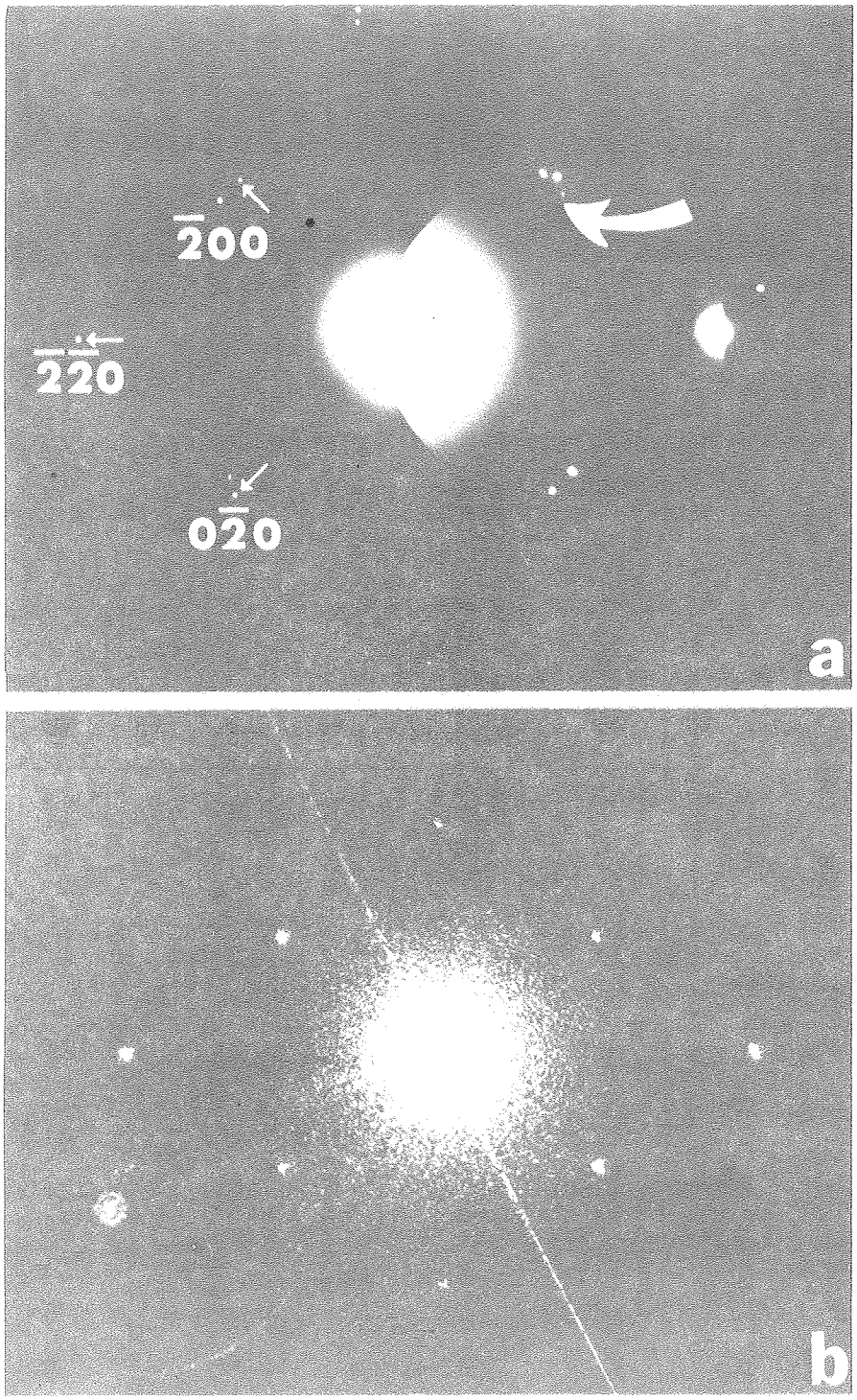

XBB 7611-10530

Fig. 46

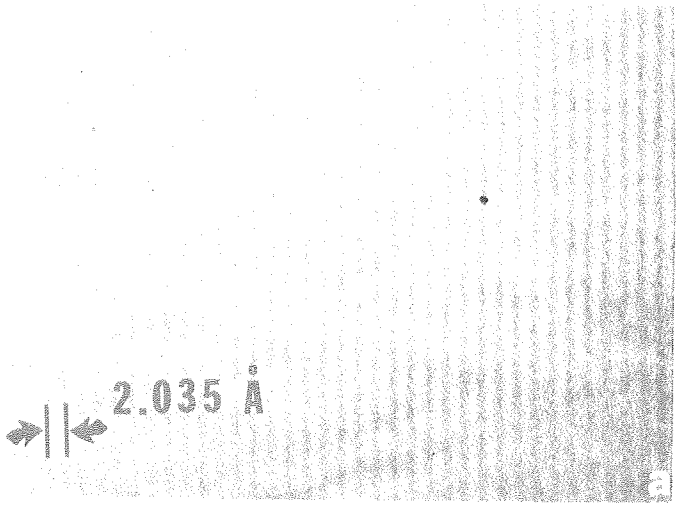

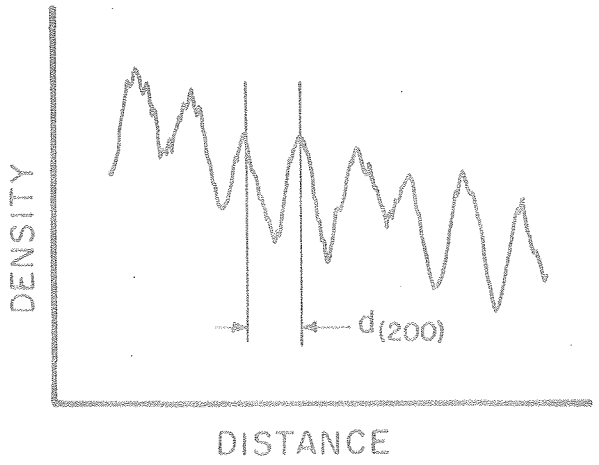

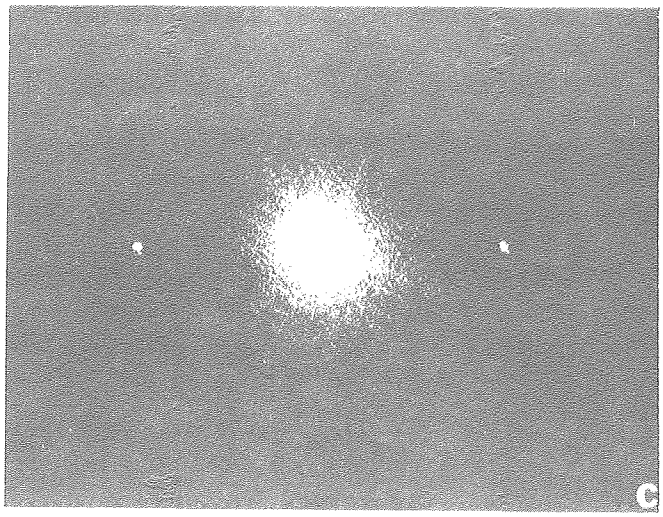

XBB 7611-10497

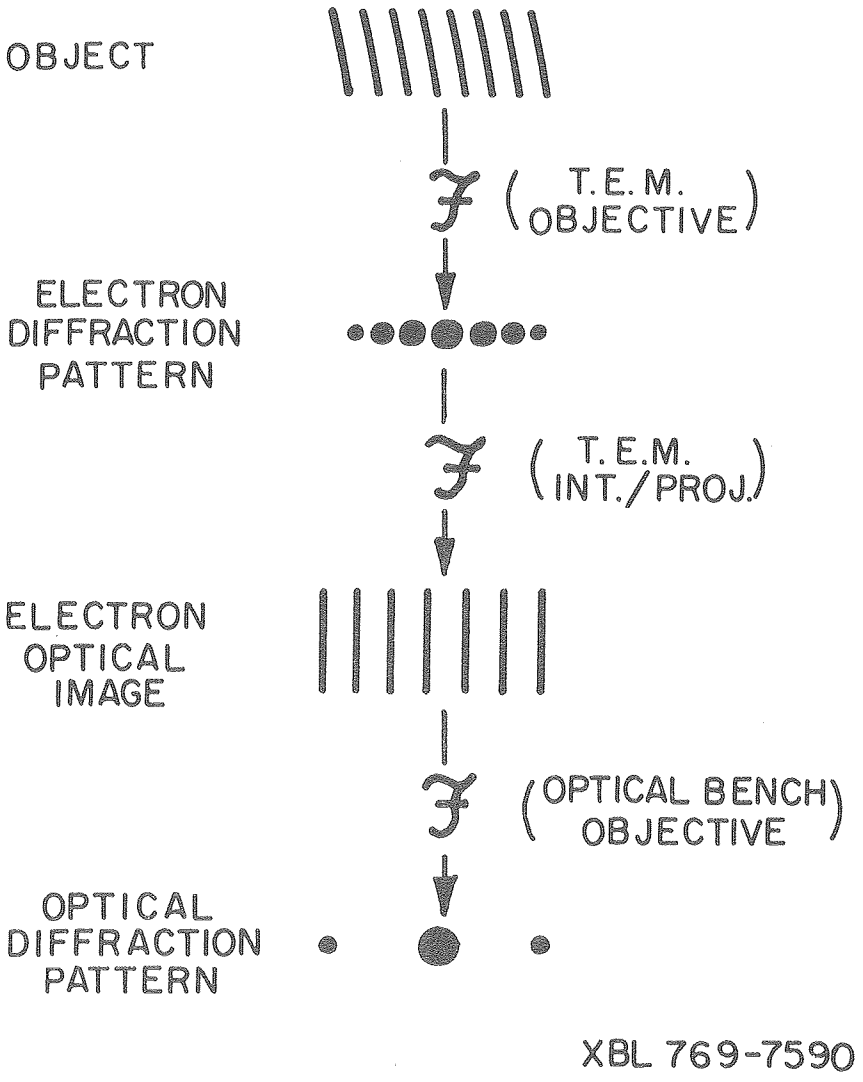
OBJECT
T.E.M. OBJECTIVE
ELECTRON DIFFRACTION PATTERN
T.E.M. INT./PROJ.
ELECTRON OPTICAL IMAGE
OPTICAL BENCH OBJECTIVE
OPTICAL DIFFRACTION PATTERN
XBL 769-7590

Fig. 48

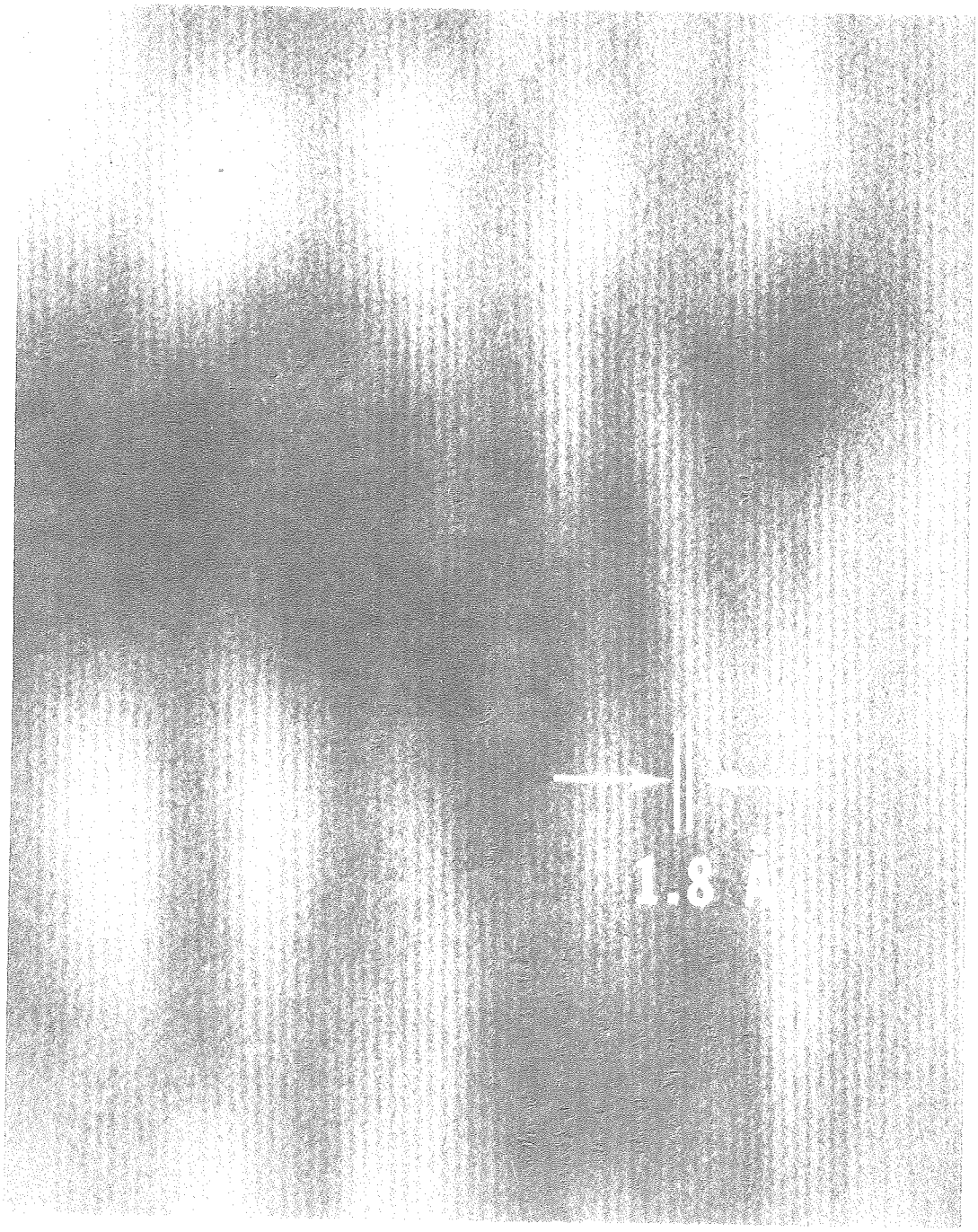

XBB 757-5130

Fig. 49

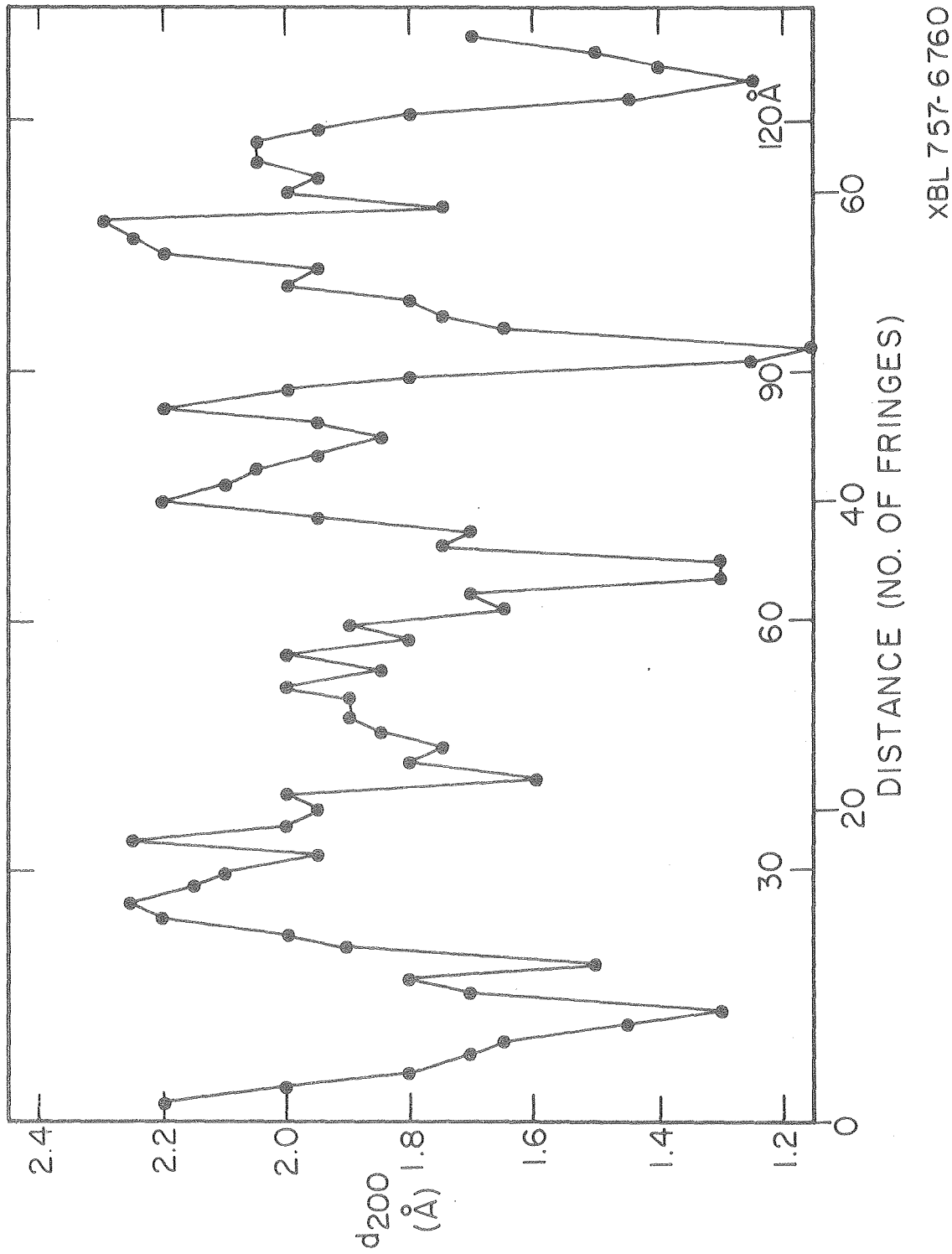

Fig. 50(a)

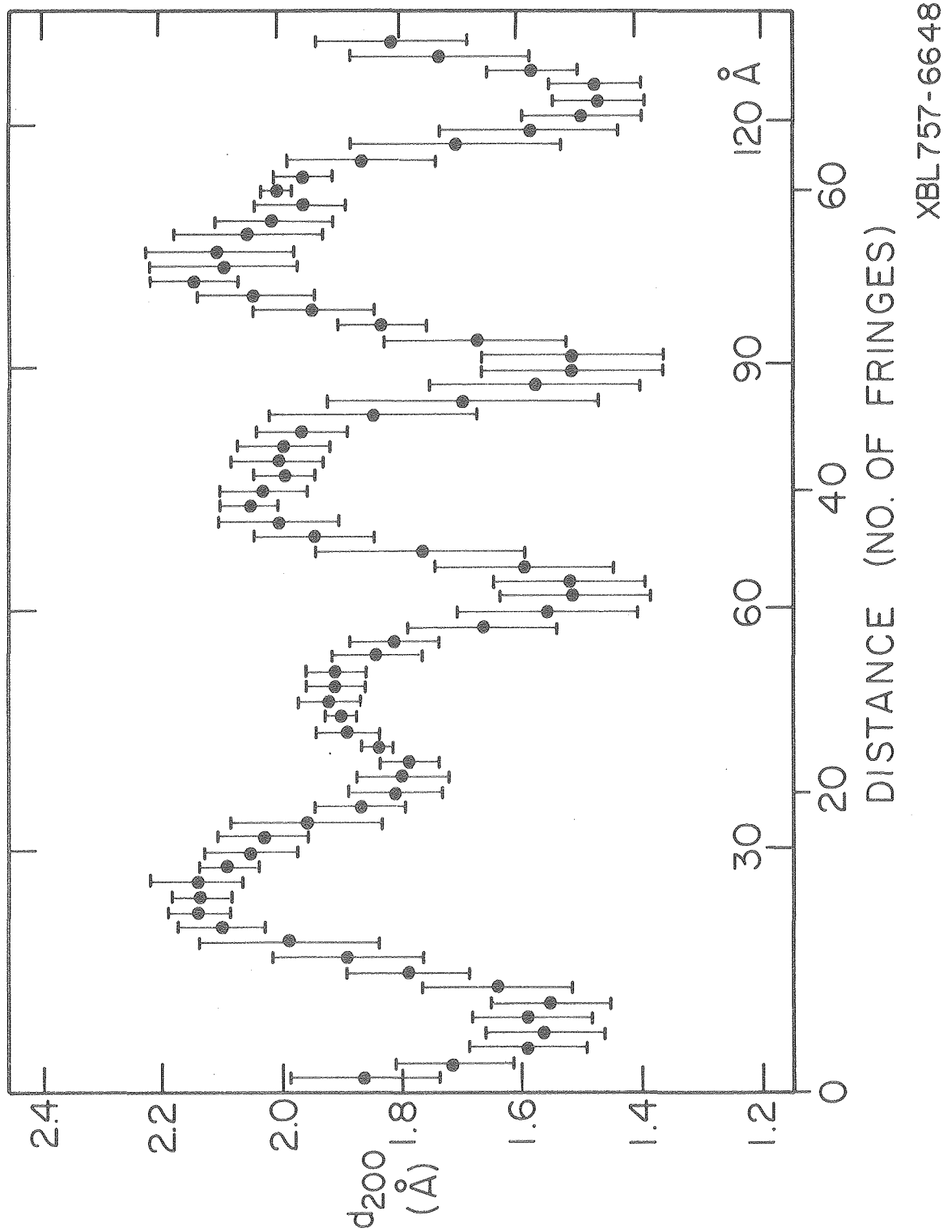
XBL757-6648
DISTANCE (NO. OF FRINGES)
0
20
40
60
90
120 Å
30
60
d200 (Å)
2.4
2.2
2.0
1.8
1.6
1.4
1.2

Fig. 50(b)

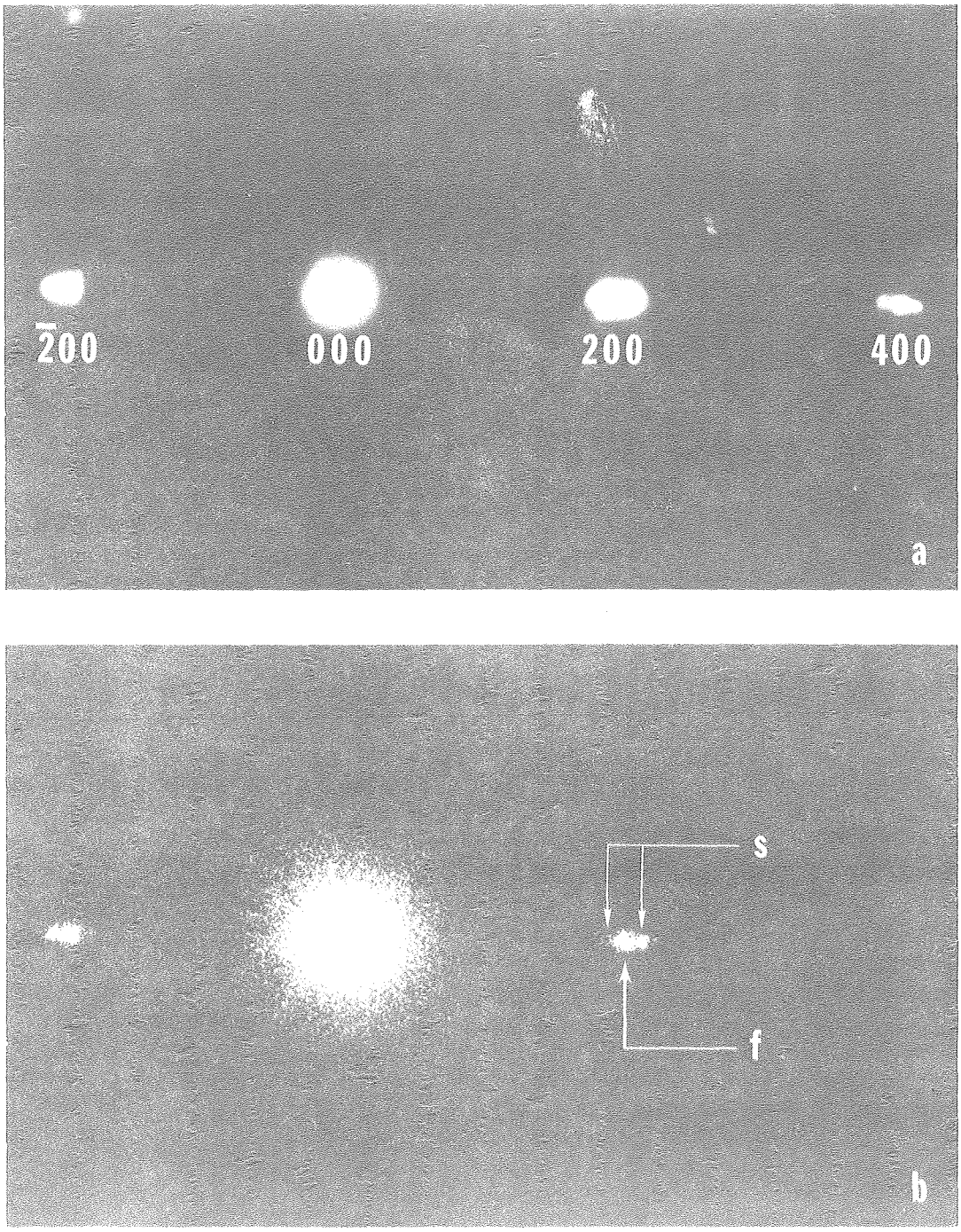

XBB 757-5132A

Fig. 51

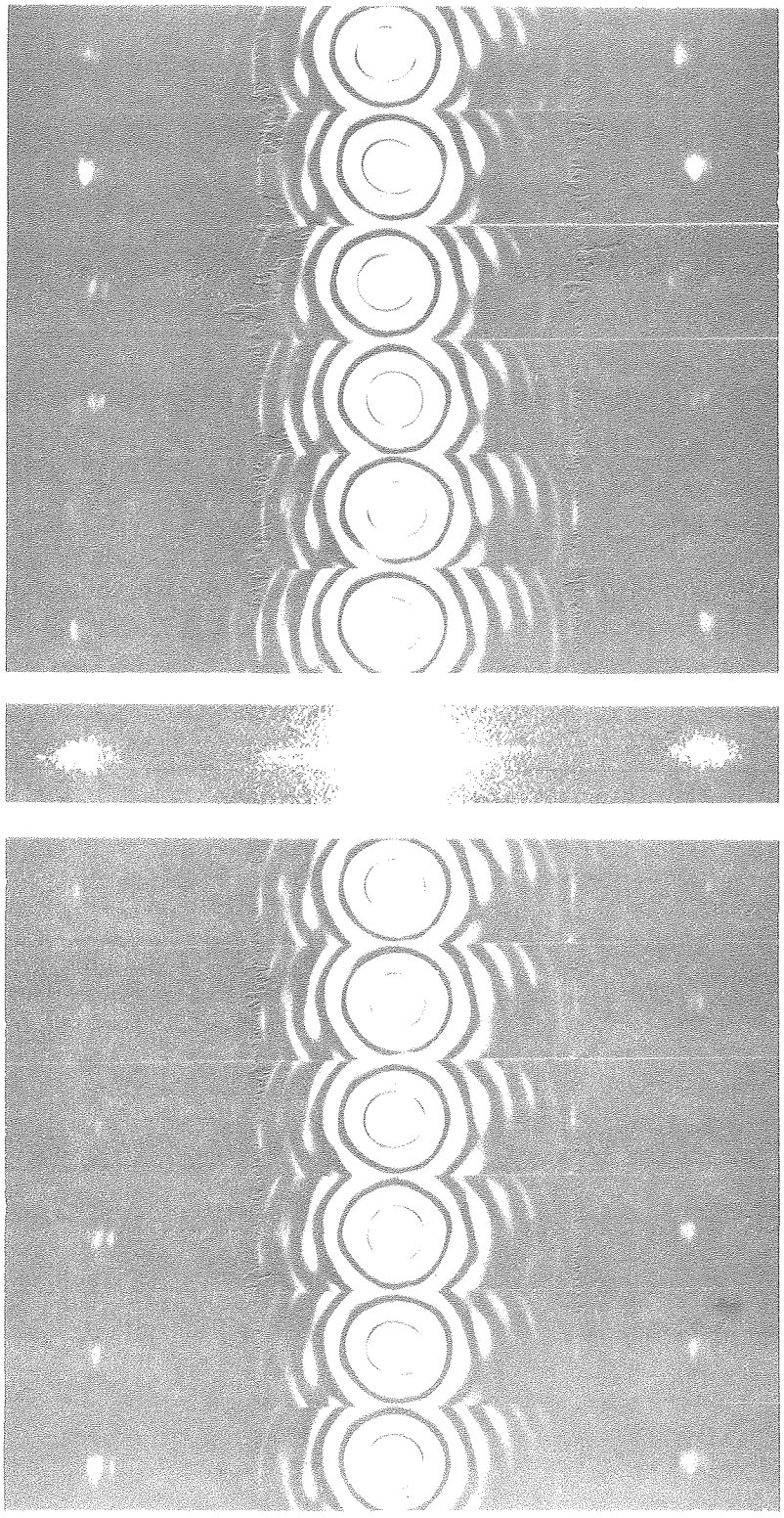

XBB 763-2668

Fig. 52(a)

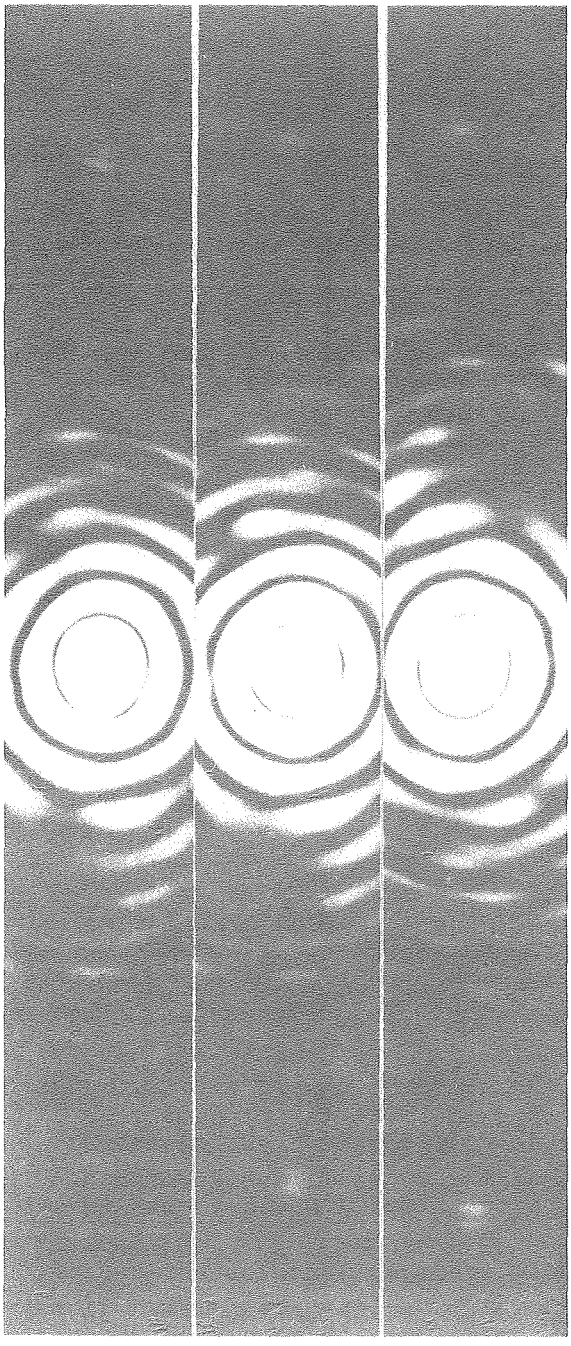

XBB 762-1582

Fig. 52(b)